

A Priori Subgrid Analysis of Temporal Mixing Layers with Evaporating Droplets

Nora Okong'o and Josette Bellan

Jet Propulsion Laboratory

California Institute of Technology

4800 Oak Grove Drive, M/S 125-109,

Pasadena CA 91109-8099

Submitted to Physics of Fluids

*subgrid scale models
drop-laden mixing layers
a priori subgrid scaling
turbulent flows*

Abstract

Subgrid analysis of a transitional temporal **mixing layer** with **evaporating droplets** has been performed using three sets of results from a Direct Numerical Simulation (DNS) database, with Reynolds numbers (based on initial vorticity thickness) as large as 600 and with droplet mass loadings as large as 0.5. In the DNS, the gas phase is computed using a Eulerian formulation, with Lagrangian droplet tracking. The **Large Eddy Simulation (LES)** equations corresponding to the DNS are first derived, and key assumptions in deriving them are first confirmed by computing the terms using the DNS database. Since LES of this flow requires the computation of unfiltered gas-phase variables at droplet locations from filtered gas-phase variables at the grid points, it is proposed to model these by assuming the gas-phase variables to be the sum of the filtered variables and a correction based on the filtered standard deviation; this correction is then computed from the Subgrid Scale (SGS) standard deviation. This model predicts the unfiltered variables at droplet locations considerably better than simply interpolating the filtered variables. Three methods are investigated for modeling the SGS standard deviation:

the Smagorinsky approach, the Gradient model and the Scale-Similarity formulation. When the proportionality constant inherent in the SGS models is properly calculated, the Gradient and Scale-Similarity methods give results in excellent agreement with the DNS.

I. INTRODUCTION

Droplet-laden turbulent flows are an inherent part of atmospheric flows such as rain and superficial oceanographic shear layers, and of industrial processes such as spray painting, ink jet printing, household and medical spray dispensing, and spray atomization and combustion in engines and furnaces. The interaction of particles and turbulence gives these flows their particular characteristics which are different from single phase flows. For example, it is well known that addition of particles to a mixing layer increases or decreases its stability depending upon the ratio of the particle diameter divided by the turbulence length scale (see [5]). Moreover, when gas evolves from the particles (e.g. phase change for drops, chemical reactions for solid particles) there is an additional thermodynamic coupling related to the dynamic one (because of the added mass to the gas phase) which might change this stability boundary.

Because the particles-turbulence interaction is an integral feature of such flows, it has been the topic of much research [3,5,7,21]. Large Eddy Simulation (LES), in which the flow field is spatially filtered, is emerging as a powerful tool in modeling unsteady turbulent flows. It is expected to be more generally applicable than Reynolds-Averaged Navier Stokes (RANS), since the large scale structures are computed, and the more universal small scale structures are modeled. LES is also less computationally intensive than Direct Numerical Simulation (DNS) in which all length scales are resolved, and has the additional advantage of being able to accommodate considerably larger Reynolds numbers. Whereas much research has been devoted to LES modeling for single phase incompressible flows, only moderate attention has been given to compressible shear flows [1,25], with focus now turning two-phase flows [6,19,29]. In addition to modeling subgrid scale (SGS) terms for the gas phase, a LES of a droplet-laden flow would require modeling the unfiltered gas phase variables at the droplet locations. Several LES studies exist of particle laden homogeneous shear flows [30], of mixing layers [19], [28], of particle laden channel flows [23], [26], [27], of sprays [17], and of general particle laden flows [6]. However, none of those studies benefitted from an

a priori SGS model; instead, the SGS model was assumed and sometimes further validated with data. In the present study, we develop an *a priori* SGS model for drop laden mixing layers with phase change.

The success of the LES approach crucially depends upon the fidelity of the SGS in modeling the small scales by using only the values of the variables at the larger scale, which are the only quantities available in the LES context. In simplistic models, the filtered variables are substituted for the unfiltered variables, but this expeditious choice is made only when DNS databases or empirical data are not available to guide SGS modeling; this assumption may be substantially inaccurate for droplets. With an increasing body of DNS computations, [3], [7], [10], [11], [13], [14], [15], [22], and [24], it is now possible to assess SGS quantities at moderate Reynolds numbers, with good prospects for devising SGS models.

In a recent DNS, Miller and Bellan [14,15] generated a database for droplet laden three-dimensional mixing layers with phase change. The authors used the terminology ‘DNS’ to refer to computations in which all length scales of the gas-phase are resolved but the effect of the gas on each droplet (drop sizes are smaller than the Kolmogorov scale) is modeled using a validated drop model based on non-equilibrium evaporation and Stokes drag with a drag coefficient accounting for blowing from the drops. Drops and gas are entirely coupled, both dynamically and thermodynamically, and the effect of the droplets on the gas is modeled through source terms in the gas-phase equations. The present paper addresses the use of the DNS database of Miller and Bellan [14] to evaluate SGS closures. Specifically, we examine three Reynolds number (Re , based on initial vorticity thickness, $\delta_{\omega,0}$, and initial velocity difference, ΔU_0) and mass loading (ML) combinations: $Re = 500, ML = 0.2$; $Re = 500, ML = 0.5$; $Re = 600, ML = 0.2$. We consider the fully developed flow situation for all cases, corresponding to a dimensionless time $t\Delta U_0/\delta_{\omega,0}$ of about 85.

II. GOVERNING EQUATIONS

The governing equations are formulated in an Eulerian - Lagrangian manner whereby the carrier gas is modeled in an Eulerian frame whereas the drops are followed on their trajectory in a Lagrangian frame. These equations for the gas phase are recalled from Miller and Bellan [15] to be:

$$\frac{\partial \rho}{\partial t} + \frac{\partial}{\partial x_j} [\rho u_j] = S_I \quad (1)$$

$$\frac{\partial \rho u_i}{\partial t} + \frac{\partial}{\partial x_j} [\rho u_i u_j + P \delta_{ij} - \sigma_{ij}] = S_{II,i} \quad (2)$$

$$\frac{\partial \rho E}{\partial t} + \frac{\partial}{\partial x_j} \left[(\rho E + P) u_j - \lambda \frac{\partial T}{\partial x_j} - u_i \sigma_{ij} \right] = S_{III} \quad (3)$$

$$\frac{\partial \rho Y_V}{\partial t} + \frac{\partial}{\partial x_j} \left[\rho Y_V u_j - \rho \Gamma \frac{\partial Y_V}{\partial x_j} \right] = S_I \quad (4)$$

$$\sigma_{ij} = \mu \left(\frac{\partial u_i}{\partial x_j} + \frac{\partial u_j}{\partial x_i} - \frac{2}{3} \frac{\partial u_k}{\partial x_k} \delta_{ij} \right) \quad (5)$$

$$P = \rho R T \quad (6)$$

$$E = \frac{1}{2} u_i u_i + C_v T + h_V^0 Y_V \quad (7)$$

$$R = Y_V R_V + (1 - Y_V) R_C \quad (8)$$

$$C_v = Y_V C_{v,V} + (1 - Y_V) C_{v,C} \quad (9)$$

$$C_p = Y_V C_{p,V} + (1 - Y_V) C_{p,C} = R + C_v \quad (10)$$

where ρ is the gas phase density, u_i is the gas phase velocity, $E = e + u_i u_i / 2$ is the total gas energy (internal e , plus kinetic), P is the thermodynamic pressure, σ_{ij} is the viscous stress

tensor, Y_V is the mass fraction of the evaporated species, subscript V denotes the vapor, subscript C denotes the carrier gas, the mass fraction of the carrier gas is $Y_C = 1 - Y_V$, δ_{ij} is the Kronecker delta function, $R_V = R_u/W_V$ with W denoting the molecular weight and R_u being the universal gas constant, and μ , λ and Γ are the constant gas phase viscosity, thermal conductivity and Fickian diffusion coefficient, respectively. The right hand side terms S_I , $S_{II,i}$ and S_{III} describe the phase couplings of mass, momentum and energy, respectively (discussed below). Note that a variable density (compressible) formulation is necessary even for low velocity flows due to the presence of both the mass source term and to non-equal molecular weight effects.

Coupled to the gas conservation equations, the Lagrangian particle equations for the position (X_i), velocity (v_i) temperature (T_d) and mass (m_d) are:

$$\frac{dX_i}{dt} = v_i, \quad (11)$$

$$\frac{dv_i}{dt} = \frac{F_i}{m_d}, \quad (12)$$

$$\frac{dT_d}{dt} = \frac{Q + \frac{dm_d}{dt} L_v}{m_d C_L}, \quad (13)$$

where the coupling between flow and drops is contained in the force term, F_i , the heat transfer term, Q , and the mass evolution from the drop term, dm_d/dt . Computation of the drag force F_i , the heat flux Q and the evaporation rate dm_d/dt requires knowledge of the gas phase variables (u_i, T, Y_V, P) at the droplet locations, and involves in particular the use of validated models for the description of a single drop behavior [15]. Employing these validated relationships, yields:

$$F_i = m_d \left(\frac{f_1}{\tau_d} \right) (u_i - v_i), \quad (14)$$

$$Q = m_d \left(\frac{f_2}{\tau_d} \right) \left(\frac{Nu C_{p,G}}{3 Pr} \right) (T - T_d), \quad (15)$$

$$\frac{dm_d}{dt} = \dot{m}_d = -m_d \left(\frac{1}{\tau_d} \right) \left(\frac{Sh}{3Sc} \right) \ln [1 + B_M], \quad (16)$$

where the subscript d denotes individual droplet conditions, the particle time constant for Stokes flow is $\tau_d = \rho_L D^2 / (18\mu)$, D is the droplet diameter, C_L is the heat capacity of the liquid and the latent heat of evaporation is L_V . The gas mixture heat capacity is calculated using a mass averaging, $C_{p,G} = (1 - Y_V)C_{p,C} + Y_VC_{p,V}$ (evaluated at the droplet location) where $C_{p,C}$ and $C_{p,V}$ are the constant pressure heat capacities of the carrier gas and vapor, respectively ($C_{v,C}$ and $C_{v,V}$ are the corresponding constant volume heat capacities). The gas phase Prandtl and Schmidt numbers are $Pr = \mu C_{p,G} / \lambda$ and $Sc = \mu / (\rho \Gamma)$, respectively. The evaporation rate is determined by the mass transfer number; $B_M = (Y_S - Y_V) / (1 - Y_S)$ (subscript S denotes droplet surface conditions). To account for the effects of finite droplet slip Reynolds numbers, the semi-empirical Ranz-Marshall correlations are utilized for the Nusselt (Nu) and Sherwood (Sh) numbers, whereas f_1 is an empirical correlation accounting for the effects of both finite slip and evaporation to Stokes drag. The function $f_2 = \beta / (e^\beta - 1)$ is an analytical evaporative heat transfer correction, where the non-dimensional evaporation parameter $\beta = -1.5 Pr \tau_d \dot{m}_d / m_d$ is constant for droplets obeying the ' D^2 law'. The vapor surface mass fraction is calculated directly from the surface molar fraction (χ_s) which is obtained by equating the vapor and liquid fugacities at the surface (i.e. $\chi_s P = P_{sat}$) with the saturation pressure (P_{sat}) provided by the Clausius-Clapeyron relation yielding:

$$Y_S = \frac{\chi_s}{\chi_s + (1 - \chi_s)W_C/W_V}, \quad \chi_s = \frac{P_{atm}}{P} \exp \left\{ \frac{L_V}{R_V} \left(\frac{1}{T_{B,L}} - \frac{1}{T_d} \right) \right\}, \quad (17)$$

where P_{atm} is atmospheric pressure, $T_{B,L}$ is the liquid saturation temperature at P_{atm} (i.e. the normal boiling temperature). As shown by Miller and Bellan [15], the latent heat must be a linear function of temperature for calorically perfect species: $L_V = h_V^0 - (C_L - C_{p,V})T_d$.

Equations 11 - 17 allow the computation of the eqs. 1 - 4 source terms which are (see Miller and Bellan [15])

$$S_I = - \sum_{\alpha} \frac{w_{\alpha}}{V} \left[\frac{dm_d}{dt} \right]_{\alpha} \quad (18)$$

$$S_{II,i} = - \sum_{\alpha} \frac{w_{\alpha}}{V} \left[F_i + \frac{dm_d}{dt} v_i \right]_{\alpha} \quad (19)$$

$$S_{III} = - \sum_{\alpha} \frac{w_{\alpha}}{V} \left[F_i v_i + Q + \frac{dm_d}{dt} \left(\frac{1}{2} v_i v_i + C_{p,V} T_d + h_V^0 \right) \right]_{\alpha} \quad (20)$$

where the summation is over the α droplets within a discretization volume V associated with each grid point, and the weights w_{α} distribute the droplet contribution among the nearest eight grid points; this weighting is necessary because the drop locations do not coincide in general to Eulerian grid points. On the other hand, eqs. 11 - 16 require the knowledge of the gas flow variables at the drop locations; this is accomplished by using a fourth order Lagrange interpolation procedure [15].

As explained by Miller and Bellan [15], even for the smaller mass loadings used in the calculations, the source terms exhibit spatial ‘spottiness’ resulting in artificial oscillations. To mitigate this situation, the source terms are minimally smoothed with a conservative operator. This operation is not a filtering, as one of the filter’s characteristics is to truncate the high wave number terms, resulting in a nonconservative procedure.

The governing equations are integrated in time using a fourth-order Runge-Kutta explicit scheme, with eighth-order finite-differences for all derivatives and fourth-order Lagrangian interpolation of gas-phase variables to droplet locations, as explained in detail in Miller and Bellan [15]). The numerical mesh is uniform in all directions with $\Delta x_1 \simeq \Delta x_2 \simeq \Delta x_3$.

The initial conditions are similar to those of Moser and Rogers [16] and we refer the reader to Miller and Bellan [15] for details. Basically, the configuration chosen is that of the temporally developing mixing layer where the streamwise (x_1), cross stream (x_2) and spanwise (x_3) coordinates are defined, and the respective lengths are $L_1 = 4\lambda_1$, $L_2 = 1.1L_1$ and $L_3 = 4\lambda_3$, where λ_1 and λ_3 are the forcing wavelengths in the x_1 and x_3 directions, $\lambda_1 = 7.29\delta_{\omega,0}$ is an empirically found (see Moser and Rogers [16]) most unstable wavelength for the initial profile, and $\lambda_3 = 0.6\lambda_1$ following the suggestion of [16]; for all the simulations performed by Miller and Bellan [15] $L_1 = 0.2$ m. The relative amplitudes of the forcing perturbations with respect to the circulations are 10% and 2.25% in the spanwise and streamwise

directions, respectively. The boundary conditions used in conjunction with the conservation equations were periodic in the x_1 and x_3 directions, and adiabatic slip-wall conditions in the x_2 direction were employed. To insure physical consistency and avoid numerical instabilities, the wave decomposition method of Poinso and Lele [18] was used at the slip-wall boundaries. The initial vorticity thickness was $\delta_{\omega,0}$ and $\delta_{\omega}(t) = \Delta U_0 / \langle \partial u_1 / \partial x_2 \rangle_{\max}$ where the brackets $\langle \rangle$ indicate averaging over homogeneous $x_1 - x_3$ planes. The freestream velocity difference across the layer, ΔU_0 was calculated from a specified value of the convective Mach number, M_c .

The purpose of this investigation is to develop a SGS model to be utilized in a LES for a drop laden shear layer. Just as in the DNS, in the LES, the gas phase equations will be solved in an Eulerian frame, but at the LES, larger scale rather than the DNS scale, whereas the drops will be followed in a Lagrangian frame. Therefore we can immediately identify two additional issues to that of the expected modeling of the SGS terms in the filtered gas phase equations. First, gas phase variables being calculated on the larger grid may no longer be a good representation of the equivalent DNS values, and the question arises on how to accurately calculate these unfiltered values at the drop locations. On the other hand, the drop dependent variables are accurately calculated at each drop location if every single drop is followed on its trajectory. However, since the gas phase source terms in the filtered equations represent averages over the drops in the filtered volume, there is an inherent degree of uncertainty on how to model these source terms, i.e. how to accurately represent them using only information at the LES scale. This uncertainty represents the second additional issue to be addressed in a two phase flow LES formulated in the Eulerian/Lagrangian context. We address in this paper the first issue identified above and defer the discussion of the second issue to a future publication.

III. FILTERED GOVERNING EQUATIONS

A. General equations

The general definition of a filter operation is:

$$\bar{\phi}(\vec{x}) = \int_V \phi(\vec{y}) G_\Delta(\vec{x} - \vec{y}) d\vec{y} \quad (21)$$

where G_Δ is the filter function, and V is the filtering volume. In this study, we use a cubic top-hat filter, in which V is a cube of sides Δ , and G_Δ is simply a volume-average:

$$G_\Delta(\vec{x} - \vec{y}) = \frac{1}{\Delta^3} \prod_{i=1}^3 \{H(\Delta/2 - |x_i - y_i|)\} \quad (22)$$

where $H(x)$ is the Heaviside function and Δ is the filter width. Our choice is guided by the simplicity of the associated integrations according to eq. 21, and we disregard at this point the fact that the filtered equations are no longer invariant to coordinate rotations other than orthogonal. Since the goal of this investigation is to perform a LES of the shear layer using the SGS derived herein (and compare it with the filtered DNS), this lack of invariance can be tolerated. One of the properties of eq. 21 is that for $\phi = 1$, $\bar{\phi} = 1$ as well. For compressible flow, we define the traditional Favre filtered variables as $\tilde{\phi} = \bar{\rho\phi}/\bar{\rho}$, thereby removing the density fluctuations from the averaged equations. Applying the filtering, and assuming that differentiation and filtering commute, the gas phase equations become:

$$\frac{\partial \bar{\rho}}{\partial t} + \frac{\partial}{\partial x_j} [\bar{\rho} \tilde{u}_j] = \bar{S}_I \quad (23)$$

$$\frac{\partial \bar{\rho} \tilde{u}_i}{\partial t} + \frac{\partial}{\partial x_j} [\bar{\rho} \tilde{u}_i \tilde{u}_j + \bar{P} \delta_{ij} - \tilde{\sigma}_{ij} + \bar{\rho} \tau_{ij}] = \bar{S}_{II,i} \quad (24)$$

$$\begin{aligned} \frac{\partial \bar{\rho} \tilde{E}}{\partial t} + \frac{\partial}{\partial x_j} \left[(\bar{\rho} \tilde{E} + \bar{P}) \tilde{u}_j - \lambda \frac{\partial \bar{T}}{\partial x_j} - \tilde{u}_i \tilde{\sigma}_{ij} \right] \\ + \frac{\partial}{\partial x_j} \left[\tilde{u}_i \bar{\rho} \tau_{ij} + C_{p,C} \bar{\rho} \theta_j + \left\{ (C_{p,V} - C_{p,C}) \bar{T} + h_V^0 \right\} \bar{\rho} \eta_j \right] \\ = \bar{S}_{III} \end{aligned} \quad (25)$$

$$\frac{\partial \bar{\rho} \tilde{Y}_V}{\partial t} + \frac{\partial}{\partial x_j} \left[\bar{\rho} \tilde{Y}_V \tilde{u}_j - \bar{\rho} \Gamma \frac{\partial \tilde{Y}_V}{\partial x_j} + \bar{\rho} \eta_j \right] = \bar{S}_I \quad (26)$$

where we have defined

$$\tau_{ij} = \widetilde{u_i u_j} - \tilde{u}_i \tilde{u}_j \quad (27)$$

$$\theta_j = \widetilde{T u_j} - \bar{T} \tilde{u}_j \quad (28)$$

$$\eta_j = \widetilde{Y_V u_j} - \tilde{Y}_V \tilde{u}_j \quad (29)$$

$$\tilde{\sigma}_{ij} = \mu \left(\frac{\partial \tilde{u}_i}{\partial x_j} + \frac{\partial \tilde{u}_j}{\partial x_i} - \frac{2}{3} \frac{\partial \tilde{u}_k}{\partial x_k} \delta_{ij} \right) \quad (30)$$

$$\tilde{C}_p = \tilde{Y}_V C_{p,V} + (1 - \tilde{Y}_V) C_{p,C} \quad (31)$$

$$\tilde{C}_v = \tilde{Y}_V C_{v,V} + (1 - \tilde{Y}_V) C_{v,C} \quad (32)$$

$$\tilde{R} = \tilde{Y}_V R_V + (1 - \tilde{Y}_V) R_C = \tilde{C}_p - \tilde{C}_v \quad (33)$$

and it has been assumed that

$$\bar{\sigma}_{ij} = \tilde{\sigma}_{ij} \quad (34)$$

$$\overline{u_i \sigma_{ij}} = \tilde{u}_i \tilde{\sigma}_{ij} \quad (35)$$

$$\frac{1}{2} (\overline{\rho u_i u_i u_j} - \overline{\rho u_i u_i} \tilde{u}_j) = \bar{\rho} \tau_{ij} \tilde{u}_i \quad (36)$$

$$\overline{\rho Y_V T} = \overline{\rho Y_V} \bar{T} \quad (37)$$

$$\overline{\rho Y_V T u_j} - \overline{\rho Y_V T} \tilde{u}_j = \bar{\rho} \bar{T} (\widetilde{Y_V u_j} - \tilde{Y}_V \tilde{u}_j) \quad (38)$$

$$\bar{T} = \tilde{T} \quad (39)$$

$$\bar{P} = \bar{\rho} \tilde{R} \bar{T} \quad (40)$$

$$\tilde{E} = \frac{1}{2} \tilde{u}_i \tilde{u}_i + \tilde{C}_v \bar{T} + h_V^0 \tilde{Y}_V + \frac{1}{2} \tau_{ii} \quad (41)$$

$$\overline{\rho \Gamma \frac{\partial Y_V}{\partial x_j}} = \bar{\rho} \Gamma \frac{\partial \tilde{Y}_V}{\partial x_j} \quad (42)$$

Equation 36 is inspired by the RANS equations and the term $(C_{p,V} - C_{p,C}) \bar{\rho} \eta_j \bar{T} + C_{p,C} \bar{\rho} \theta_j$ is a direct result of the assumption of eq. 38. For example, if we assume instead that

$$\overline{\rho Y_V T u_j} - \overline{\rho Y_V T} \tilde{u}_j = \bar{\rho} \tilde{Y}_V (\tilde{T} \tilde{u}_j - \bar{T} \tilde{u}_j), \quad (43)$$

this term would be replaced by $\tilde{C}_p \bar{\rho} \theta_j$. Moreover, eq. 42 is derived (for constant Γ) from

$$\overline{\rho \frac{\partial Y_V}{\partial x_j}} = \overline{\frac{\partial \rho Y_V}{\partial x_j}} - \overline{Y_V \frac{\partial \rho}{\partial x_j}} = \frac{\partial \bar{\rho} \tilde{Y}_V}{\partial x_j} - \overline{Y_V \frac{\partial \rho}{\partial x_j}} = \bar{\rho} \frac{\partial \tilde{Y}_V}{\partial x_j} + \left(\tilde{Y}_V \frac{\partial \bar{\rho}}{\partial x_j} - \overline{Y_V \frac{\partial \rho}{\partial x_j}} \right) \quad (44)$$

by assuming the last term to be negligible. Also, in contrast to the single phase situation where the filtered equation of state contains \tilde{T} only, in the two phase case $\tilde{Y}_V \tilde{T}$ appears as well. In the next subsection we will assess the validity of all assumptions introduced by eqs. 34 - 39 and 42 and show that they are justified for the three sets of results analyzed.

In the present two phase flow formulation a SGS model must contain not only models for the subgrid stresses, τ_{ij} , but also models for the subgrid heat flux θ_j and the subgrid species flux η_j . Furthermore, since it is \bar{T} rather than \tilde{T} that appears in the heat flux in the energy equation, this introduces the quandary as to which is the appropriate averaging of the temperature. In the SGS model presented below we opt to use \bar{T} , making therefore the assumption that $\bar{T} = \tilde{T}$, and note that using \tilde{T} requires the assumption [8] that $\partial \tilde{T} / \partial x_j = \partial \bar{T} / \partial x_j$; an assessment of the former assumption is presented below.

The SGS modeling is performed with the understanding that the droplet equations will still be solved in the LES, except that in LES the gas-phase variables (u_i, T, Y_V, P) at the droplet locations are no longer immediately available and need to be derived from the filtered variables $(\tilde{u}_i, \bar{T}, \tilde{Y}_V, \bar{P})$. Therefore, in order to be able to utilize a SGS model, one must also construct a model of each of the unfiltered gas-phase variables as functions of the filtered values of the same variable. These models will be derived in the next section.

B. Magnitude of terms and evaluation of underlying assumptions in the LES equations

1. Magnitude of terms in LES equations

An evaluation of the magnitude of various terms in the LES equations is prerequisite not only to assessing the assumptions of eqs. 34 - 39 and 42, but it is also crucial in providing both an understanding of the balance among terms, and an intuition on the models that may be used for SGS modeling. This evaluation is performed using the three sets of results from the database generated by Miller and Bellan [14], TP500a, TP500b and TP600 of a transitional, temporal drop laden mixing layer whose characteristics are summarized in Table I. As stated above, the Reynolds number, Re , is based on initial vorticity thickness, $\delta_{\omega,0}$, and initial velocity difference, ΔU_0 . The mass loading, ML , is the initial loading in the droplet-laden stream and the database contains the results at the dimensionless time of $t\Delta U_0/\delta_{\omega,0} = 85$. All three simulations were performed in a domain with grid size $0.2m \times 0.22m \times 0.12m$. Our analysis is performed on the same grid as the DNS, with the resolutions listed in Table I, and all derivatives are calculated employing the same eighth-order finite-difference operator as in the DNS. In all cases, we use a cubic top-hat (box) filter, with filter width $\Delta = 4 \max(\Delta x_1, \Delta x_2, \Delta x_3)$ where $\Delta x_1 \simeq \Delta x_2 \simeq \Delta x_3$.

Presented in Tables II - VI is such an evaluation for the momentum eq. 24 (Tables II - IV), the energy eq. 25 (Table V), and the species eq. 26 (Table VI). Listed in the tables are the global root-mean-squares ($RMS(\phi) = \sqrt{\langle\langle\langle \phi^2 \rangle\rangle\rangle}$, where $\langle\langle\langle \rangle\rangle\rangle$ denotes averaging over the whole domain) for cases TP500a, TP500b and TP600. From Tables II - IV it is immediately apparent that in the three momentum equations $\partial \bar{\rho} \tilde{u}_i \tilde{u}_j / \partial x_j$ and $\partial \bar{P} / \partial x_j$ are the largest terms, and that they are of about the same order of magnitude. The smallest term, which is two orders of magnitude smaller than the largest, is $\partial(\bar{\sigma}_{ij} - \tilde{\sigma}_{ij}) / \partial x_j$, justifying the assumption $\bar{\sigma}_{ij} = \tilde{\sigma}_{ij}$. In the middle range are $\partial \bar{\rho} \tau_{ij} / \partial x_j$ and $\partial \tilde{\sigma}_{ij} / \partial x_j$, with the former term being about three times as large as the latter, whereas the source term $\tilde{S}_{II,i}$

is slightly smaller than the middle range terms. Note that the source terms which are listed in Tables II - VI are averaged over the whole grid, but are zero over about 20% of the grid where there are no droplets. However, planar RMS evaluations of the relative magnitude of the same terms in the center of the mixing layer (see Fig. 1 for case TP600) gives the same magnitude as that over the entire domain, thereby reinforcing our magnitude ranking above.

A similar evaluation of the energy equation terms displayed in Table V reveals that the inviscid subgrid term is of the same order of magnitude as the resolved inviscid term $\partial(\bar{\rho}\tilde{E} + \bar{P})\tilde{u}_j/\partial x_j$, followed by the heat flux and the resolved viscous term. The viscous subgrid term $\partial(\overline{u_i\sigma_{ij}} - \tilde{u}_i\tilde{\sigma}_{ij})/\partial x_j$ is about one-third of the viscous resolved term $\partial\tilde{u}_i\tilde{\sigma}_{ij}/\partial x_j$, suggesting that although $\partial\overline{u_i\sigma_{ij}}/\partial x_j$ and $\partial\tilde{u}_i\tilde{\sigma}_{ij}/\partial x_j$ are of the same magnitude, they are not perfectly correlated. The correlation between two terms is defined either by averaging over homogeneous $(x_1 - x_3)$ planes

$$\mathcal{R}(X, Y; x_2) = \frac{\langle XY \rangle}{\sqrt{\langle X^2 \rangle} \sqrt{\langle Y^2 \rangle}} \quad (45)$$

or over the whole domain

$$\mathcal{R}(X, Y) = \frac{\langle\langle\langle XY \rangle\rangle\rangle}{\sqrt{\langle\langle\langle X^2 \rangle\rangle\rangle} \sqrt{\langle\langle\langle Y^2 \rangle\rangle\rangle}} \quad (46)$$

where by definition \mathcal{R} is between -1 and 1. As usual, values near 1 indicate strong positive correlation, values near -1 indicate strong negative correlation, whereas values near 0 indicate poor correlation. More precisely, we find that the correlation of $\partial\overline{u_i\sigma_{ij}}/\partial x_j$ and $\partial\tilde{u}_i\tilde{\sigma}_{ij}/\partial x_j$ over the entire grid is 0.92, and a corresponding linear fit is $\partial\overline{u_i\sigma_{ij}}/\partial x_j = 0.95\partial\tilde{u}_i\tilde{\sigma}_{ij}/\partial x_j$. As will be seen below, this correlation is only slightly worse than that between $\overline{u_i\sigma_{ij}}$ and $\tilde{u}_i\tilde{\sigma}_{ij}$. Moreover, since $\partial(\overline{u_i\sigma_{ij}} - \tilde{u}_i\tilde{\sigma}_{ij})/\partial x_j$ is the smallest term in the energy equation, it is not unreasonable to neglect it. The source term \bar{S}_{III} is about the same size as the heat flux term justifying our expectation that it is an important term.

In Table VI we finally display a comparison of the magnitude of the species equation terms. Clearly, the subgrid term, the source term and the diffusion term are all of the same

order, being an order of magnitude smaller than the resolved convective term. The smallest term $\partial \left(\overline{\rho \Gamma \partial Y_V / \partial x_j} \right) \partial x_j - \partial \left(\bar{\rho} \Gamma \partial \tilde{Y}_V / \partial x_j \right) / \partial x_j$ is about half of $\partial \left(\bar{\rho} \Gamma \partial \tilde{Y}_V / \partial x_j \right) / \partial x_j$, but could possibly be neglected if the correlation between $\overline{\rho \partial Y_V / \partial x_j}$ and $\bar{\rho} \partial \tilde{Y}_V / \partial x_j$ is high; this is indeed the case, as discussed below.

Additional to the global RMS values shown in the tables, the planar RMS values of the various terms in each equation are presented for case TP600 in Fig. 1 (in the figures [] and { } are used to denote regular and Favre filtering, respectively), and they confirm the conclusions reached from the global RMS values.

2. Evaluation of LES assumptions

A systematic evaluation of the key assumptions made in deriving the LES equations is presented in Figs. 2 - 6 by showing the $(x_1 - x_3)$ plane averages of the approximated terms. The analysis is carried out for case TP600 with $\Delta = 4 \max(\Delta x_1, \Delta x_2, \Delta x_3)$, as above. Clearly, the assumption of eq. 36 ($\frac{1}{2}(\overline{\rho u_i u_i u_j} - \overline{\rho u_i u_i} \tilde{u}_j) = \bar{\rho} \tau_{ij} \tilde{u}_i$) is quite reasonable, as shown in Fig. 2. The assumptions of eq. 39 ($\bar{T} = \tilde{T}$) and 37 ($\overline{\rho Y_V T} = \bar{\rho} Y_V \bar{T}$) are also justified for this flow, as seen in Fig. 3, although since the turbulent temperature fluctuations in this study appear to be quite small (as will be discussed below), these two assumptions may hold only in the range of parameters covered by this study, and caution is recommended in using them without justification in more general situations.

Figure 4 addresses the modeling of $\overline{\rho Y_V T u_j}$ through either eq. 38 or eq. 43. As depicted in the figure, the right-hand side of eq. 43, $\bar{\rho} \tilde{Y}_V (\tilde{T} \tilde{u}_j - \bar{T} \tilde{u}_j)$ is almost null and additionally, it is much smaller than the left-hand side $\overline{\rho Y_V T u_j} - \bar{\rho} Y_V \bar{T} \tilde{u}_j$. However, Fig. 4 shows that the left hand side of eq. 38, $\overline{\rho Y_V T u_j} - \bar{\rho} Y_V \bar{T} \tilde{u}_j$, matches the right-hand side, $\bar{\rho} \tilde{T} (\tilde{Y}_V \tilde{u}_j - \tilde{Y}_V \tilde{u}_j)$, thereby indicating that this assumption is correct. Moreover, the correlation over the whole grid for the two-sides of eq. 43 is -0.270 , whereas it is 0.999 for eq. 38, thus justifying the latter assumption.

To evaluate the assumption of eq. 35, $\overline{u_i \sigma_{ij}} = \tilde{u}_i \tilde{\sigma}_{ij}$, we display in Fig. 5 the plane

averages, $\overline{u_i \sigma_{ij}} - \tilde{u}_i \tilde{\sigma}_{ij}$ and $\tilde{u}_i \tilde{\sigma}_{ij}$. Clearly, $\overline{u_i \sigma_{ij}} - \tilde{u}_i \tilde{\sigma}_{ij}$ is small compared to $\tilde{u}_i \tilde{\sigma}_{ij}$ and moreover a linear fit shows $\overline{u_i \sigma_{ij}} = 0.94 \tilde{u}_i \tilde{\sigma}_{ij}$, with a correlation of 0.97; thus the assumption $\overline{u_i \sigma_{ij}} = \tilde{u}_i \tilde{\sigma}_{ij}$ is justified.

Finally, to assess the assumption of eq. 42, we display in Fig. 6 both $\overline{\rho \partial Y_V / \partial x_j}$ and $\tilde{\rho} \partial \tilde{Y}_V / \partial x_j$ and show them to be well correlated. Furthermore, a calculated linear fit shows $\overline{\rho \partial Y_V / \partial x_j} = 0.997 \tilde{\rho} \partial \tilde{Y}_V / \partial x_j$ with a correlation of 0.996, thereby confirming the intuitive idea that $\overline{\rho \partial Y_V / \partial x_j}$ and $\tilde{\rho} \partial \tilde{Y}_V / \partial x_j$ may be assumed equal.

IV. MODEL FOR UNFILTERED GAS PHASE VARIABLES

As discussed above, the unfiltered gas phase variables not being available at the droplet locations, they must be evaluated from the filtered gas phase variables through appropriate models. We define by ‘appropriate models’ those relationships that give values of the unfiltered variables as close in magnitude as possible to those of the DNS, and certainly better than one would obtain by simply interpolating the values of the filtered variables at the droplet locations. To guide the modeling, we will first consider the known DNS generic variable ϕ and its filtered form $\bar{\phi}$, where the bar is here a generic averaging denoting Favre filtering for u_i , and Y_V and regular filtering for T and P . By definition, the standard deviation is

$$\sigma = \sqrt{\phi' \phi'} = \sqrt{(\phi - \bar{\phi})^2} \quad (47)$$

where ϕ' is the fluctuating part of ϕ , and thus the relation between ϕ and $\bar{\phi}$ is

$$\phi = \bar{\phi} + f\sigma \quad (48)$$

where from the definition of σ , $f = \pm 1$. Intuitively, in this formulation, $f\sigma$ can be regarded as a correction to $\bar{\phi}$ with sign f and magnitude σ . The goal of the modeling is to compute, from the filtered flow field, a model of $f\sigma$, $f_m \sigma_m$, that provides a better approximation to ϕ than does $f_m \sigma_m = 0$.

Because of the inherent simplicity, it is at first tempting to assume that f randomly takes on values of -1 and 1. However, one can show that this is not necessarily the case. If the filtering operation is viewed as a volume average, a relation between ϕ and $\bar{\phi}$ can be derived by considering the third-order Taylor expansion of ϕ integrated over the filtering volume V of characteristic length Δ with centroid at $x_0 = (x_{10}, x_{20}, x_{30})$:

$$\bar{\phi}(x_0) = \frac{1}{V} \int_V \phi(x) dV \quad (49)$$

$$\phi(x) = \phi(x_0) + \frac{\partial \phi}{\partial x_i}(x_0)(x_i - x_{i0}) + \frac{\partial^2 \phi}{\partial x_i \partial x_j}(x_0) \frac{1}{2}(x_i - x_{i0})(x_j - x_{j0}) + O(\Delta^3) \quad (50)$$

where from the definition of the centroid, $\frac{1}{V} \int_V (x_i - x_{i0}) dV = 0$. If V is symmetric, then

$$\frac{1}{V} \int_V (x_i - x_{i0})(x_j - x_{j0}) dV = 0; \quad i \neq j \quad (51)$$

and

$$I_c \Delta^2 = \frac{1}{V} \int_V (x_i - x_{i0})(x_j - x_{j0}) dV; \quad i = j \quad (52)$$

is the (positive) moment of inertia, so that one may rewrite eq. 49 as

$$\bar{\phi} = \phi + \nabla^2 \phi \frac{I_c \Delta^2}{2} + O(\Delta^4) \quad (53)$$

where terms of $O(\Delta^3)$ vanish due to the symmetry of the filtering volume.

A comparison between eqs. 48 and 53, and the interpretation that f is a sign correction leads to the conclusion that f will generally be $-sign(\nabla^2 \phi)$. However, ϕ is not available in a LES formulation, and from the available filtered quantities we can compute $\nabla^2 \bar{\phi}$ rather than $\nabla^2 \phi$. Therefore, to model f we assume that $\nabla^2 \bar{\phi}$ and $\nabla^2 \phi$ have the same sign and evaluate this assumption for the gas phase variables in the section devoted to finalizing the SGS models.

To model σ , we note that the SGS terms for the gas phase that must be modeled have the generic form $\overline{\phi\phi} - \bar{\phi}\bar{\phi}$. If one defines σ_{SGS} as the SGS standard deviation,

$$\sigma_{SGS} = \sqrt{\overline{\phi\phi} - \bar{\phi}\bar{\phi}} \quad (54)$$

the relationship between σ and σ_{SGS} can be elucidated by considering $\overline{\sigma^2}$

$$\overline{\sigma^2} = \overline{(\phi - \overline{\phi})^2} = \overline{\phi\phi} - 2\overline{\phi\overline{\phi}} + \overline{\overline{\phi}\overline{\phi}} \quad (55)$$

where the second filter is unweighted (e.g. regular rather than Favre) for all variables. To evaluate the terms in eq. 55, we note that $\overline{\phi\phi} = \sigma_{SGS}^2 + \overline{\phi\overline{\phi}}$ and that $\overline{\overline{\phi}\overline{\phi}}$ can be written in terms of the local correlation between ϕ and $\overline{\phi}$

$$\mathcal{R}(\phi, \overline{\phi}) = \frac{\overline{\phi\overline{\phi}}}{\sqrt{\overline{\phi\phi}}\sqrt{\overline{\overline{\phi}\overline{\phi}}}} \quad (56)$$

If we assume that $\mathcal{R}(\phi, \overline{\phi}) \simeq 1$, then

$$\overline{\sigma^2} = \left(\sqrt{\overline{\phi\phi}} - \sqrt{\overline{\phi\overline{\phi}}} \right)^2 = \left(\sqrt{\sigma_{SGS}^2 + \overline{\phi\overline{\phi}}} - \sqrt{\overline{\phi\overline{\phi}}} \right)^2 \quad (57)$$

The assumption that $\mathcal{R}(\phi, \overline{\phi}) \simeq 1$ was checked for all gas phase variables using the TP600 set of results and was found to be justified (see the finalization of the SGS models section). It is noteworthy that when using even small departures from the unity (i.e. 0.99) assumption, one obtains models for the unfiltered variables (in particular Y_V) that are considerably less accurate than those obtained using $\mathcal{R}(\phi, \overline{\phi}) \simeq 1$.

Defining $\overline{\sigma} = \sqrt{\overline{\sigma^2}}$, and using $\overline{\sigma}$ as a model for σ , we arrive at a model for ϕ of the form

$$\phi = \overline{\phi} - \text{sign}(\nabla^2 \overline{\phi}) \overline{\sigma} \quad (58)$$

i.e. $f_m = -\text{sign}(\nabla^2 \overline{\phi})$, $\sigma_m = \overline{\sigma}$.

V. MODELS FOR SUBGRID CROSS-TERMS

The success of the LES formalism depends considerably upon the fidelity of $\tau_{ij} = \widetilde{u_i u_j} - \widetilde{u_i} \widetilde{u_j}$, $\theta_j = \widetilde{T u_j} - \widetilde{T} \widetilde{u_j}$, $\eta_j = \widetilde{Y_V u_j} - \widetilde{Y_V} \widetilde{u_j}$ and $\sigma_{SGS}^2 = \overline{\phi\phi} - \overline{\phi\overline{\phi}}$ models in portraying the true magnitude of the unfiltered terms using the filtered variables. For LES in the gas-phase, models are required for the subgrid stresses τ_{ij} , heat fluxes θ_j , and species fluxes η_j ; for the droplet description, models are required for the subgrid variances σ_{SGS}^2 : $\widetilde{u_1 u_1} - \widetilde{u_1} \widetilde{u_1}$,

$\widetilde{u_2 u_2} - \widetilde{u_2} \widetilde{u_2}$, $\widetilde{u_3 u_3} - \widetilde{u_3} \widetilde{u_3}$, $\overline{TT} - \overline{T} \overline{T}$, $\widetilde{Y_V Y_V} - \widetilde{Y_V} \widetilde{Y_V}$ and $\overline{PP} - \overline{P} \overline{P}$. Since the subgrid stresses, the heat flux, the species flux and the subgrid variances are all of the same form, it seems reasonable and consistent to use the same type of model for them. In the following, we consider the possibility of subgrid modeling employing three different models: the traditional (e.g. constant coefficient) Smagorinsky model, the Gradient model, and the Scale-Similarity model [25]. We first define these three models below and introduce in each of the models a constant of proportionality that we further determine from comparisons of the modeled terms with the exact values of the subgrid terms as calculated from the unfiltered variables in the DNS database.

A. Smagorinsky SGS Model

In the traditional Smagorinsky model, τ_{ij} , θ_j , and η_j are expressed as (see [20])

$$\tau_{ij} = -2C_R \Delta^2 \sqrt{\tilde{S}_{kl} \tilde{S}_{kl}} \left(\tilde{S}_{ij} - \frac{1}{3} \tilde{S}_{kk} \delta_{ij} \right) \quad (59)$$

$$\theta_j = -\frac{C_R \Delta^2}{\text{Pr}} \sqrt{\tilde{S}_{kl} \tilde{S}_{kl}} \frac{\partial \overline{T}}{\partial x_j} \quad (60)$$

$$\eta_j = -C_R \Delta^2 \sqrt{\tilde{S}_{kl} \tilde{S}_{kl}} \frac{\partial \tilde{Y}_V}{\partial x_j} \quad (61)$$

where C_R is a model constant and Δ is a filter width. In eqs. 59 - 61 the rate-of-strain tensor for the filtered velocities is defined as

$$\tilde{S}_{ij} = \frac{1}{2} \left(\frac{\partial \tilde{u}_i}{\partial x_j} + \frac{\partial \tilde{u}_j}{\partial x_i} \right). \quad (62)$$

We note that this form is the basis for most SGS models, concerned only with flow dynamics, but that it cannot be easily extended to compute the subgrid variances for T, P and Y_V .

B. Gradient SGS Model

In contrast to the traditional Smagorinsky model, the gradient model (e.g. Liu et al. [12]) defined by

$$\tau_{ij} = C_G \Delta^2 \frac{\partial \tilde{u}_i}{\partial x_k} \frac{\partial \tilde{u}_j}{\partial x_k} \quad (63)$$

$$\theta_j = C_G \Delta^2 \frac{\partial \bar{T}}{\partial x_k} \frac{\partial \tilde{u}_j}{\partial x_k} \quad (64)$$

$$\eta_j = C_G \Delta^2 \frac{\partial \tilde{Y}_V}{\partial x_k} \frac{\partial \tilde{u}_j}{\partial x_k} \quad (65)$$

is easily extended to compute the subgrid variances for any quantity ϕ as

$$\sigma_{SGS}^2(\phi) = \overline{\phi\phi} - \bar{\phi}\bar{\phi} = C_G \Delta^2 \frac{\partial \bar{\phi}}{\partial x_k} \frac{\partial \bar{\phi}}{\partial x_k}. \quad (66)$$

Theoretically, $C_G \Delta^2$ is the moment of the filtering volume ($I_c \Delta^2$ of eq. 52) as can be seen by integrating the square of the Taylor expansion for ϕ , eq. 50, over the filtering volume, and using filtered instead of unfiltered quantities in the calculation of the derivatives. Thus, theoretically, for a cubic top-hat filter $C_G = \frac{1}{12}$.

This model is not only easily extended to calculate σ_{SGS} for all variables, but also has the advantage that the derivatives are already available from the computation of the resolved fields.

C. Scale-Similarity SGS Model

In the Scale-Similarity model, a second filter $\hat{\Delta}$ is introduced and the protocol involves refiltering the flow-field [2] with a test filter $\hat{\Delta} \geq \Delta$ (filtering at level $\hat{\Delta}$ is unweighted) to yield:

$$\tau_{ij} = C_S \left(\widehat{\tilde{u}_i \tilde{u}_j} - \hat{\tilde{u}}_i \hat{\tilde{u}}_j \right) \quad (67)$$

$$\theta_j = C_S \left(\widehat{\tilde{u}_j \bar{T}} - \hat{\tilde{u}}_j \hat{\bar{T}} \right) \quad (68)$$

$$\eta_j = C_S \left(\widehat{\tilde{u}_j \tilde{Y}_V} - \hat{\tilde{u}}_j \hat{\tilde{Y}}_V \right). \quad (69)$$

If the model were completely exact, C_S would be 1. Deviations from unity reflect therefore departures from the exact representation of τ_{ij} , θ_j and η_j computed from the DNS through eqs. 67 - 69.

Similar to the Gradient model, the Scale-Similarity model is easily extended to compute the subgrid variances for any quantity ϕ as

$$\sigma_{SGS}^2(\phi) = \overline{\phi\phi} - \overline{\phi}\overline{\phi} = C_S \left(\widehat{\overline{\phi\phi}} - \widehat{\overline{\phi}}\widehat{\overline{\phi}} \right) \quad (70)$$

D. Model Coefficients

In the following we will refer to standard deviations calculated from eq. 54 as “exact” since in this model they represent the best available values that can be calculated at the LES (i.e. filtered) scale from the unfiltered variables. Therefore, we first compute the correlation between the “exact” and model SGS standard deviations using the definitions of eqs. 45 and 46 and then determine the relationship between the “exact” and modeled variables which yields the model coefficient. Note that eq. 45 allows pointwise assessment of the correlations.

The simplest SGS model is that having a constant-coefficient with C_R, C_G, C_S being the same for all flow variables over the entire (spatial and temporal) domain. For this type of model, the coefficient can be determined using a least-squares fit to $Y = bX$ which leads to $b = \langle\langle\langle XY \rangle\rangle\rangle / \langle\langle\langle XX \rangle\rangle\rangle$. If X is the model standard deviation and Y is the “exact” standard deviation, then b is the square root of the model coefficient. More sophisticated models would have the model coefficients as functions of space and time; this will be the subject of a further investigation as we note that the simplicity of the constant coefficient models is partially offset by the fact that they yield models which are flow dependent. However, considering the lack of experience with *a priori* models for two phase flows, it is worthwhile in this first step to assess the possibility of constant model coefficients since they are the simplest to derive and use in a LES.

VI. FINALIZATION OF THE QUANTITATIVE SGS MODELS

A. Unfiltered Variable Model

As stated in eq. 48, the unfiltered variable ϕ can be expressed as $\phi = \bar{\phi} + f\sigma$, where $\sigma = |\phi - \bar{\phi}|$ and $f = \text{sign}(\phi - \bar{\phi})$, and we showed in eq. 58 a possible model for $f\sigma$ (denoted $f_m\sigma_m$) that has the potential of being more accurate than that obtained from a simple extrapolation of the filtered gas phase variables at the droplet locations (i.e. $f_m\sigma_m = 0$). The proposed model will be now used to first compute ϕ for all dependent variables at the Eulerian grid points, and then interpolate it to the droplet locations.

Figure 7 shows the probability density function (PDF) for $(\phi - \bar{\phi})/\bar{\sigma}$ for case TP600 with ϕ being u_1, u_2, u_3, T, Y_V and P , where $\bar{\sigma} = \sqrt{\bar{\sigma}^2}$ is calculated from the filtered field using eq. 57. Figure 8 shows the PDF for $(\phi - \bar{\phi})/\sigma_{SGS}$. Although the correlation between σ and $\bar{\sigma}$ is similar to that between σ and σ_{SGS} (ranging from 0.6 to 0.8), the $(\phi - \bar{\phi})/\bar{\sigma}$ and $(\phi - \bar{\phi})/\sigma_{SGS}$ PDF are remarkably different. The PDF for $(\phi - \bar{\phi})/\sigma_{SGS}$ shows one very large peak at zero, whereas that for $(\phi - \bar{\phi})/\bar{\sigma}$ shows peaks at ± 1 , similar to the PDF of $(\phi - \bar{\phi})/\sigma$ which has values of ± 1 . This confirms $\bar{\sigma}$ to be an appropriate model for σ , but implies that σ and σ_{SGS} are only moderately correlated. Closer examination of the PDF of $(\phi - \bar{\phi})/\bar{\sigma}$ in the $(x_1 - x_3)$ plane (not shown) reveals the large Y_V peak at zero to be due to the upper stream region where $Y_V = 0$, whereas the small u_1, u_2 and u_3 peaks at zero correspond to the lower edge of the mixing layer, where freestream droplets are being entrained. For all variables except Y_V , the PDFs of $(\phi - \bar{\phi})/\bar{\sigma}$ in the droplet free domain are focused on ± 1 , but have a larger variation between -1 and $+1$ in the droplet laden part.

Figure 9 shows the comparison between interpolating the gas dependent variables to the droplet locations using the exact quantities (unfiltered DNS), and interpolating the same variables using other models to the droplet locations. Results are presented in terms of the difference between the model and the unfiltered variable, averaged over droplets within a given x_2 -interval and denoted by $\langle\langle \rangle\rangle$. In the first three models $\sigma_m = \sigma$ with σ given

by eq. 47 (and therefore it is evaluated from the unfiltered variables which are not available in LES) with the purpose of comparing and evaluating the validity of the models for f . Clearly, $f_m = 0$ leads to significant discrepancy between the exact and model interpolated variable; any model with $f_m = 0$ will not perform any better since the deviations toward the unfiltered value will be just as likely as the deviations away from the unfiltered values. This is illustrated in Fig. 9 by the case where f_m randomly assumes the values -1 or $+1$; its predictions generally lead the largest deviations and its performance is slightly worse than $f_m = 0$ despite having the exact σ . Using $f_m = -\text{sign}(\nabla^2 \bar{\phi})$ gives significant improvement despite the two assumptions that $f_m = -\text{sign}(\nabla^2 \phi)$ and $\text{sign}(\nabla^2 \phi) = \text{sign}(\nabla^2 \bar{\phi})$; for the data shown in Fig. 9, these assumptions hold with 86%, 86%, 86%, 85%, 86% and 93% certainty for u_1, u_2, u_3, T, Y_V , and P respectively. When σ is replaced by $\bar{\sigma}$ (denoted $[\sigma]$ in the figures), while $f_m = -\text{sign}(\nabla^2 \bar{\phi})$, there is considerable improvement over the predictions obtained with $f_m = 0$, for all quantities except T for which all models give similar results. For T, Y_V and P , equivalent results are obtained with the two sets ($f_m = 1, \sigma_m = \sqrt{\phi\phi} - \sqrt{\bar{\phi}\bar{\phi}}$) and ($f_m = -\text{sign}(\nabla^2 \bar{\phi}), \sigma_m = \bar{\sigma}$) where $\bar{\sigma} = \sqrt{\bar{\sigma}^2} = \left| \sqrt{\phi\phi} - \sqrt{\bar{\phi}\bar{\phi}} \right|$ is calculated as in eq. 57; in Fig. 9 we have defined ‘signed $[\sigma]$ ’ = $\sqrt{\phi\phi} - \sqrt{\bar{\phi}\bar{\phi}}$. An alternative expression for f_m , $f_m = \text{sign}(\phi - \bar{\phi}) = \text{sign}(\bar{\phi} - \bar{\bar{\phi}})$, is inspired by the Scale-Similarity relations and results in a similar accuracy to using $f_m = -\text{sign}(\nabla^2 \bar{\phi})$ for all six variables.

The primary conclusion from the comparison of results obtained with modeled f and σ (the only possibility within LES) is that the “exact” model proposed in eq. 58 is the most accurate at simulating the unfiltered gas phase variables as a function of the same filtered variables. Moreover, an analysis of the correlation $\mathcal{R}(\phi, \bar{\phi})$ defined by eq. 56 shows that $\mathcal{R} = 1$ for T and P , $0.97 < \mathcal{R} < 1$ for u_1, u_2 and u_3 , with the greatest deviation from 1 appearing in the central part of the mixing layer; and $0.7 < \mathcal{R} < 1$ for Y_V , with the greatest deviation being obtained at the droplet-laden/droplet-free interface. The low Y_V correlation is due to the sparsity of drops, producing a Y_V which reduces the quality of the statistics. Since apparently $\mathcal{R} < 1$ for Y_V , we tried unsuccessfully to improve the modeling of the unfiltered quantities through the filtered quantities by slightly reducing \mathcal{R} .

Not only was the model with $\mathcal{R} < 1$ generally inferior, but even at the interface where the greatest deviation from unity was obtained, $\mathcal{R} = 1$ led to the best prediction of Y_V at droplet locations. Most important, $\mathcal{R} = 1$ is the only value that provides the correct $\bar{\sigma} \simeq 0$ in the laminar freestream. Finally, we note that the efforts at reducing the error for the approximation of eq. 58 through the reduction in the error in Y_V are misplaced since the total model error is determined by that of the velocity components which are the largest (about 1.5%); in contrast, the temperature, mass fraction and pressure have errors an order of magnitude lower. Given these observations, it is unlikely that increased accuracy would be obtained even if a model with a variable \mathcal{R} (according to the dependent variable) could be constructed.

B. Determination of SGS Model Constants

Illustrated in Fig. 10 are the subgrid scale stresses calculated from the DNS, those predicted by the Smagorinsky model, and the correlation between the DNS calculated values and the model predictions calculated according to eq. 45. The lack of good correlation between the DNS and predicted stresses is not surprising considering that even for single phase flow global correlations are in the range of 0.4 (see [4] and [24]). Since in the present situation local rather than global correlations are of interest because the unfiltered variable model requires good local values of σ_{SGS} for computing $\bar{\sigma}$, the lack of good local correlation induced us to discard the Smagorinsky model.

Both the Gradient and the Scale-Similarity models are assessed in Figs. 11 - 13 where the normalized σ_{SGS} planar averages are shown in Figs. 11, 12 and 13 for cases TP500a, TP500b and TP600 respectively and σ_{SGS} is calculated either from the unfiltered values or using the models. For the sake of optimizing the Scale-Similarity model, we also consider several test-to-LES filter ratios, as the best value recommended in the literature is usually 2 (e.g. [24]). The model coefficients used in all plots in Figs. 11 - 13 are the mean values — C_G listed in Table VII for the gradient model and C_S listed in Table VIII for the Scale-Similarity

model. To find these model coefficients listed in Tables VII and VIII, linear fits of the exact σ_{SGS} to the model σ_{SGS} over the whole domain were performed. Since for the temperature the SGS deviations were underpredicted, the model coefficients were replaced by $C_G \text{Pr}$ in eq. 66 and $C_S \text{Pr}$ in eq. 70, where the Prandtl number is $\text{Pr} = 0.7$ for the present flow conditions. For all variables and all filter ratios of the Scale-Similarity model, as well as for the Gradient model, the prediction of σ_{SGS} is very good, with that from the Scale-Similarity model being slightly superior. The only exception to this good agreement occurs for the temperature (see Figs. 11d, 12d and 13d) when the Scale-Similarity model with filter width ratio $\hat{\Delta}/\Delta = 1$ is used. This is not completely surprising since as mentioned above, most investigators using a similarity model recommend $\hat{\Delta}/\Delta = 2$.

Along with the individual SGS model constants for each set of DNS results, we also show in Tables VII and VIII the recommended mean constants for all runs. For the gradient model, the mean value of $\sqrt{C_G} = 0.4$ is approximately 40% larger than the theoretical value of $\sqrt{C_G} = 1/\sqrt{12} \simeq 0.29$ for the cubic filter. The discrepancy between the model and theoretical values is attributed to departures from the behavior assumed by the Gradient model, most notably to the replacement of unfiltered by filtered quantities in the calculation of the derivatives (as stated when formulating the model). For the Scale-Similarity model, a linear best fit gives $\sqrt{C_S} = 1.71 - 0.49(\hat{\Delta}/\Delta)$, however, with only three values for this fit, it is recommended to use the computed coefficients rather than the linear best fit. In particular, for $\hat{\Delta}/\Delta = 1$ we find that $\sqrt{C_S} \neq 1$, indicating that $\overline{\bar{\phi}} = \bar{\phi}$ is not a good assumption. Consistent with the previous discussion on the model for the unfiltered variables using the filtered variables, Figs. 11 - 13 show that the σ_{SGS} are largest for the velocity components whereas those for Y_V , T and P are an order of magnitude smaller.

VII. CONCLUSIONS

An *a priori* subgrid analysis has been presented for a temporally developing mixing layer with evaporating droplets by employing a DNS database for three Reynolds number (based

on vorticity thickness) and mass loading combinations: (500; 0.2), (500; 0.5) and (600; 0.2). The DNS equations were filtered, and LES equations were constructed subject to several assumptions. These assumptions were evaluated by calculating the exact filtered expressions and their filtered models for the three sets of results in the database, as well as the other terms in the equations. The comparison among these terms showed that the assumptions used to derive the final set of LES equations were well justified. For example, an order of magnitude analysis of the terms in these equations showed that the subgrid terms arising from filtering the inviscid terms are smaller only than the inviscid terms based on filtered quantities. However, the subgrid terms arising from filtering the viscous terms were found to be negligible. The triple correlation of velocity, mass fraction and temperature is found to be well modeled as the temperature multiplied by the mass fraction-velocity correlation.

Within the LES formalism for two phase flows, it was found that there are two modeling issues in addition to the usual modeling of the SGS terms. One of these modeling issues, which is that the unfiltered gas phase dependent variables at the drop locations must be derived from the LES filtered variables, was addressed as a preliminary to SGS modeling. For each gas phase variable, several constructs for the unfiltered value as function of the filtered value were considered, and it was shown that the most accurate is that with a standard deviation having the magnitude of the filtered standard deviation and the opposite sign of the Laplacian of the filtered variable. With this model, predictions for the unfiltered variables at the droplet locations were found to be considerably improved compared to simply interpolating the filtered variables.

To model the subgrid scale (SGS) standard deviations, two models, the Gradient and Scale-Similarity, were found to give excellent results when the model constant was properly calculated using the database, while the traditional Smagorinsky model was found inadequate. More sophisticated dynamic models, where the present constant is replaced by a functional dependence of the filtered variables will be considered in the future. Statistical analysis of the database showed that the gradient model is well represented by the same model constant for all three cases. For the similarity model, the constant was found, as

expected, to be dependent on the test-to-LES filter ratio.

Future work will address dynamic SGS modeling as well as the second issue in two phase flow LES calculations which is that of the computation of the averaged source terms from the filtered dependent variables. Once this issue is resolved, we will conduct an *a posteriori* testing of the Gradient and Scale-Similarity models in an LES.

VIII. ACKNOWLEDGMENTS

This research was conducted at the Jet Propulsion Laboratory (JPL) of the California Institute of Technology (Caltech) under the sponsorship of General Electric (GE) through the Air Force Office of Scientific Research (AFOSR) Focused Research Initiative program with Dr. Hukam Mongia from GE serving as contract monitor. Computations were performed using the Caltech Center for Advanced Computing Research (CACR) parallel HP Exemplar.

REFERENCES

- [1] A. Ansari and W. Z. Strang. Large-Eddy Simulation of Turbulent Mixing Layers. Technical Report 96-0684, AIAA, 1996.
- [2] J. Bardina, J. H. Ferziger, and W. C. Reynolds. Improved Subgrid Scale Models for Large Eddy Simulation. Technical Report 80-1357, AIAA, 1980.
- [3] M. Boivin, O. Simonin, and K. D. Squires. Direct Numerical Simulation of Turbulence Modulation by Particles in Isotropic Turbulence. *J. Fluid Mech.*, 375:235–263, 1998.
- [4] R. A. Clark, J. H. Ferziger, and W. C. Reynolds. Evaluation of Subgrid-Scale Models Using an Accurately Simulated Turbulent Flow. *J. Fluid Mech.*, 91(1):1–16, 1979.
- [5] C. T. Crowe, T. R. Troutt, and J. N. Chung. Numerical Models for Two-Phase Turbulent Flows. *Annual Review of Fluid Mechanics*, 28:11–43, 1996.
- [6] E. Deutsch and O. Simonin. Large Eddy Simulation Applied to the Modelling of Particulate Transport Coefficients in Turbulent Two-Phase Flows. In *Eighth Symposium on Turbulent Shear Flows*, pages 10–1:1–6, September 1991.
- [7] S. Elghobashi and G. C. Truesdell. On the Two-Way Interaction Between Homogeneous Turbulence and Dispersed Solid Particles. I: Turbulence Modification. *Phys. Fluids A*, 5(7):1790–1801, 1993.
- [8] G. Erlebacher, M. Y. Hussaini, C. G. Speziale, and T. A. Zang. Toward the Large-Eddy Simulation of Compressible Turbulent Flows. *J. Fluid Mech.*, 238:155–185, 1992.
- [9] T. Goutorbe and D. Laurence. Modelling Anisotropy and Backscatter Effects in the Subgrid Scale Stress Tensor. EDF Technical Report 96NB00003
- [10] F. F. Grinstein and K. Kailasanath. Three-Dimensional Numerical Simulations of Unsteady Reactive Square Jets. *Combust. Flame*, 100:2–10, 1995.
- [11] D. Hansell, I. M. Kennedy, and W. Kollmann. A Simulation of Particle Dispersion in a

- Turbulent Jet. *Int. J. Multiphase Flow*, 18(4):559–576, 1992.
- [12] S. Liu, C. Meneveau, and J. Katz. On the Properties of Similarity Subgrid-Scale Models as Deduced from Measurements in a Turbulent Jet. *J. Fluid Mech*, 275:83–119, 1994.
 - [13] F. Mashayek. Droplet-Turbulence Interactions in Low-Mach-Number Homogeneous Shear Two-Phase Flows. *J. Fluid Mech.*, 367:163–203, 1998.
 - [14] R. S. Miller and J. Bellan. Direct Numerical Simulation and Subgrid Analysis of a Transitional Droplet Laden Mixing Layer. Submitted to *Physics of Fluids*, 1999.
 - [15] R. S. Miller and J. Bellan. Direct Numerical Simulation of a Confined Three-Dimensional Gas Mixing Layer with One Evaporating Hydrocarbon-Droplet Laden Stream. *J. Fluid Mech.*, 384:293–338, 1999.
 - [16] R. D. Moser, and M. M. Rogers, Mixing Transition and the Cascade to Small Scales in a Plane Mixing Layer *Phys. Fluids A* **3(5)**, 1128-1134, 1991.
 - [17] S. Pannala and S. Menon. Large Eddy Simulations of Two-Phase Turbulent Flows, Technical Report, AIAA 98-0163.
 - [18] T. J. Poinso and S. K. Lele. Boundary Conditions for Direct Simulations of Compressible Viscous Flows. *J. Computational Physics*, 101:104–129, 1992.
 - [19] O. Simonin, E. Deutsch, and M. Boivin. Large Eddy Simulation and Second-Moment Closure of Particle Fluctuating Motion in Two-Phase Turbulent Shear Flows. *Turbulent Shear Flows*, 9:85–115, 1993.
 - [20] J. Smagorinsky. Some Historical Remarks on the Use of Nonlinear Viscosities. In B. Galperin and S. A. Orszag, editors, *Large Eddy Simulation of Complex Engineering and Geophysical Flows*, chapter 1, pages 3–36. Cambridge University Press, 1993.
 - [21] K. D. Squires and J. K. Eaton. Particle Response and Turbulence Modification in Isotropic Turbulence. *Phys. Fluids A*, 2(7):1191–1203, 1990.

- [22] G. C. Truesdell and S. Elghobashi. On the Two-Way Interaction Between Homogeneous Turbulence and Dispersed Solid Particles. II. Particle Dispersion. *Phys. Fluids A*, 6(3):1405–1407, 1994.
- [23] W. S. J. Uijttewaai and R. V. A. Oliemans. Particle Dispersion and Deposition in Direct Numerical and Large Eddy Simulations of Vertical Pipe Flows. *Phys. Fluids* 8(10):2590–2604, 1996.
- [24] B. Vreman, B. Geurts, and H. Kuerten. A Priori Tests of Large Eddy Simulation of the Compressible Plane Mixing Layer. *Journal of Engineering Mathematics*, 29:299–327, 1995.
- [25] B. Vreman, B. Geurts, and H. Kuerten. Large-Eddy Simulation of the Turbulent Mixing Layer. *J. Fluid Mech.*, 339:357–390, 1997.
- [26] Q. Wang and K. D. Squires. Large Eddy Simulation of Particle Deposition in a Vertical Turbulent Channel Flow, *Int. J. Multiphase Flow*, 22(4):667–683, 1996.
- [27] Q. Wang and K. D. Squires. Large Eddy Simulation of Particle-Laden Turbulent Channel Flow, *Phys. Fluids* 8(5):1207–1223, 1996.
- [28] Q. Wang and K. D. Squires. Transport of Heavy Particles in a Three-Dimensional Mixing Layer. *J. Fluids Eng.* 120:613–620, 1998.
- [29] Q. Wang, K. D. Squires, and O. Simonin. Large Eddy Simulation of Turbulent Gas-Solid Flows in a Vertical Channel and Evaluation of Second-Order Models. *International Journal of Heat and Fluid Flow*, 19:505–511, 1998.
- [30] F. Yeh and U. Lei. On the Motion of Small Particles in a Homogeneous Turbulent Shear Flow, *Phys. Fluids A*, 3(11):2758–2776, 1991.

TABLES

Case	Re	ML	Grid	Time
TP500a	500	0.2	252×276×152	85.0
TP500b	500	0.5	252×276×152	85.0
TP600	600	0.2	300×332×180	86.2

TABLE I. Summary of DNS Database

$\bar{\rho} \tilde{u}_1$ Equation ($i = 1$)	TP500a	TP500b	TP600
$\frac{\partial \bar{\rho} \tilde{u}_i \tilde{u}_j}{\partial x_j}$	3.9×10^5	4.0×10^5	4.4×10^5
$\frac{\partial \bar{P} \delta_{ij}}{\partial x_j}$	3.4×10^5	3.4×10^5	3.5×10^5
$\frac{\partial \bar{\rho} \tau_{ij}}{\partial x_j}$	7.1×10^4	7.9×10^4	7.1×10^4
$\frac{\partial \bar{\sigma}_{ij}}{\partial x_j}$	1.5×10^4	1.7×10^4	2.0×10^4
$\bar{S}_{II,i}$	1.2×10^4	3.6×10^4	1.3×10^4
$\frac{\partial (\bar{\sigma}_{ij} - \tilde{\sigma}_{ij})}{\partial x_j}$	9.4×10^2	1.6×10^3	1.1×10^3

TABLE II. Magnitude (Root-mean-square) of terms in filtered x_1 momentum equation

$\bar{\rho} \tilde{u}_2$ Equation ($i = 2$)	TP500a	TP500b	TP600
$\frac{\partial \bar{\rho} \tilde{u}_i \tilde{u}_j}{\partial x_j}$	4.3×10^5	4.0×10^5	4.7×10^5
$\frac{\partial \bar{P} \delta_{ij}}{\partial x_j}$	3.7×10^5	3.2×10^5	3.5×10^5
$\frac{\partial \bar{\rho} \tau_{ij}}{\partial x_j}$	7.7×10^4	7.8×10^4	7.5×10^4
$\frac{\partial \bar{\sigma}_{ij}}{\partial x_j}$	1.5×10^4	1.6×10^4	2.0×10^4
$\bar{S}_{II,i}$	1.1×10^4	2.7×10^4	1.1×10^4
$\frac{\partial (\bar{\sigma}_{ij} - \tilde{\sigma}_{ij})}{\partial x_j}$	2.8×10^3	3.0×10^3	3.1×10^3

TABLE III. Magnitude (Root-mean-square) of terms in filtered x_2 momentum equations

$\bar{\rho}\tilde{u}_3$ Equation ($i = 3$)	TP500a	TP500b	TP600
$\frac{\partial \bar{\rho}\tilde{u}_i\tilde{u}_j}{\partial x_j}$	3.8×10^5	3.7×10^5	4.5×10^5
$\frac{\partial \bar{P}\delta_{ij}}{\partial x_j}$	2.8×10^5	2.8×10^5	3.1×10^5
$\frac{\partial \bar{\rho}\tau_{ij}}{\partial x_j}$	5.8×10^4	6.5×10^4	6.7×10^4
$\frac{\partial \bar{\sigma}_{ij}}{\partial x_j}$	1.4×10^4	1.4×10^4	1.9×10^4
$\bar{S}_{II,i}$	7.5×10^3	2.6×10^4	8.1×10^3
$\frac{\partial(\bar{\sigma}_{ij} - \tilde{\sigma}_{ij})}{\partial x_j}$	5.8×10^2	8.7×10^2	7.3×10^2

TABLE IV. Magnitude (Root-mean-square) of terms in filtered x_3 momentum equation

$\bar{\rho}\tilde{E}$ Equation	TP500a	TP500b	TP600
$\frac{\partial(\bar{\rho}\tilde{E} + \bar{P})\tilde{u}_j}{\partial x_j}$	2.6×10^8	2.8×10^8	3.3×10^8
$\frac{\partial[(\bar{\rho}E + \bar{P})u_j - (\bar{\rho}\tilde{E} + \bar{P})\tilde{u}_j]}{\partial x_j}$	1.7×10^8	1.9×10^8	2.0×10^8
\bar{S}_{III}	1.7×10^7	2.9×10^7	1.9×10^7
$\frac{\partial}{\partial x_j} \left(\lambda \frac{\partial \bar{T}}{\partial x_j} \right)$	1.2×10^7	1.7×10^7	1.6×10^7
$\frac{\partial \tilde{u}_i\tilde{\sigma}_{ij}}{\partial x_j}$	1.9×10^6	2.0×10^6	2.4×10^6
$\frac{\partial \tilde{u}_i\bar{\sigma}_{ij}}{\partial x_j}$	1.8×10^6	1.9×10^6	2.4×10^6
$\frac{\partial(\tilde{u}_i\bar{\sigma}_{ij} - \tilde{u}_i\tilde{\sigma}_{ij})}{\partial x_j}$	7.6×10^5	8.5×10^5	9.1×10^5

TABLE V. Magnitude (Root-mean-square) of terms of filtered energy equation

$\bar{\rho}\tilde{Y}_V$ Equation	TP500a	TP500b	TP600
$\frac{\partial \bar{\rho}\tilde{Y}_V\tilde{u}_j}{\partial x_j}$	1.5×10^2	1.8×10^2	2.0×10^2
$\frac{\partial \bar{\rho}\eta_{ij}}{\partial x_j}$	2.8×10^1	3.4×10^1	2.8×10^1
\bar{S}_I	2.0×10^1	3.2×10^1	2.2×10^1
$\frac{\partial}{\partial x_j} \left(\bar{\rho}\Gamma \frac{\partial \tilde{Y}_V}{\partial x_j} \right)$	1.2×10^1	1.6×10^1	1.6×10^1
$\frac{\partial}{\partial x_j} \left(\rho\Gamma \frac{\partial Y_V}{\partial x_j} \right)$	1.1×10^1	1.3×10^1	1.4×10^1
$\frac{\partial}{\partial x_j} \left(\rho\Gamma \frac{\partial Y_V}{\partial x_j} \right) - \frac{\partial}{\partial x_j} \left(\bar{\rho}\Gamma \frac{\partial \tilde{Y}_V}{\partial x_j} \right)$	6.2×10^0	1.1×10^1	7.8×10^0

TABLE VI. Magnitude (Root-mean-square) of terms of filtered species equation

	TP500a	TP500b	TP600	Mean
Δ	3.200×10^{-3}	3.200×10^{-3}	2.667×10^{-3}	
$\sqrt{C_G}$	0.397	0.398	0.402	0.40

TABLE VII. Coefficient for Gradient Model

$\hat{\Delta}/\Delta$	TP500a	TP500b	TP600	Mean $\sqrt{C_S}$
1.0	1.237	1.253	1.243	1.24
1.5	0.921	0.931	0.925	0.93
2.0	0.751	0.759	0.755	0.75

TABLE VIII. Coefficient for Similarity Model

FIGURES

FIG. 1. Planar RMS of filtered terms, Case TP600 a) x_1 -momentum b) x_2 -momentum c) x_3 -momentum d) Energy, e) Mass fraction

FIG. 2. Evaluation of assumption $\overline{\rho u_i u_i u_j} - \overline{\rho u_i u_i} \tilde{u}_j = \bar{\rho} \tau_{ij} \tilde{u}_i$ a) $j = 1$ b) $j = 2$ c) $j = 3$

FIG. 3. Evaluation of assumptions $\bar{T} = \tilde{T}$ and $\widetilde{Y_V T} = \tilde{Y}_V \bar{T}$ a) \bar{T} b) $\tilde{Y}_V \bar{T}$ c) RMS of differences

FIG. 4. Evaluation of assumptions regarding $\overline{\rho Y_V T u_j} - \overline{\rho Y_V T} \tilde{u}_j$ a) $j = 1$ b) $j = 2$ c) $j = 3$

FIG. 5. Evaluation of assumption $\overline{u_i \sigma_{ij}} = \tilde{u}_i \tilde{\sigma}_{ij}$ a) $j = 1$ b) $j = 2$ c) $j = 3$

FIG. 6. Evaluation of assumption $\overline{\rho \partial Y_V / \partial x_j} = \bar{\rho} \partial \tilde{Y}_V / \partial x_j$ a) $j = 1$ b) $j = 2$ c) $j = 3$

FIG. 7. PDF of $(\phi - \bar{\phi}) / \bar{\sigma}$ a) u_1, u_2, u_3 b) T, P, Y_V

FIG. 8. PDF of $(\phi - \bar{\phi}) / \sigma_{SGS}$ a) u_1, u_2, u_3 b) T, P, Y_V

FIG. 9. Error in unfiltered variable model $\phi = \bar{\phi} + f_m \sigma_m$ interpolated to droplet locations, Case TP600 a) u_1 b) u_2 c) u_3 d) T e) Y_V f) P

FIG. 10. Subgrid stresses, Case TP600 a) Exact b) Smagorinsky c) Correlation between exact and Smagorinsky stresses

FIG. 11. SGS standard deviation, Case TP500a a) u_1 b) u_2 c) u_3 d) T e) Y_V f) P

FIG. 12. SGS standard deviation, Case TP500b a) u_1 b) u_2 c) u_3 d) T e) Y_V f) P

FIG. 13. SGS standard deviation, Case TP600 a) u_1 b) u_2 c) u_3 d) T e) Y_V f) P

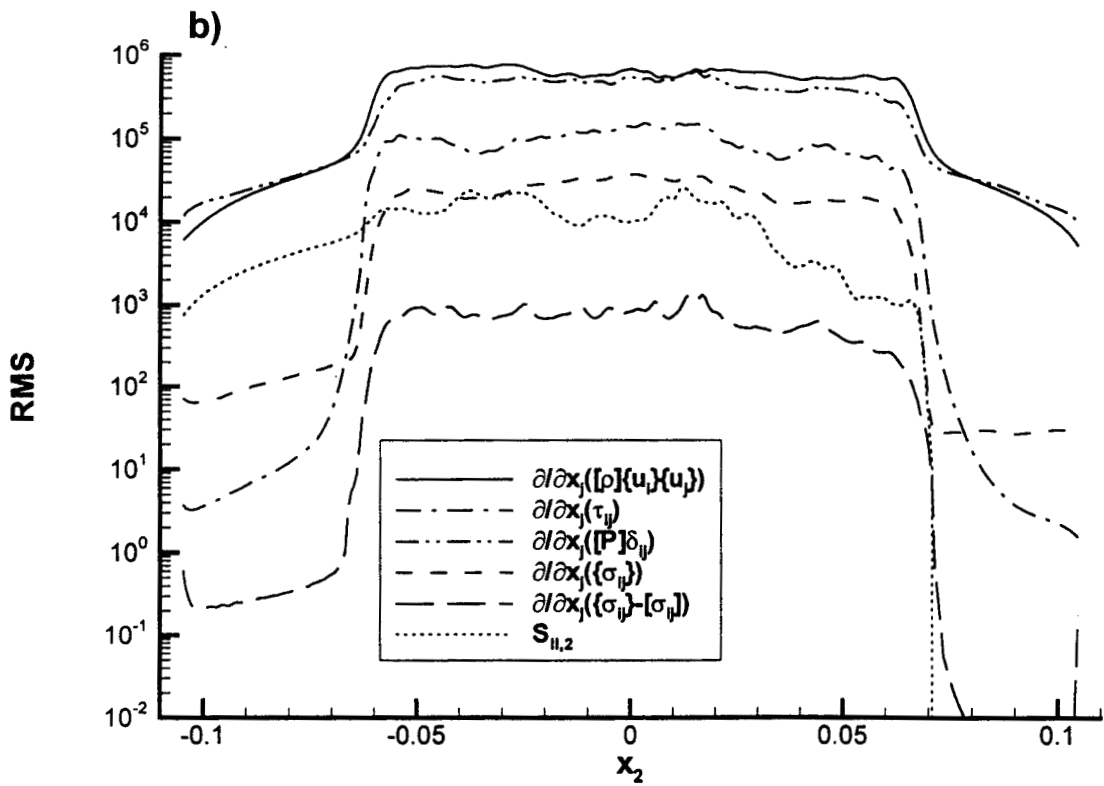
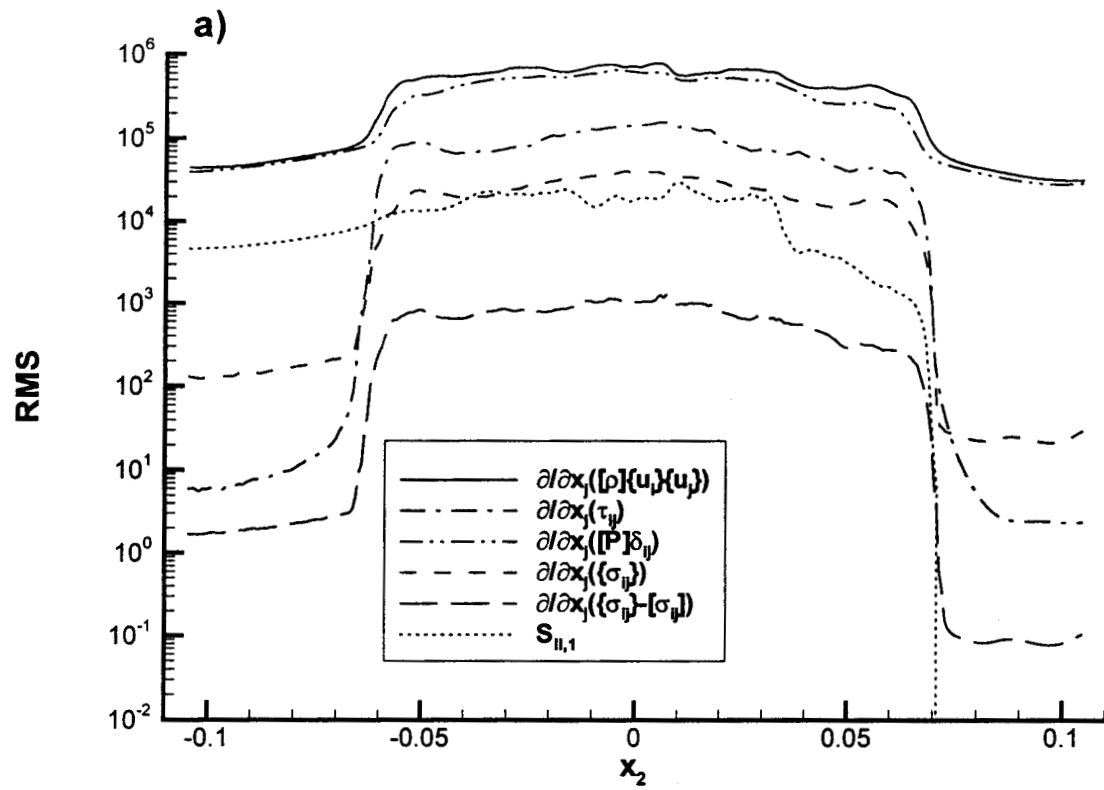


Figure 1. Planar RMS of filtered terms, Case TP600 a) x_1 -momentum b) x_2 -momentum c) x_3 momentum d) energy e) mass fraction

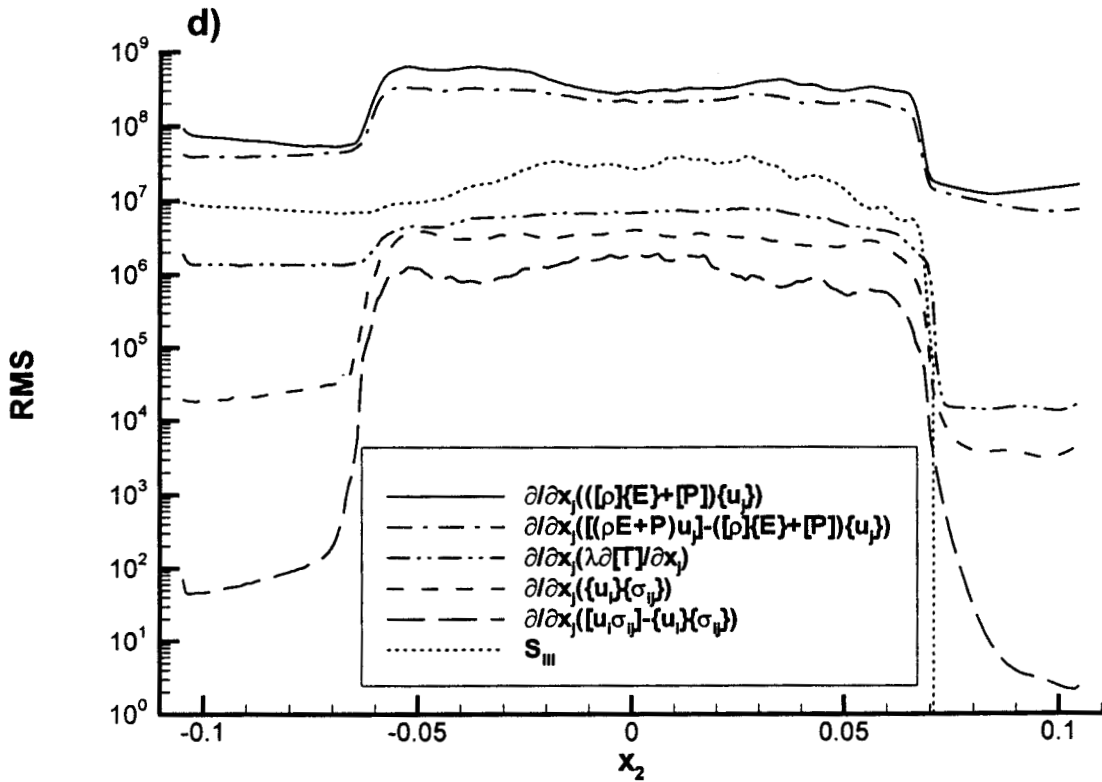
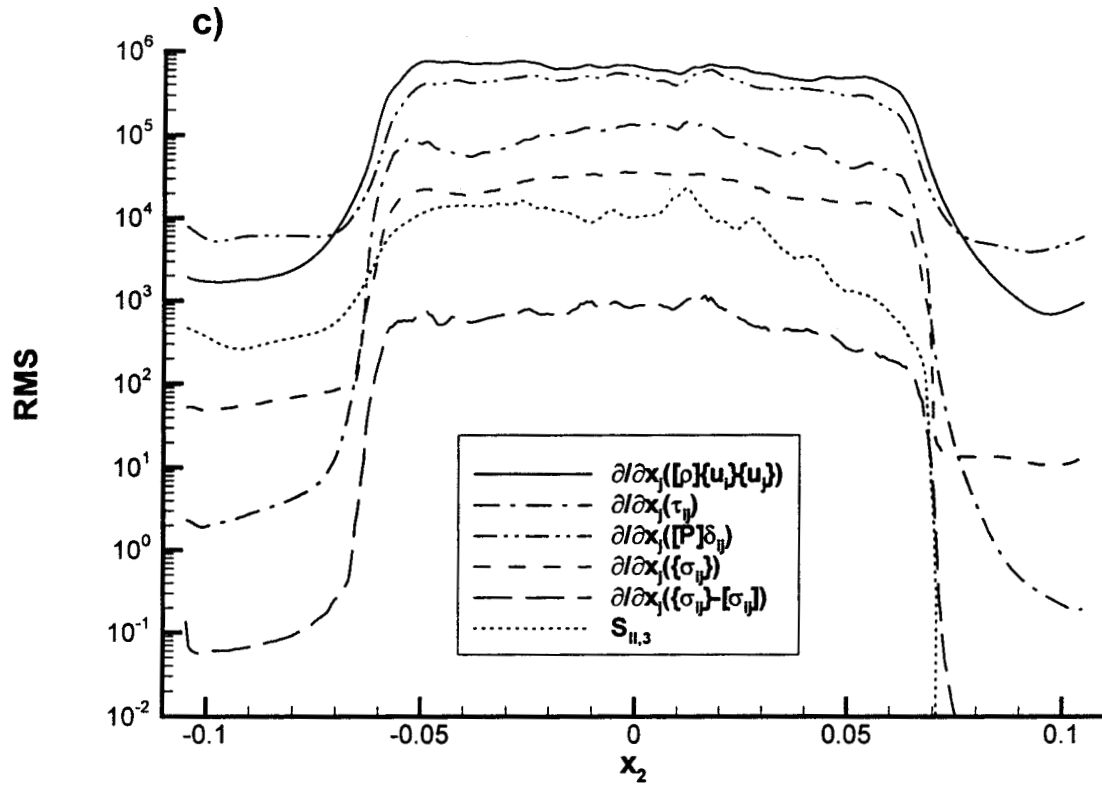


Figure 1. Planar RMS of filtered terms, Case TP600 a) x_1 -momentum b) x_2 -momentum c) x_3 momentum d) energy e) mass fraction

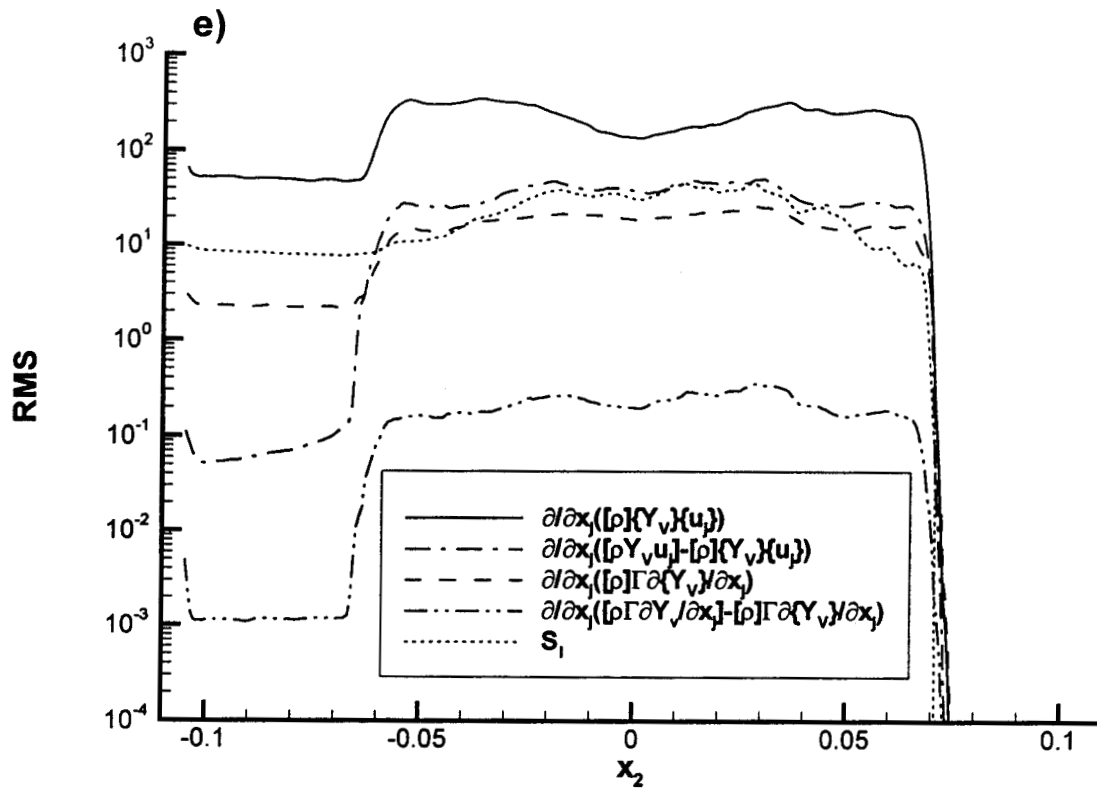


Figure 1. Planar RMS of filtered terms, Case TP600 a) x_1 -momentum
b) x_2 -momentum c) x_3 momentum d) energy e) mass fraction

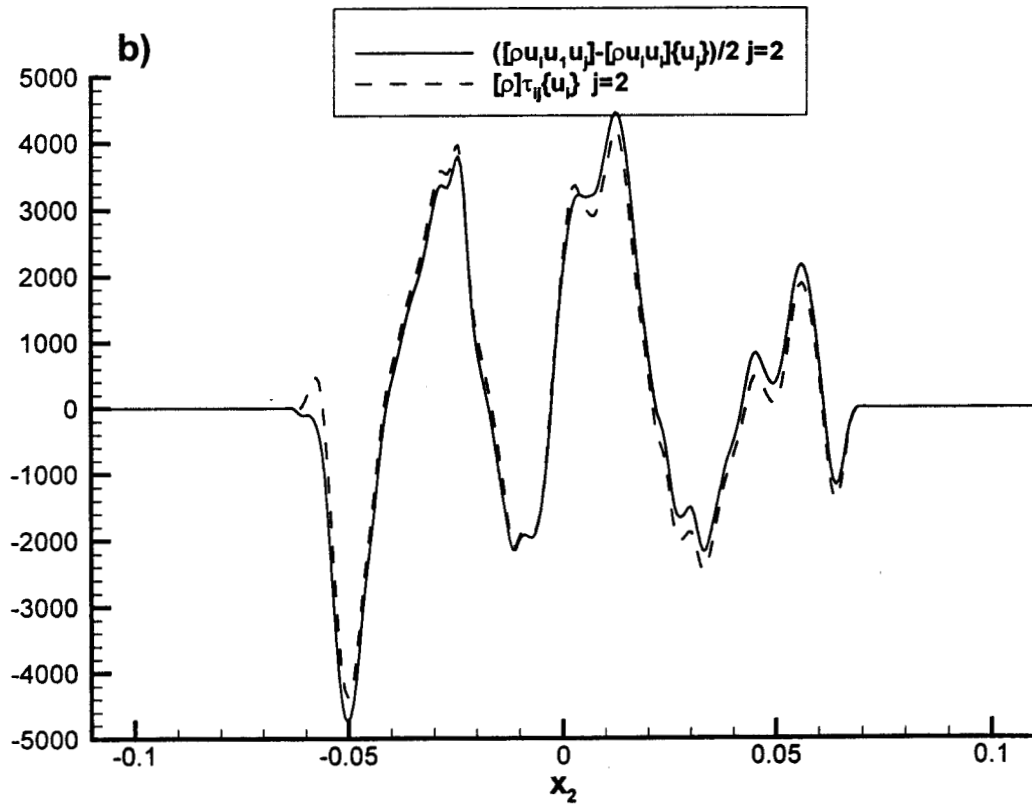
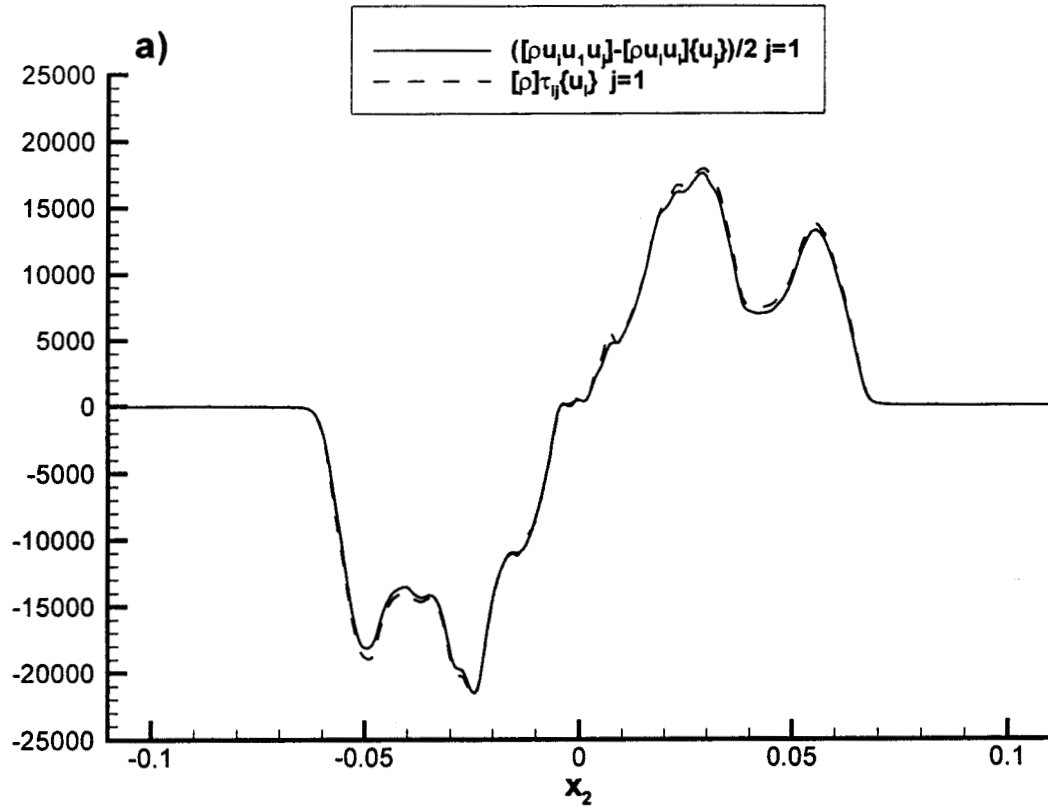


Figure 2. Evaluation of assumption $\overline{\rho u_i u_i} - \overline{\rho u_i} \tilde{u}_i = \overline{\rho} \tau_{ij} \tilde{u}_i$
a) $j=1$ b) $j=2$ c) $j=3$

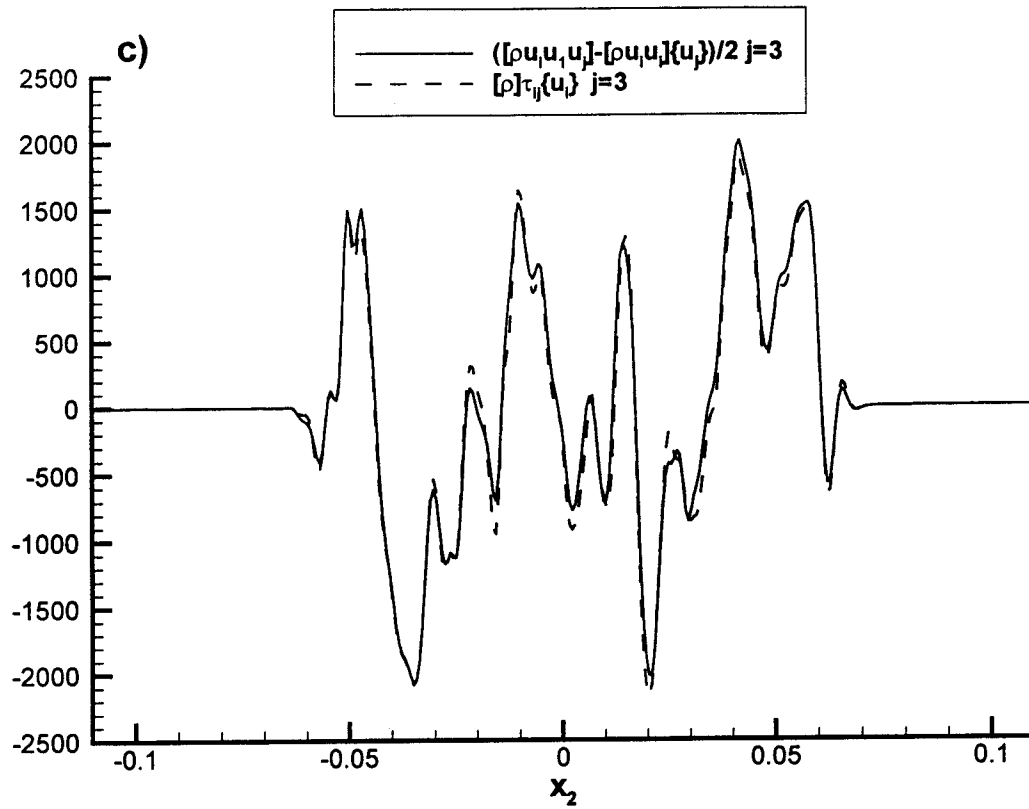


Figure 2. Evaluation of assumption $\overline{\rho u_i u_i u_j} - \overline{\rho u_i u_j} \tilde{u}_i = \rho \tau_{ij} \tilde{u}_i$
a) $j=1$ b) $j=2$ c) $j=3$

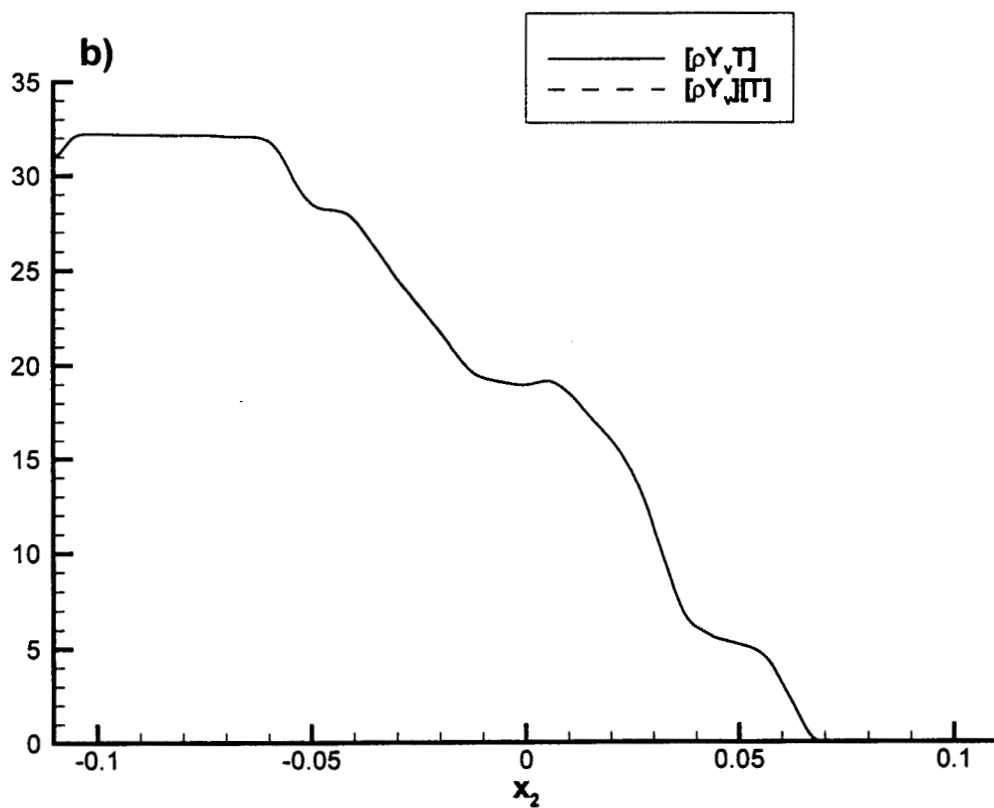
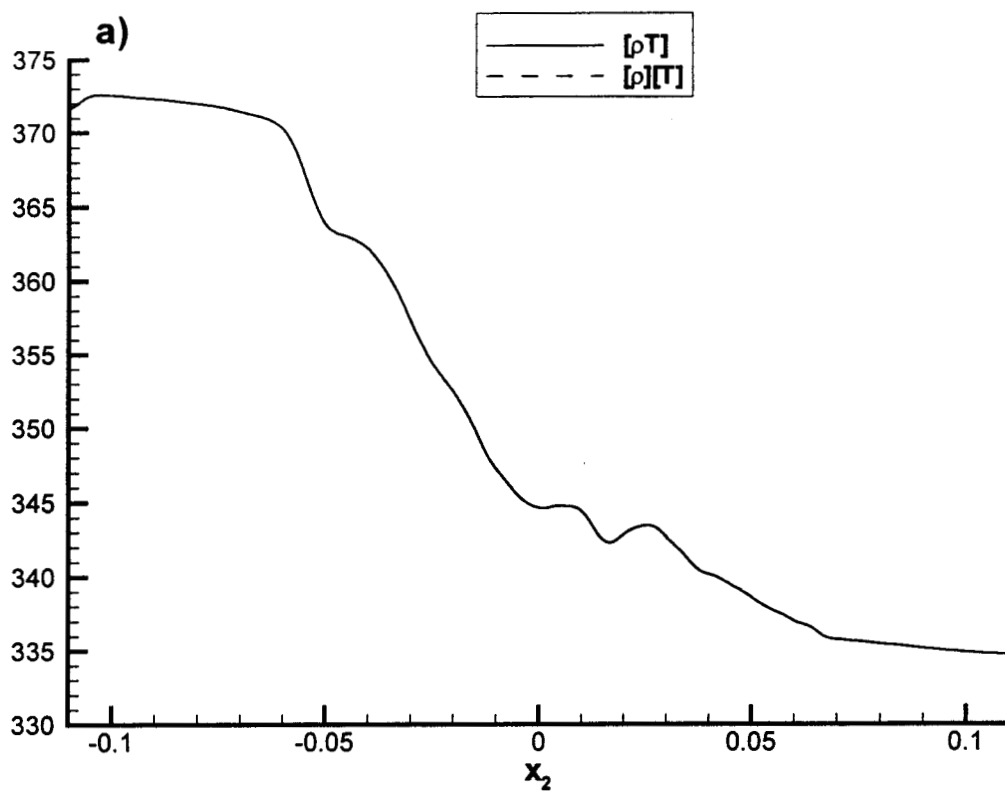


Figure 3. Evaluation of assumptions $\bar{T} = \tilde{\bar{T}}$ and $\tilde{Y}_v \bar{T} = \tilde{Y}_v \bar{T}$
a) \bar{T} b) $\tilde{Y}_v \bar{T}$ c) RMS of differences

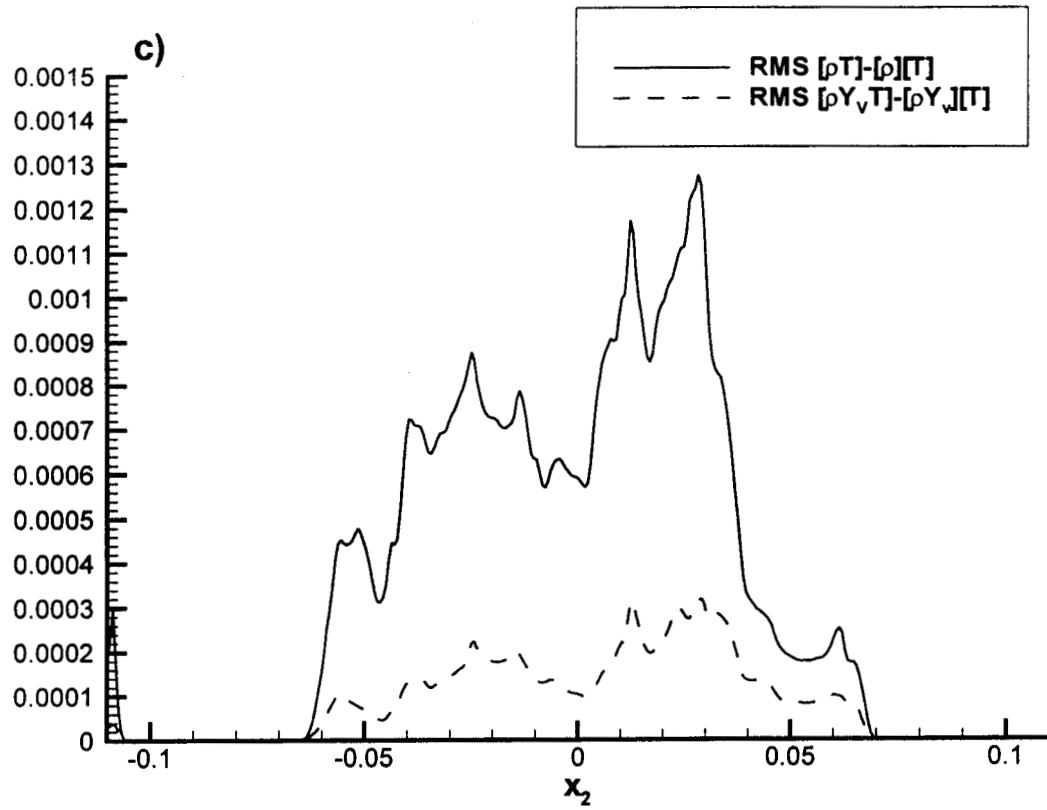


Figure 3. Evaluation of assumptions $\overline{T} = \widetilde{T}$ and $\widetilde{Y_v T} = \widetilde{Y_v} \overline{T}$
a) \overline{T} b) $\widetilde{Y_v} \overline{T}$ c) RMS of differences

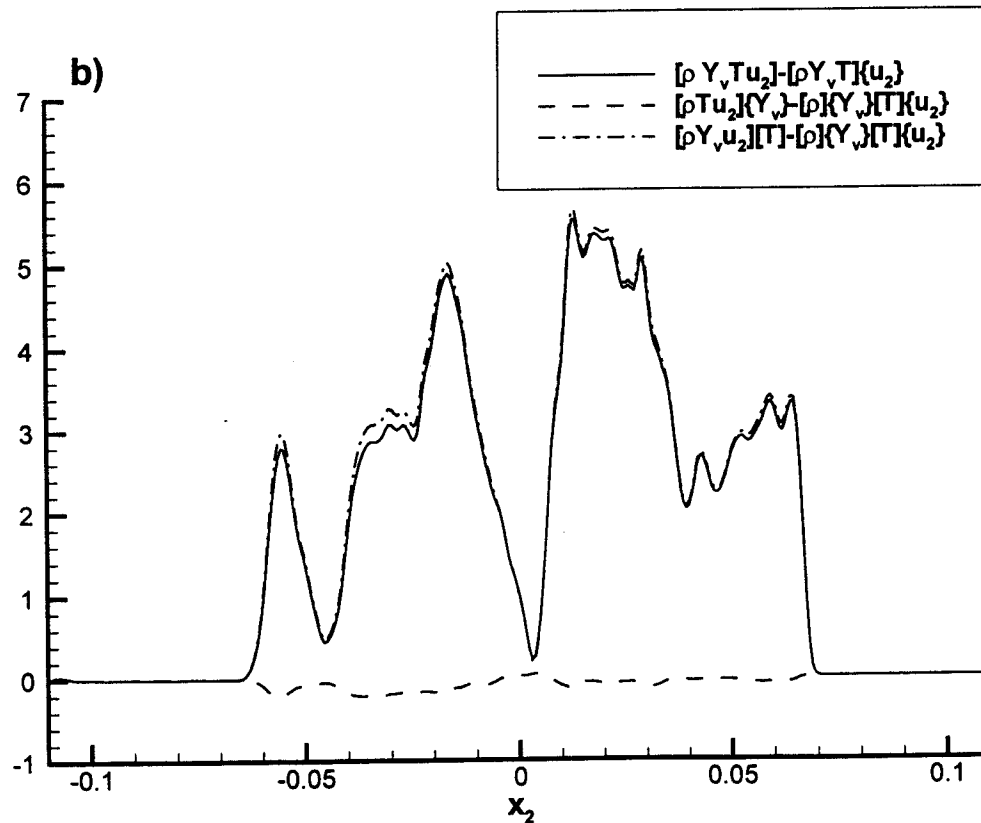
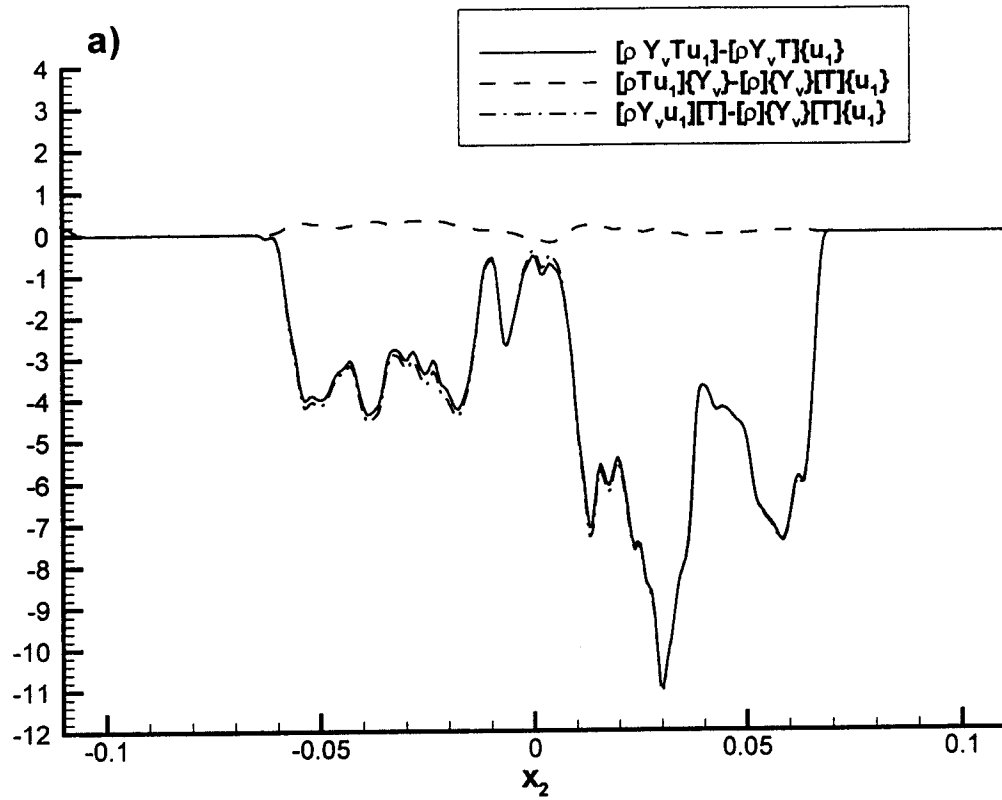


Figure 4. Evaluation of assumptions regarding $\overline{\rho Y_v T u_j} - \overline{\rho Y_v T} \tilde{u}_j$
a) $j=1$ b) $j=2$ c) $j=3$

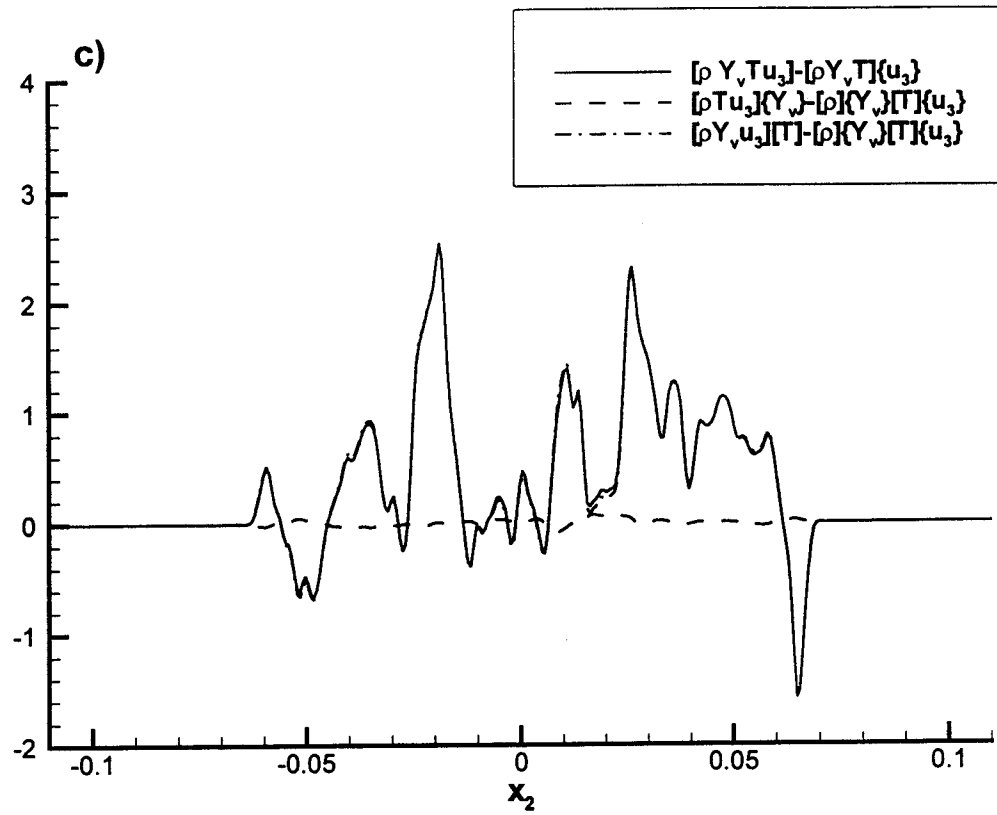


Figure 4. Evaluation of assumptions regarding $\overline{\rho Y_v T u_j} - \overline{\rho Y_v T} \tilde{u}_j$
a) $j=1$ b) $j=2$ c) $j=3$

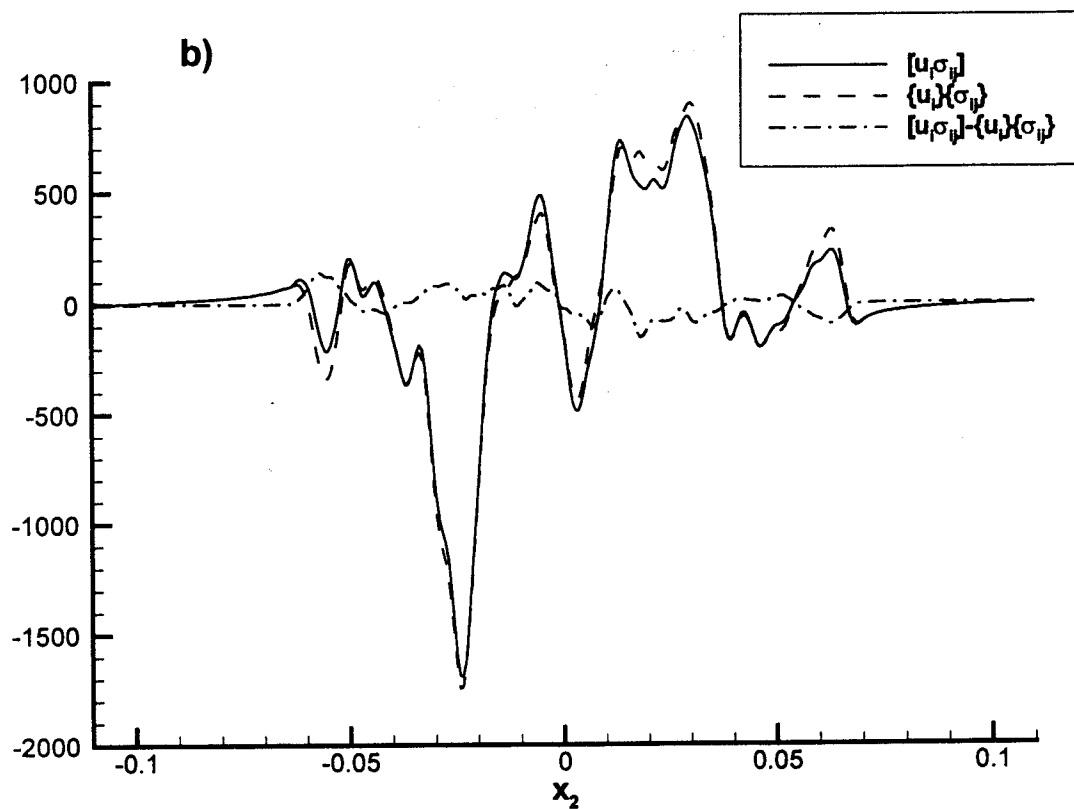
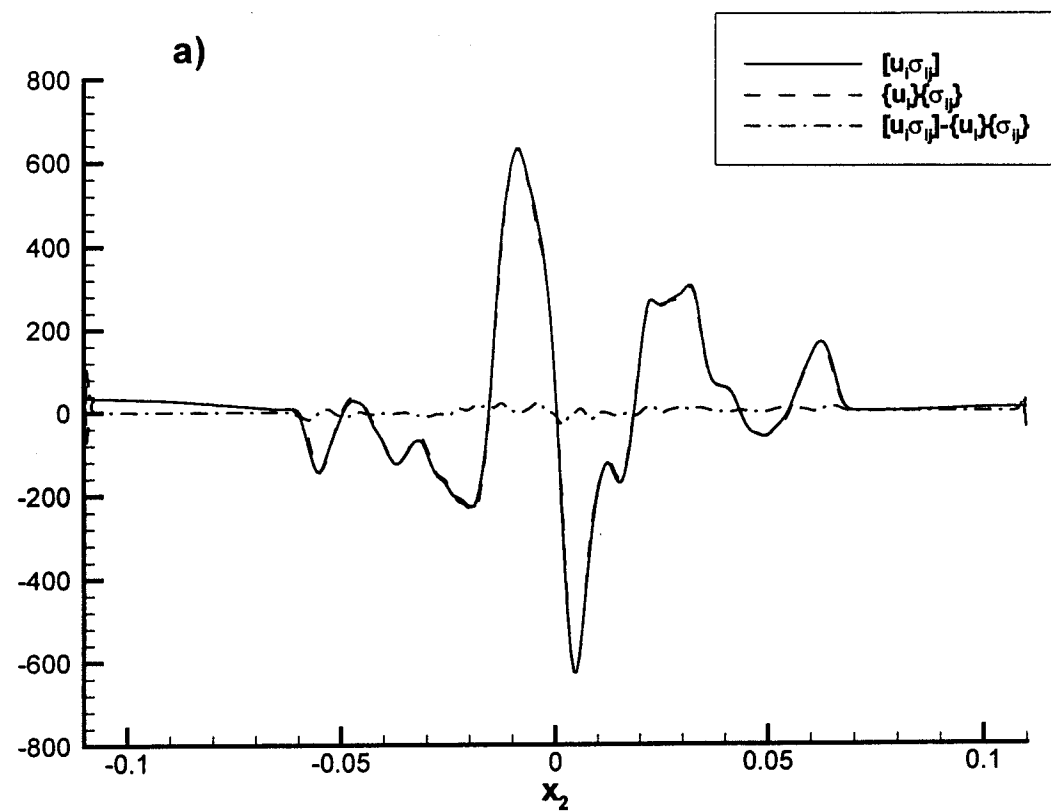


Figure 5. Evaluation of assumption $\overline{u_i \sigma_{ij}} = \tilde{u}_i \tilde{\sigma}_{ij}$
a) $j=1$ b) $j=2$ c) $j=3$

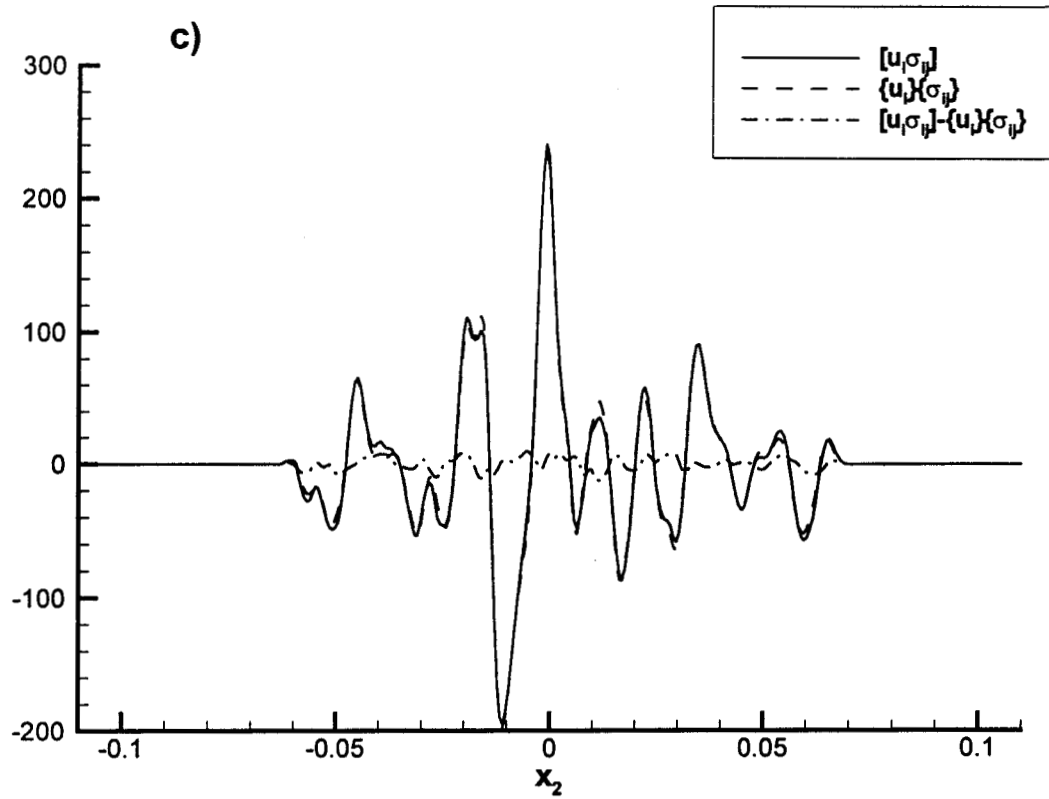


Figure 5. Evaluation of assumption $\overline{u_i \sigma_{ij}} = \tilde{u}_i \tilde{\sigma}_{ij}$
a) $j=1$ b) $j=2$ c) $j=3$

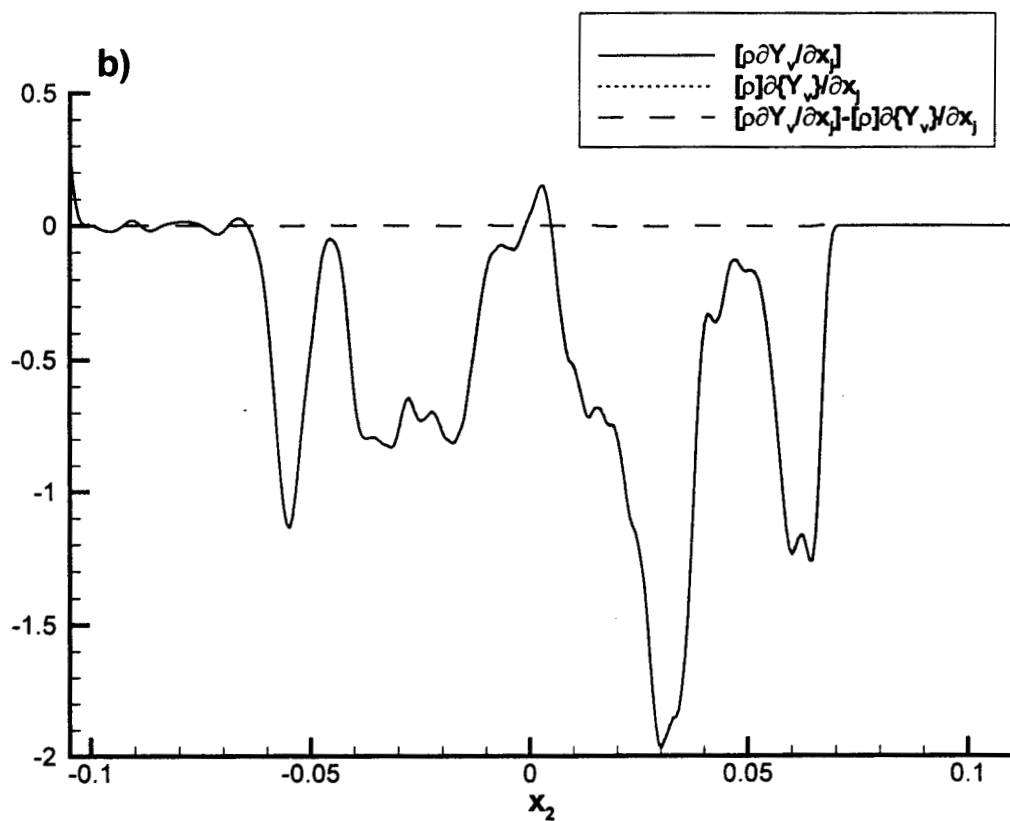
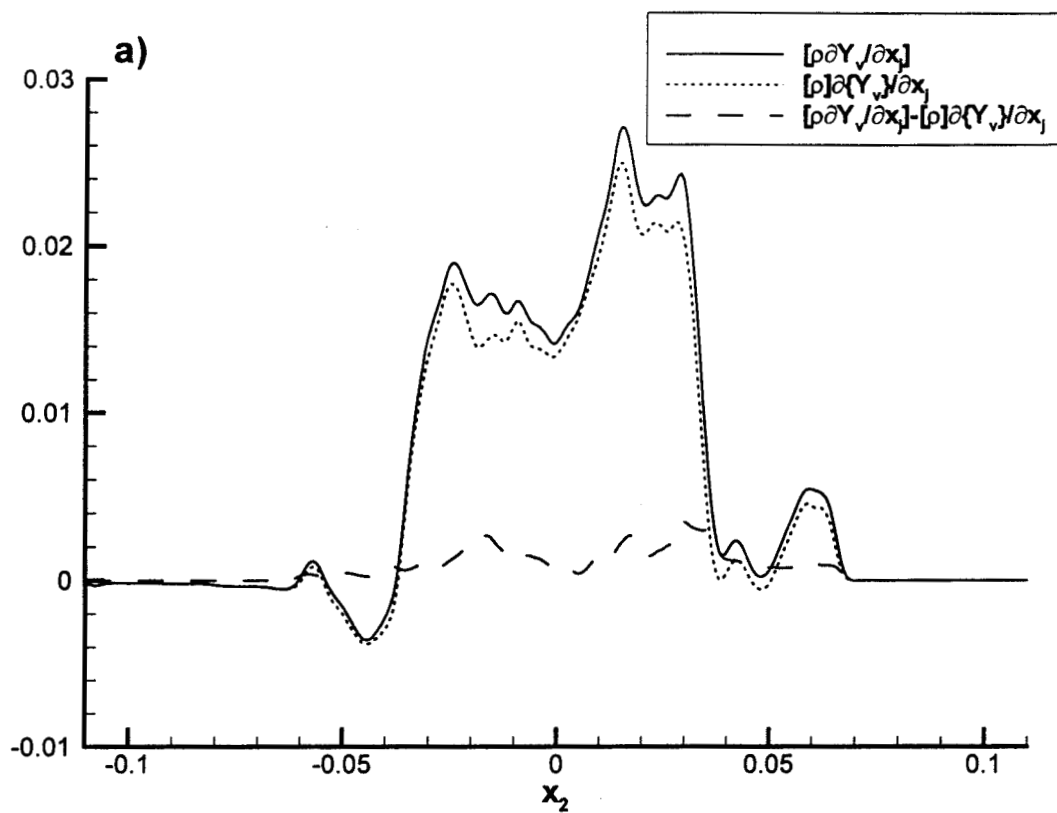


Figure 6. Evaluation of assumption $\overline{\rho \partial Y / \partial x_j} = \bar{\rho} \partial \tilde{Y} / \partial x_j$
a) $j=1$ b) $j=2$ c) $j=3$

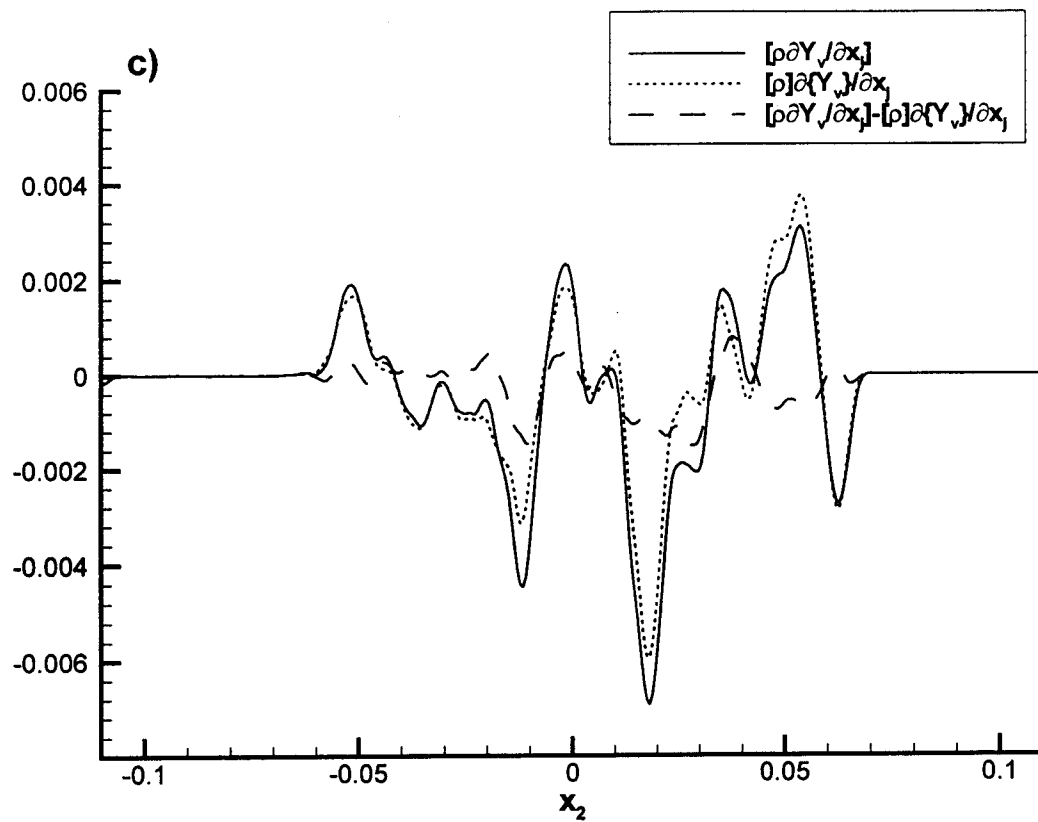


Figure 6. Evaluation of assumption $\overline{\rho \partial Y / \partial x_j} = \bar{\rho} \partial \tilde{Y} / \partial x_j$
a) $j=1$ b) $j=2$ c) $j=3$

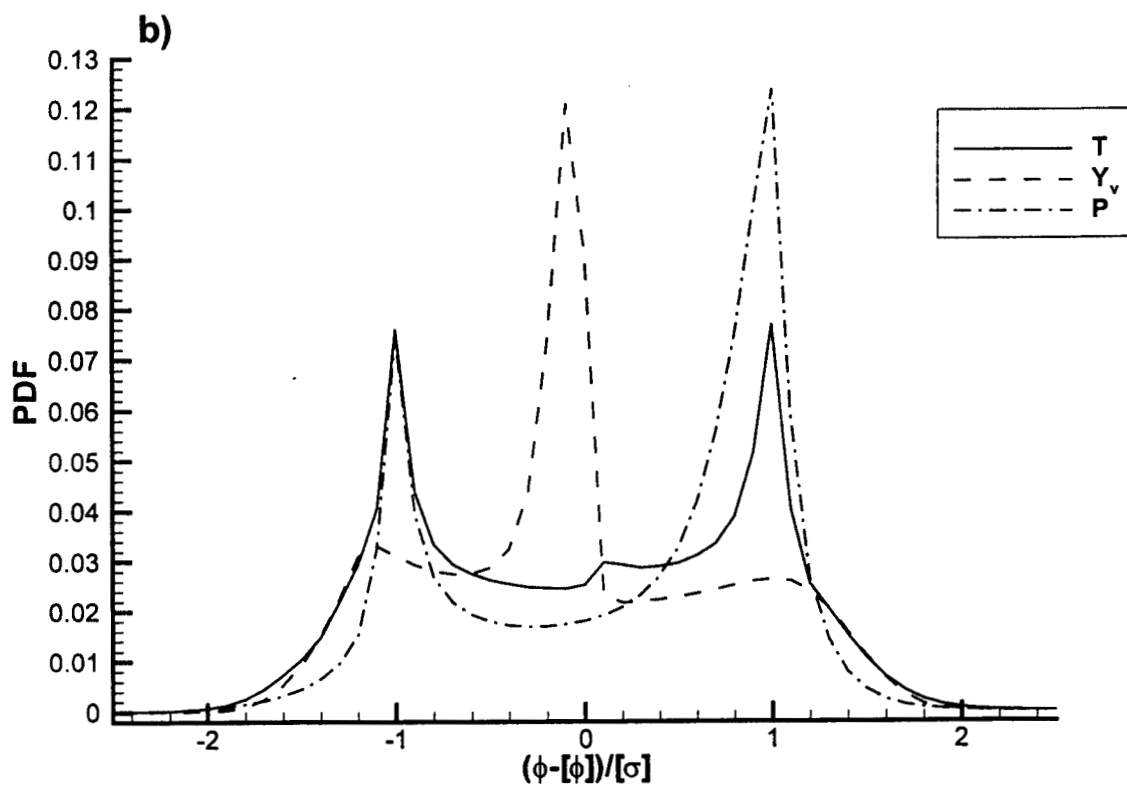
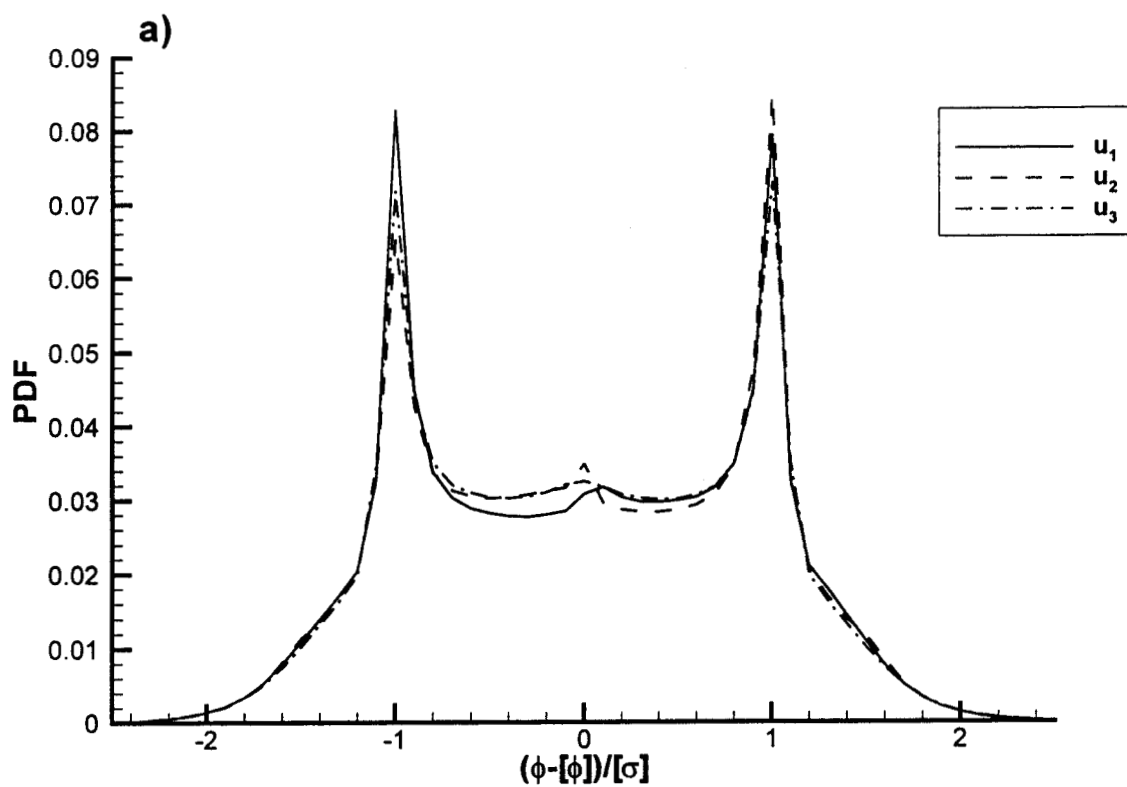


Figure 7. PDF of $(\phi - [\phi]) / \bar{\sigma}$ a) u_1, u_2, u_3 b) T, Y_v, P

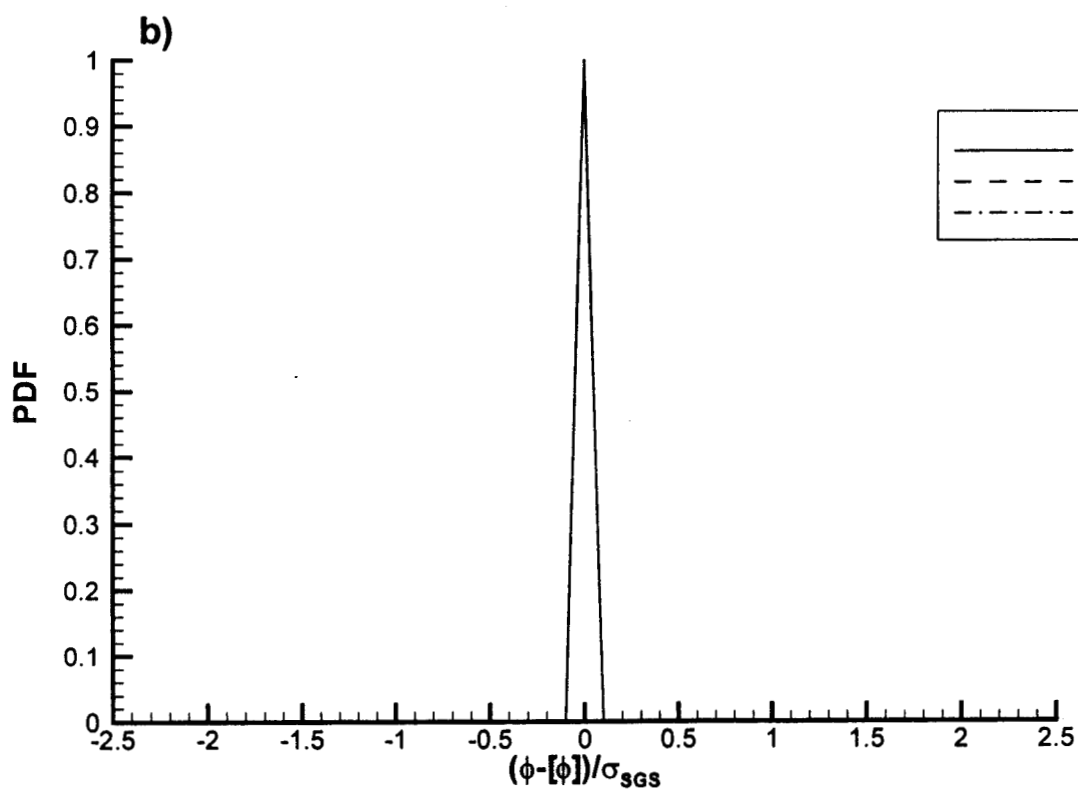
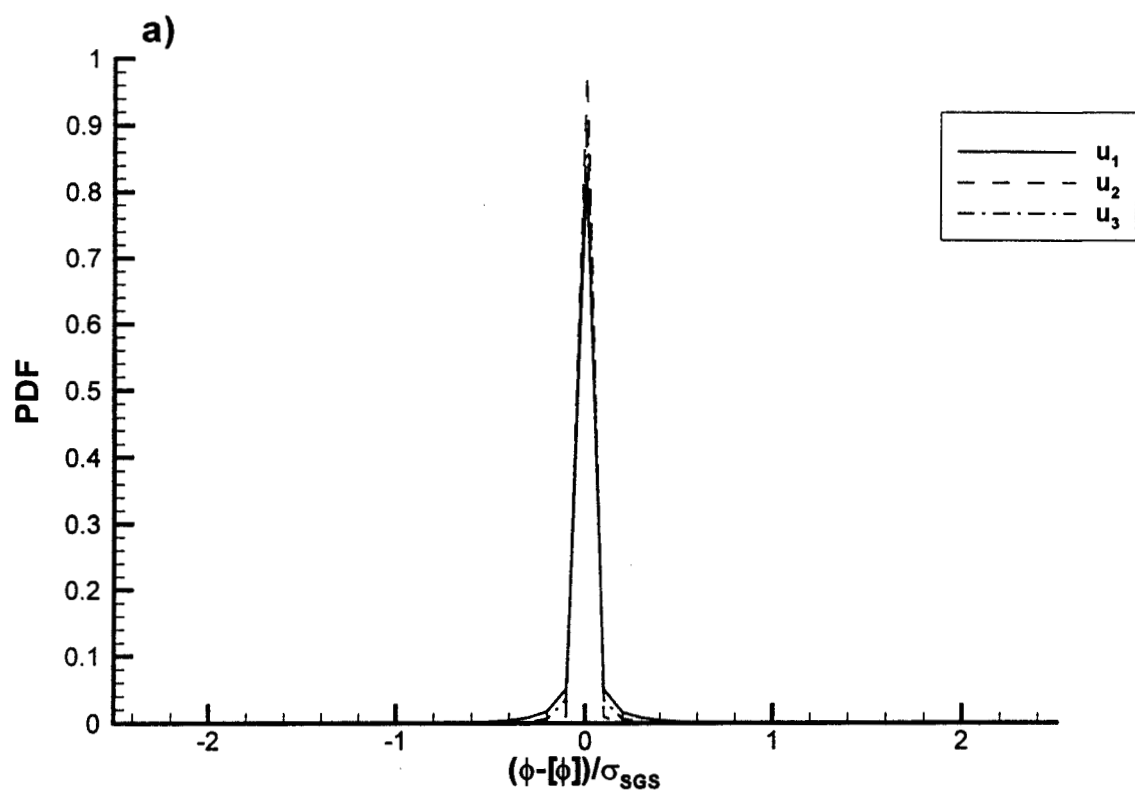


Figure 8 . PDF of $(\phi - \bar{\phi}) / \sigma_{SGS}$ a) u_1, u_2, u_3 b) T, Y_v, P

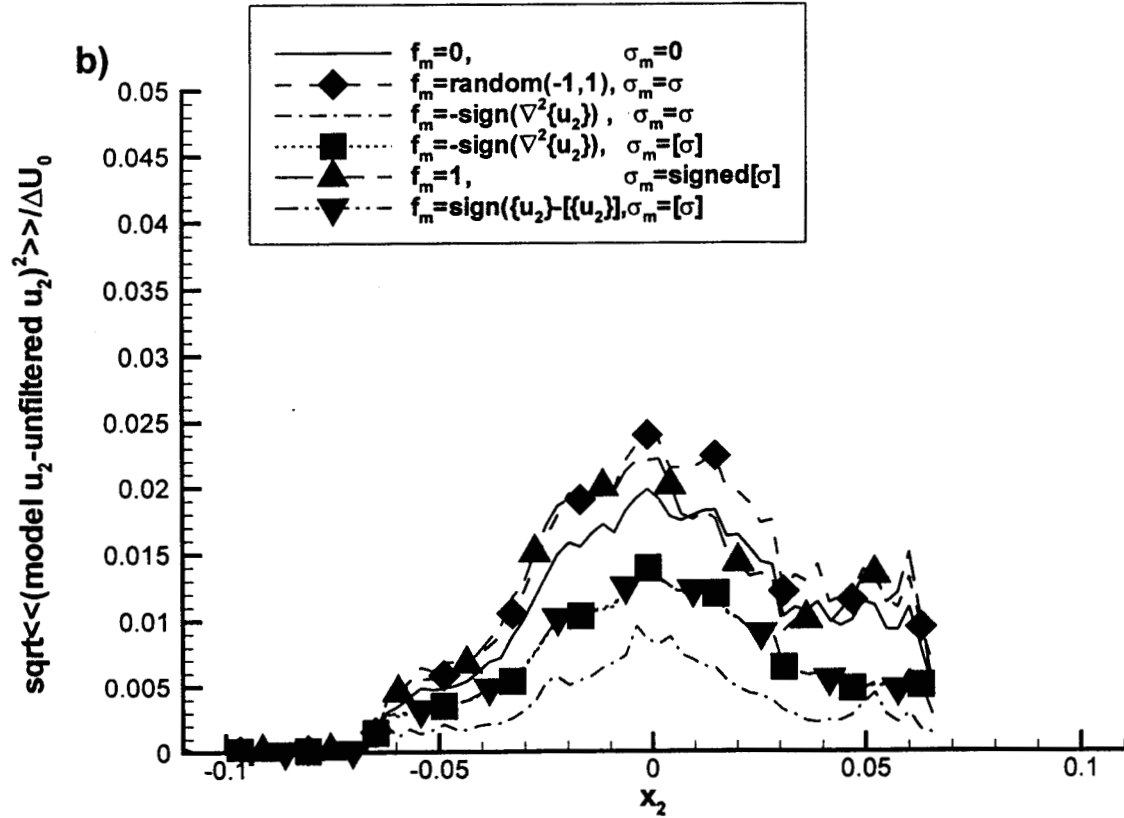
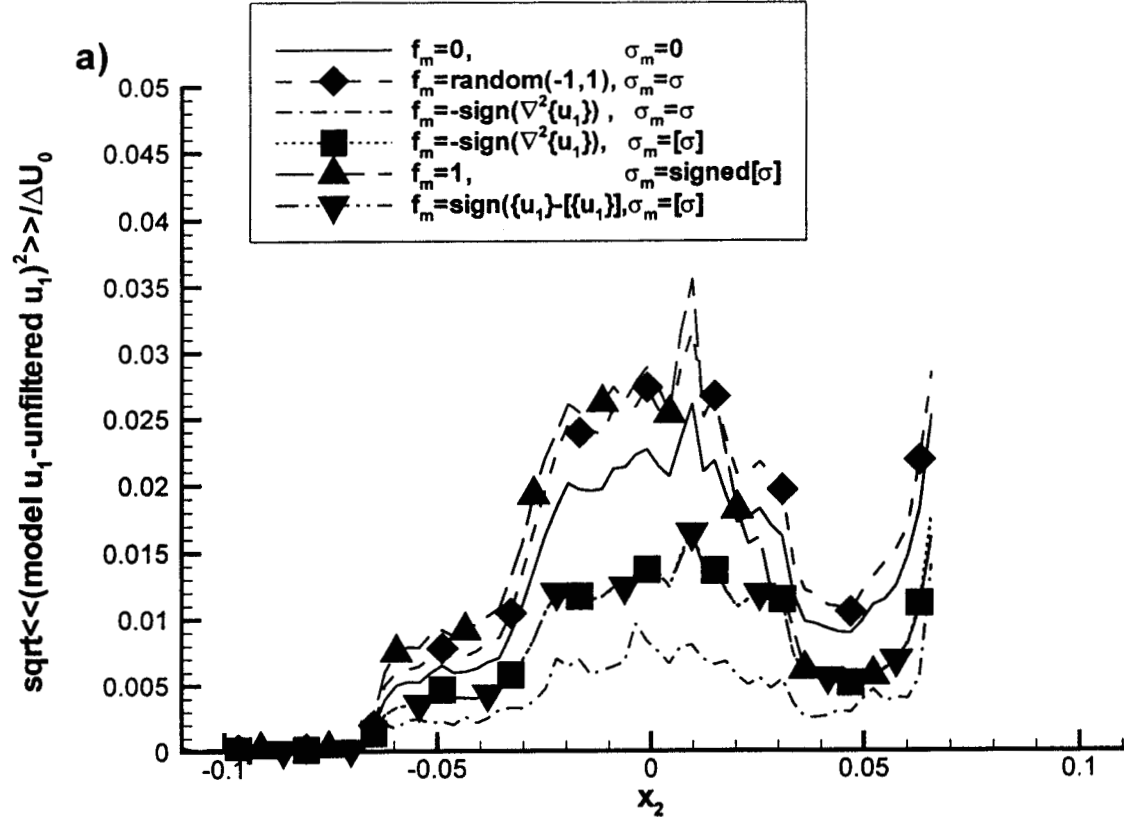


Figure 9. Error in unfiltered variable model $\phi = \bar{\phi} + f_m \sigma_m$ interpolated to droplet locations, Case TP600 a) u_1 b) u_2 c) u_3 d) T e) Y_v f) P

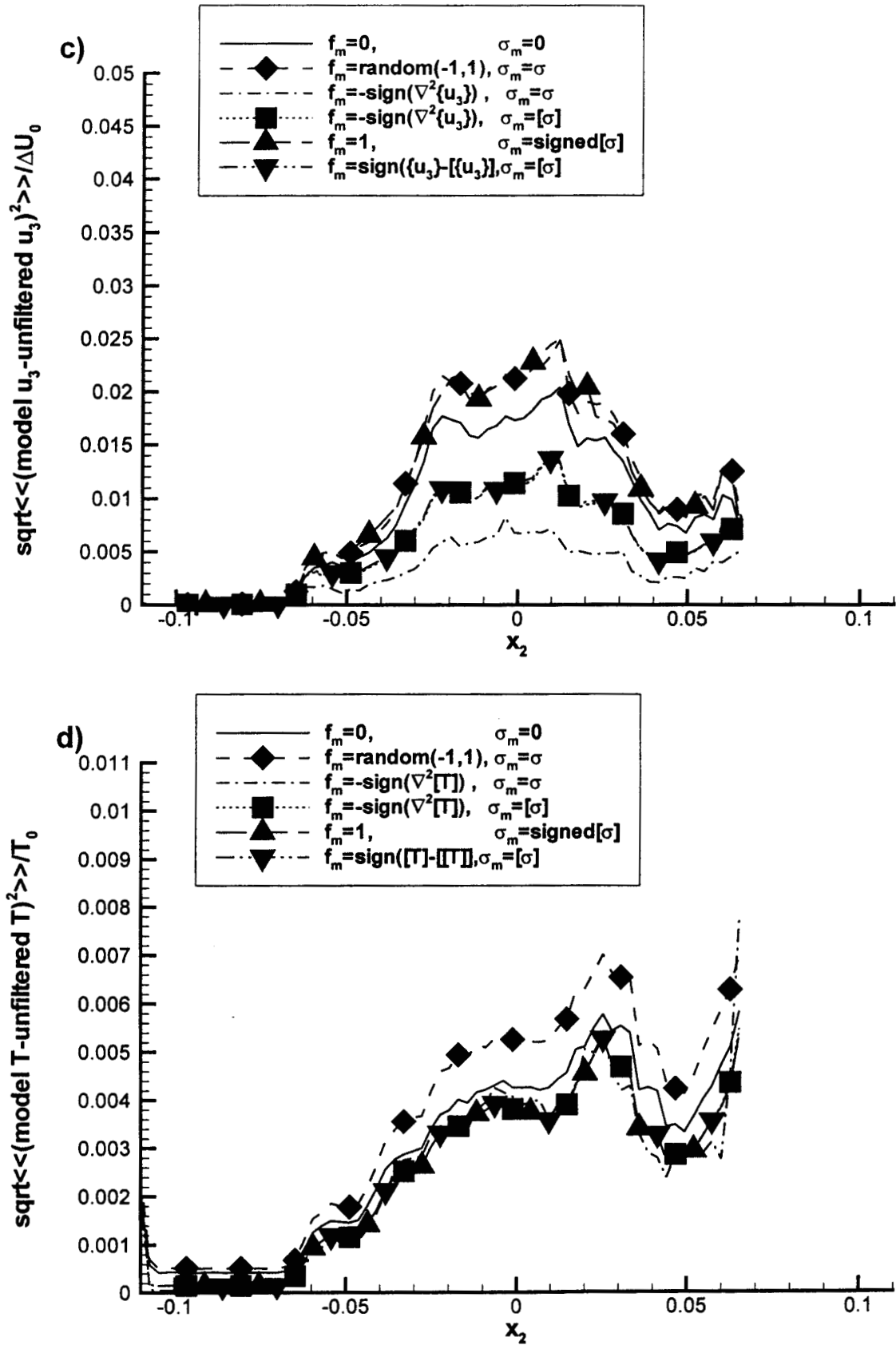


Figure 9. Error in unfiltered variable model $\phi = \bar{\phi} + f_m \sigma$ interpolated to droplet locations, Case TP600 a) u_1 b) u_2 c) u_3 d) T e) Y_v f) P

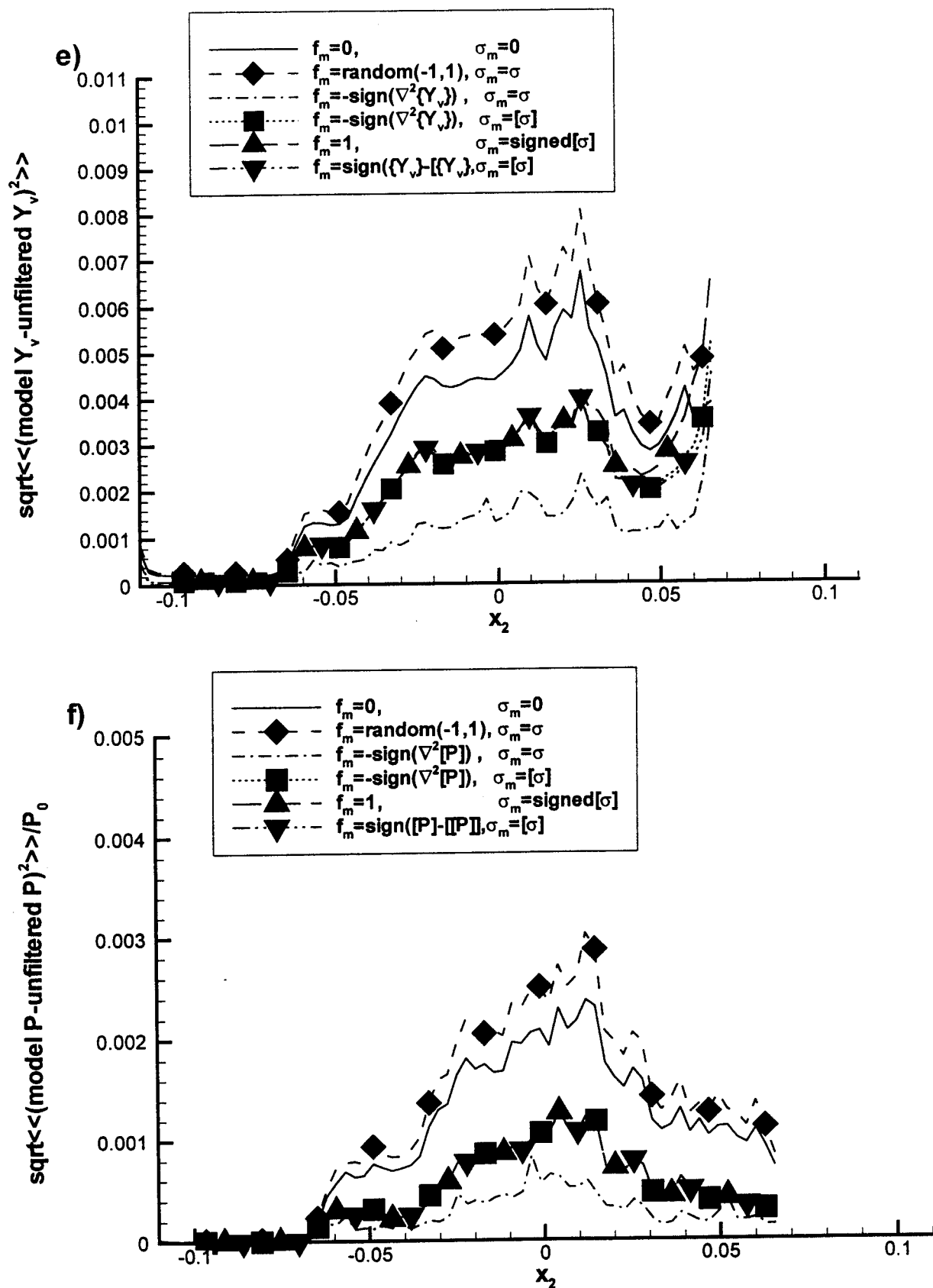


Figure 9. Error in unfiltered variable model $\phi = \bar{\phi} + f_m \sigma_m$ interpolated to droplet locations, Case TP600 a) u_1 b) u_2 c) u_3 d) T e) Y_v f) P

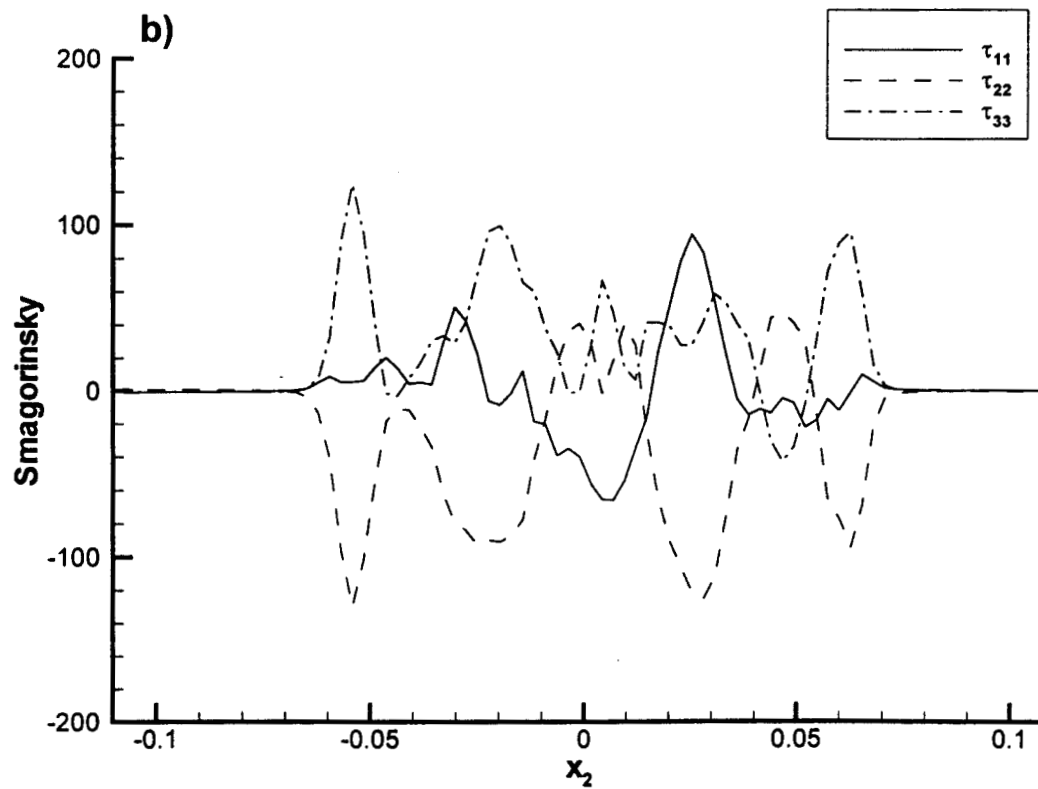
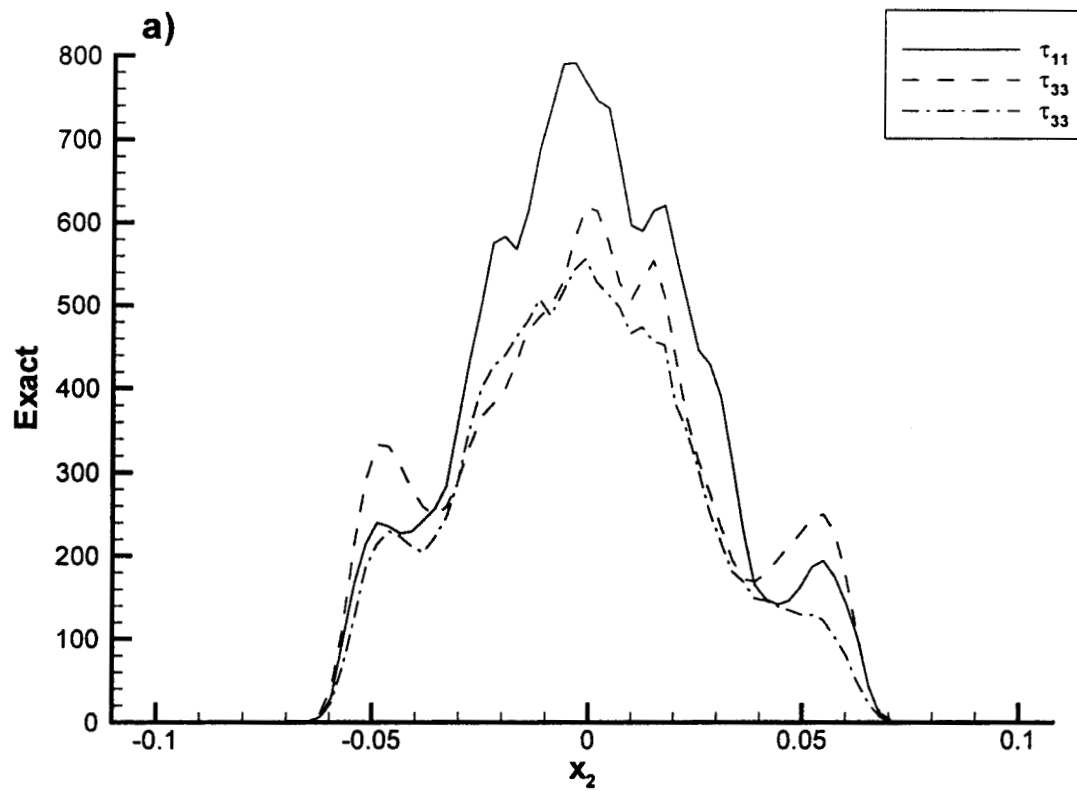


Figure 10. Subgrid stresses, Case TP600 a) Exact b) Smagorinsky c) Correlation between exact and Smagorinsky stresses

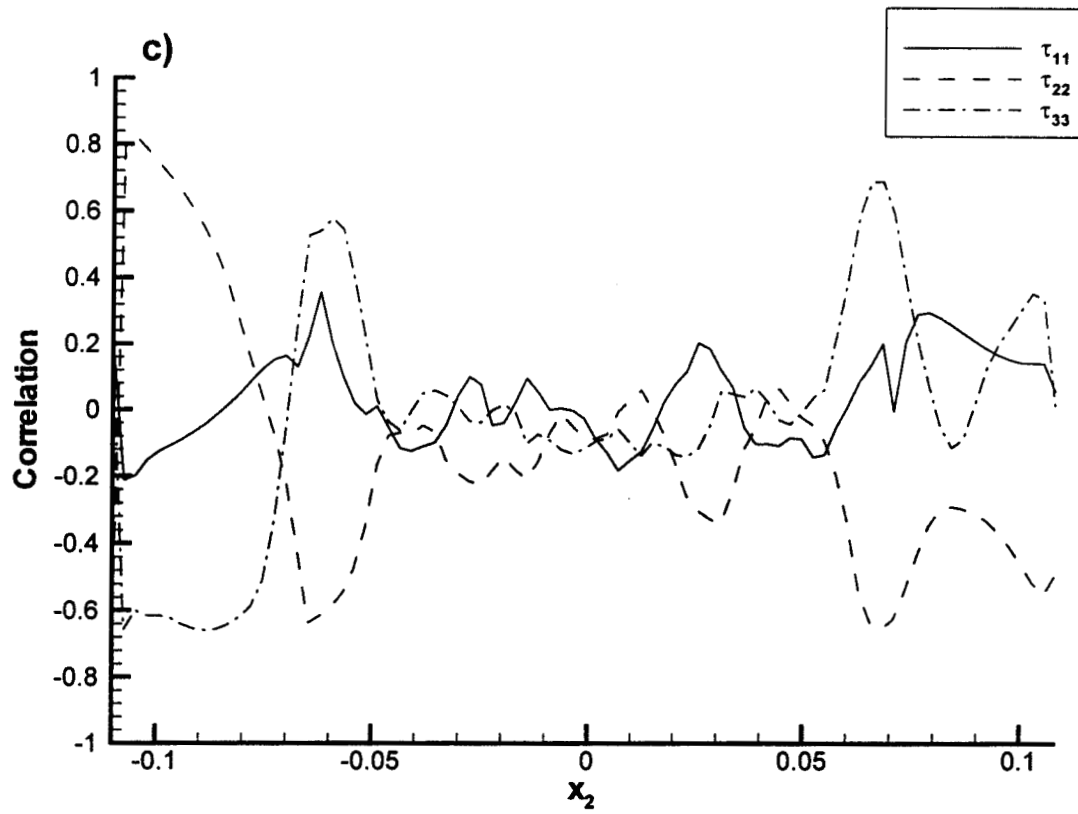


Figure 10. Subgrid stresses, Case TP600 a) Exact b) Smagorinsky c) Correlation between exact and Smagorinsky stresses

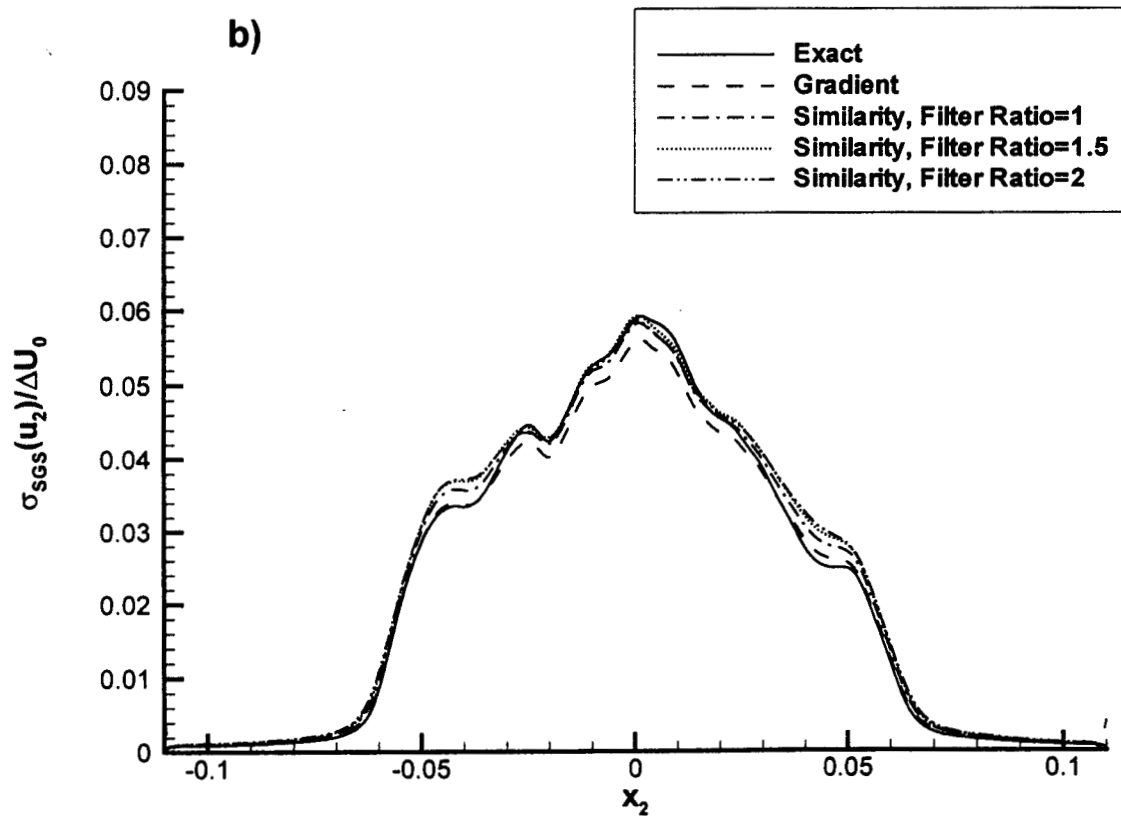
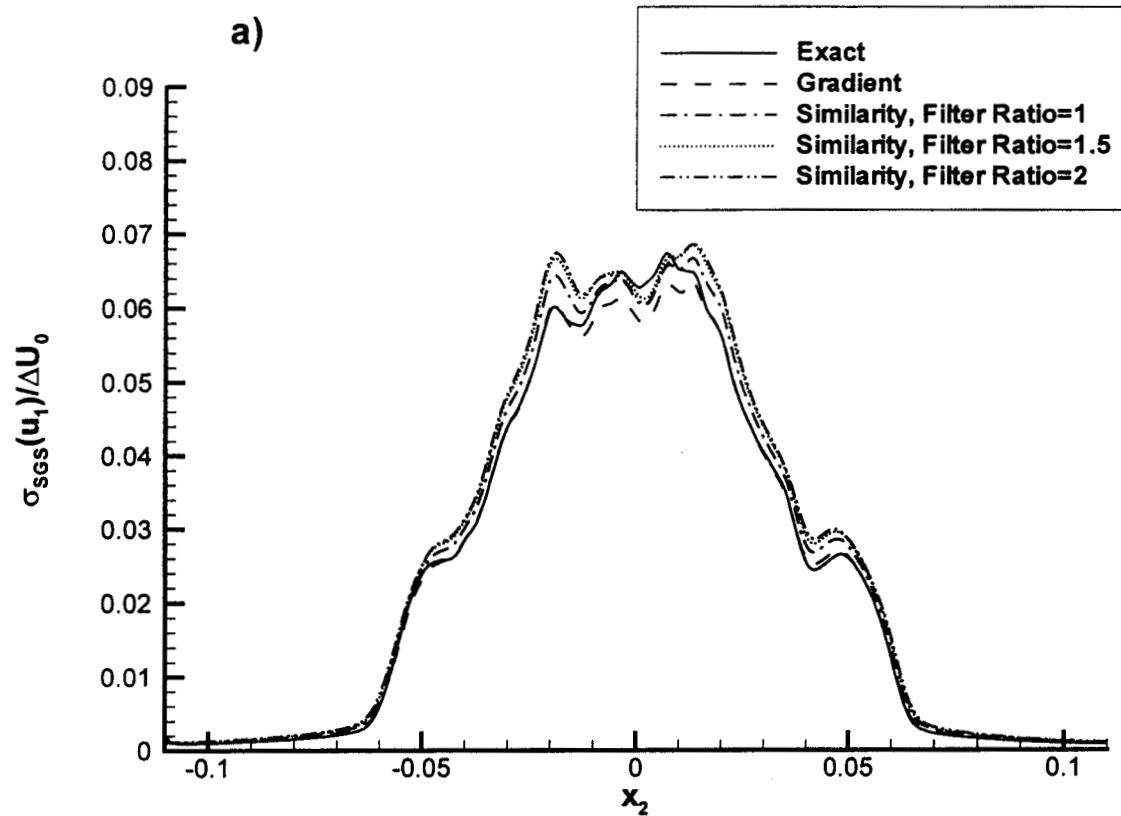


Figure 11. SGS standard deviation, Case TP500a
a) u_1 b) u_2 c) u_3 d) T e) Y_v f) P

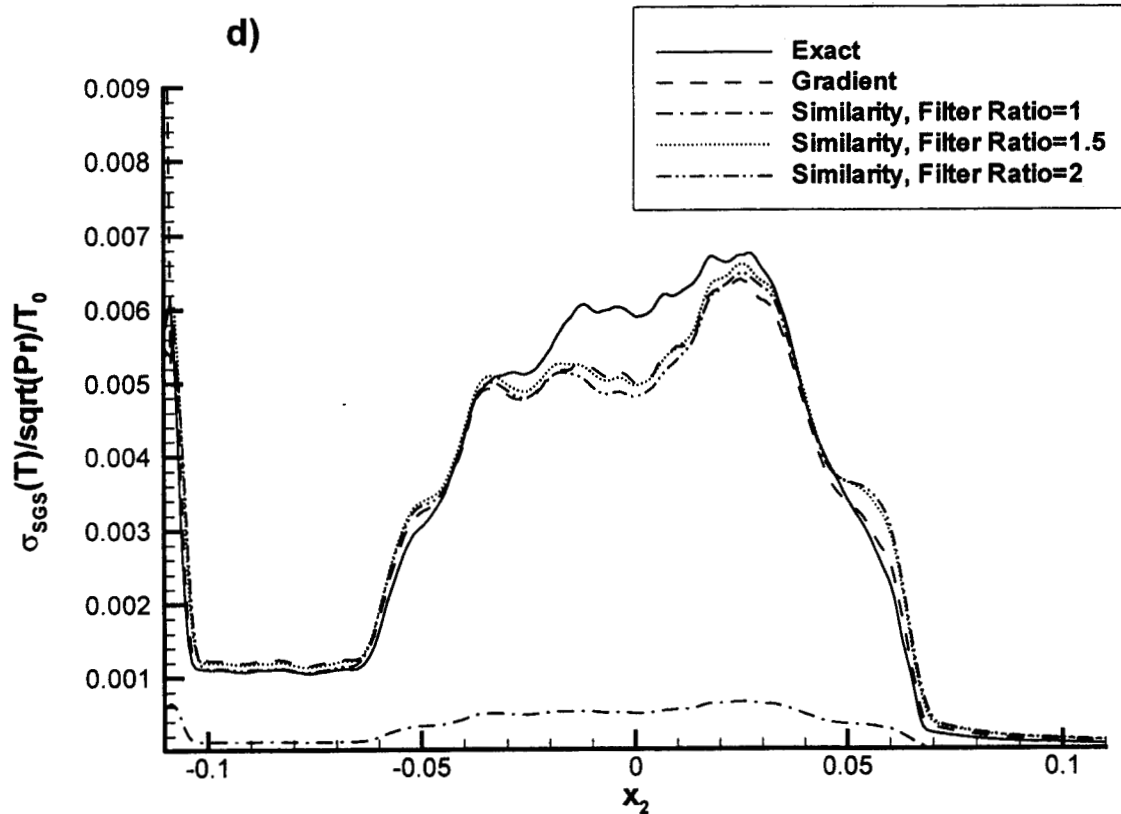
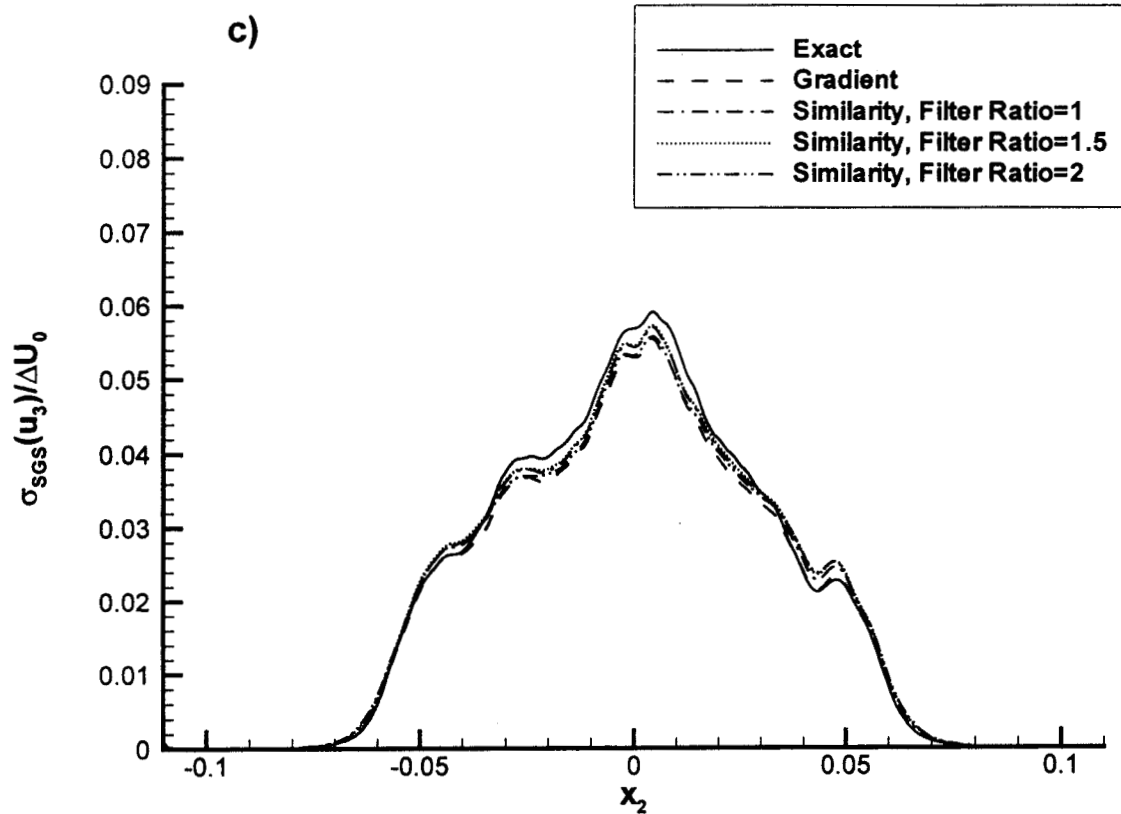


Figure 11. SGS standard deviation, Case TP500a
a) u_1 b) u_2 c) u_3 d) T e) Y_v f) P

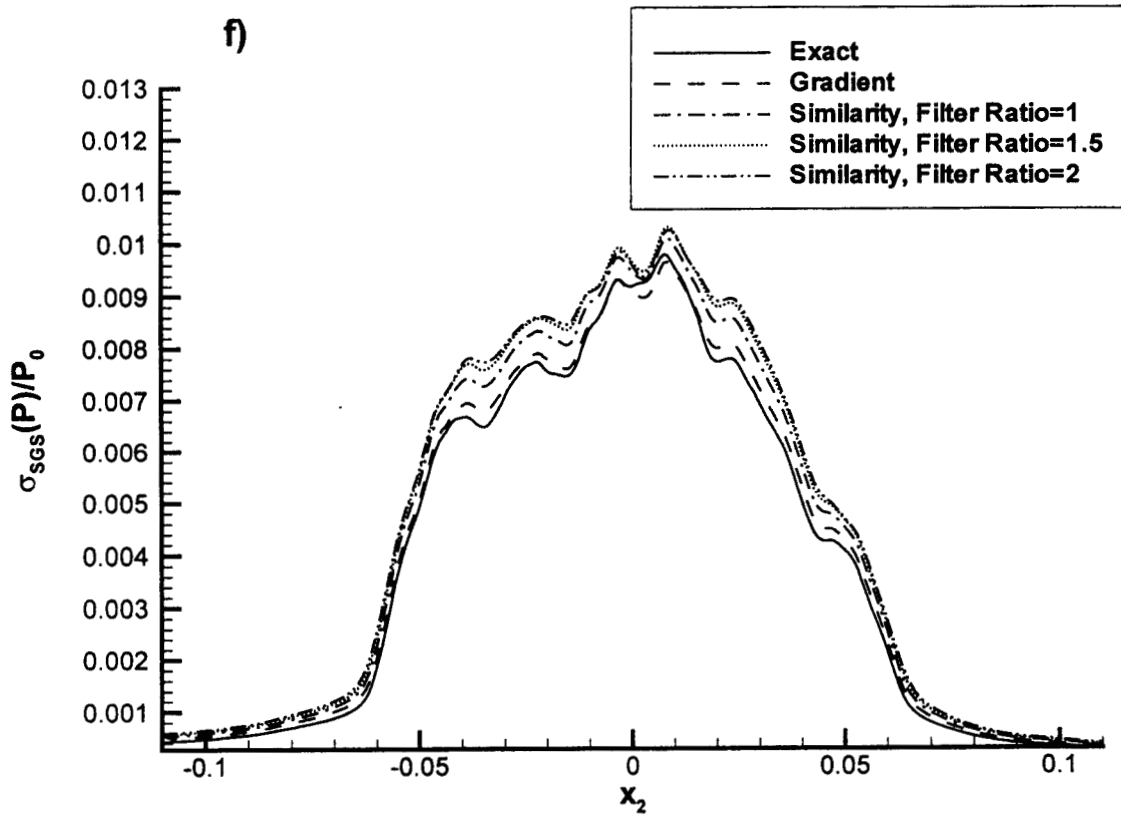
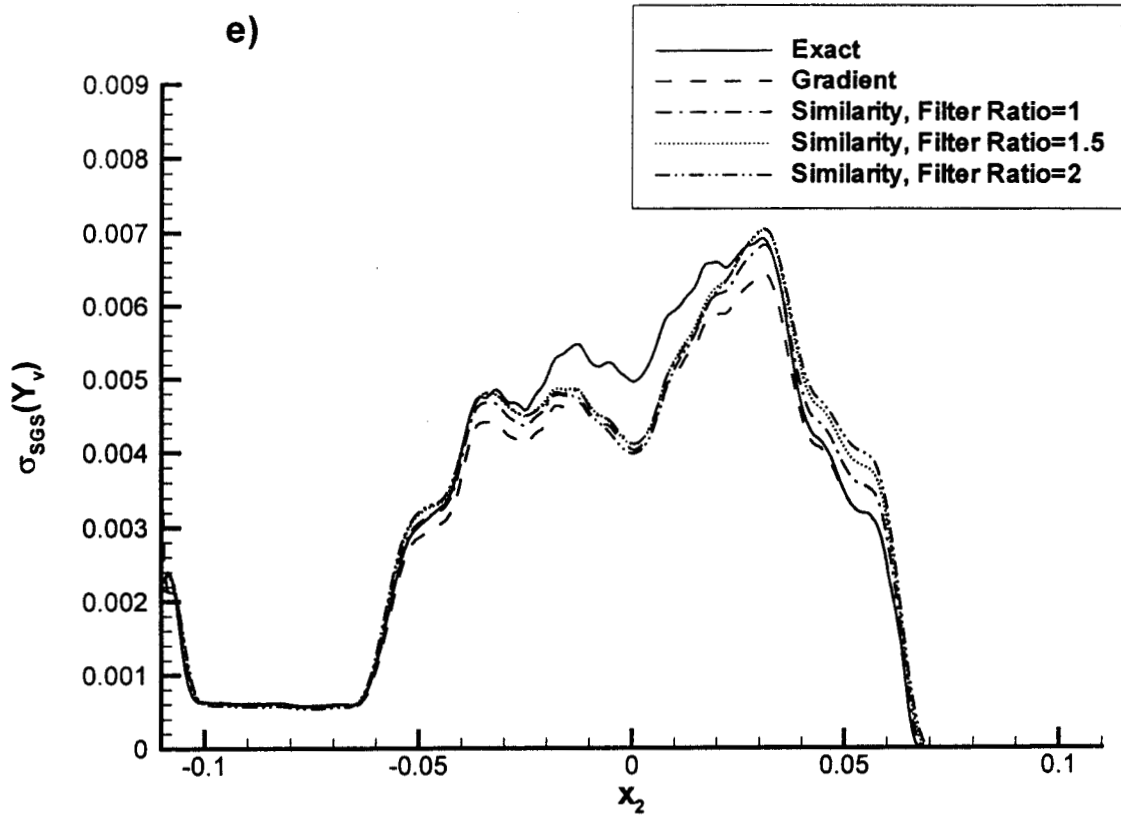


Figure 11. SGS standard deviation, Case TP500a
a) u_1 b) u_2 c) u_3 d) T e) Y_v f) P

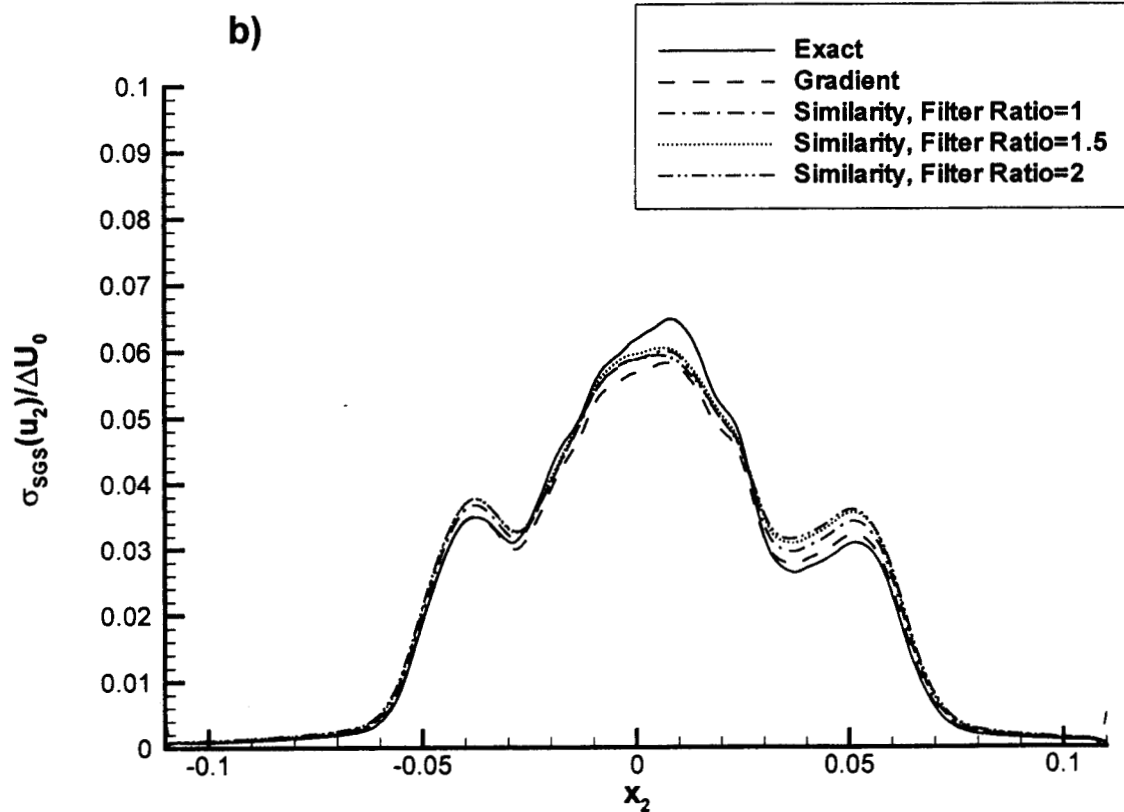
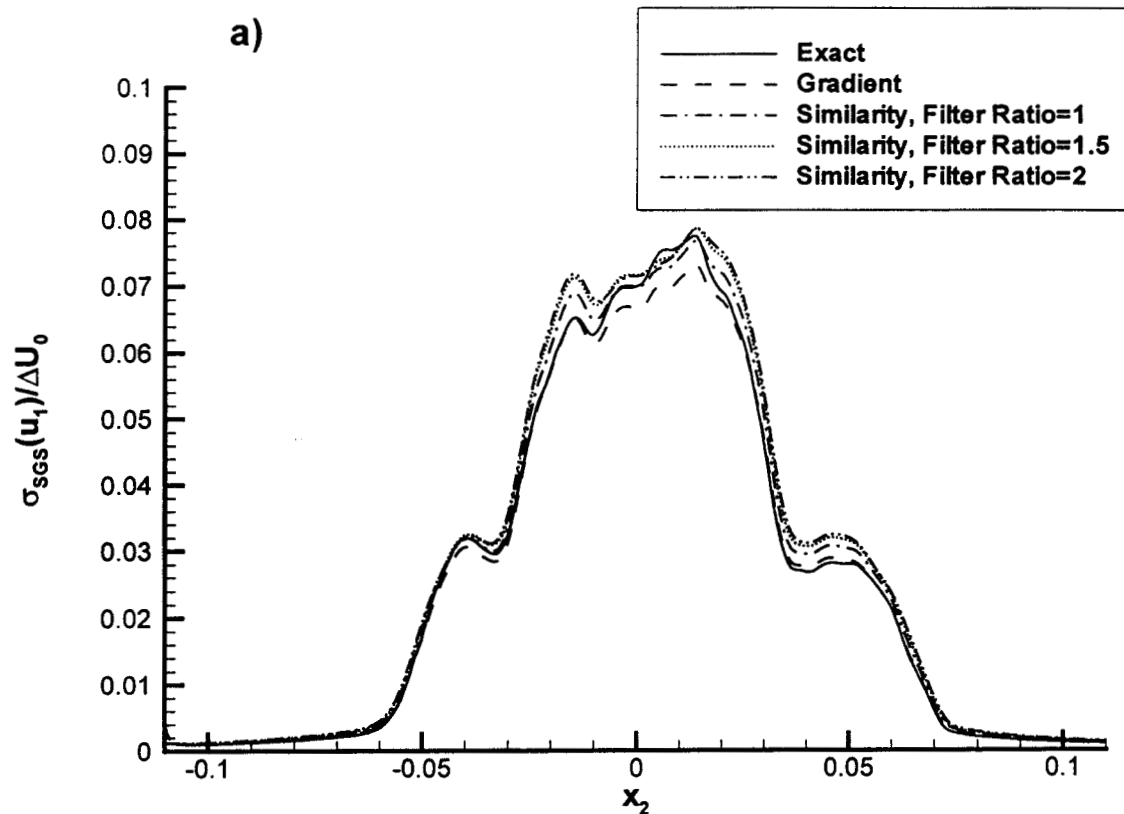


Figure 12. SGS standard deviation, Case TP500b
a) u_1 b) u_2 c) u_3 d) T e) Y_v f) P

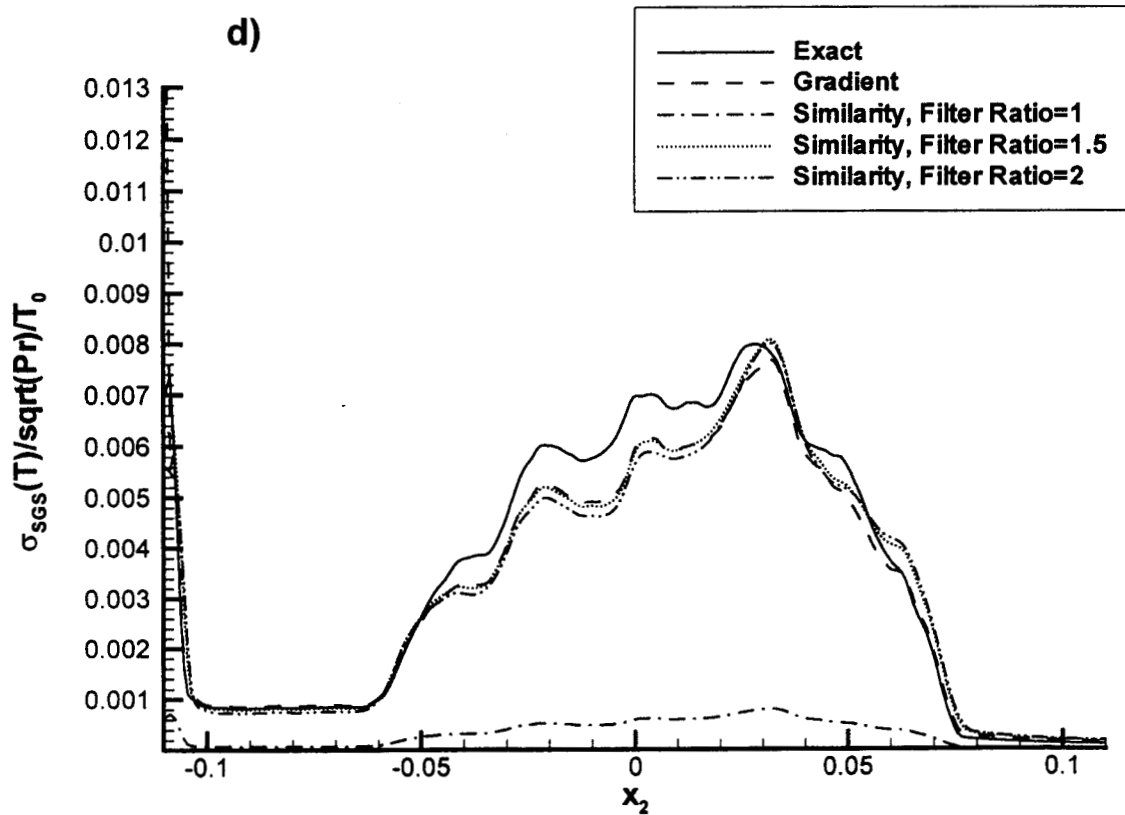
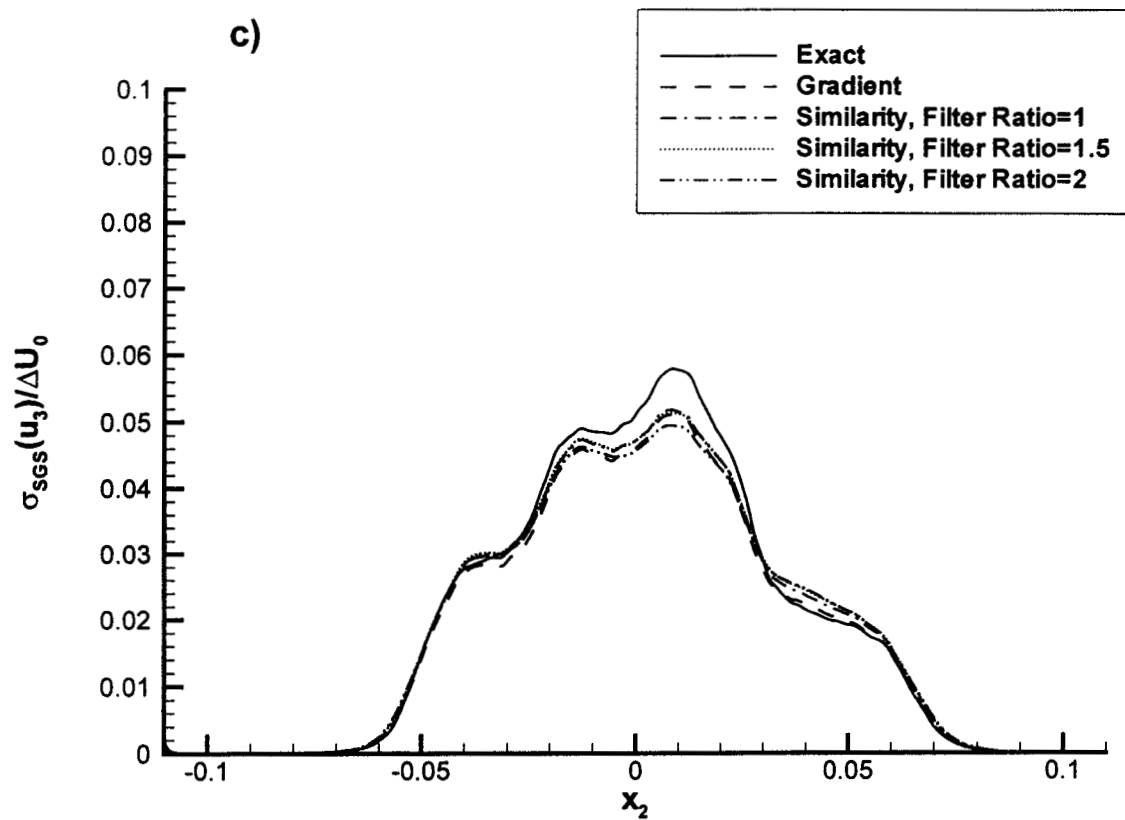


Figure 12. SGS standard deviation, Case TP500b
a) u_1 b) u_2 c) u_3 d) T e) Y_v f) P

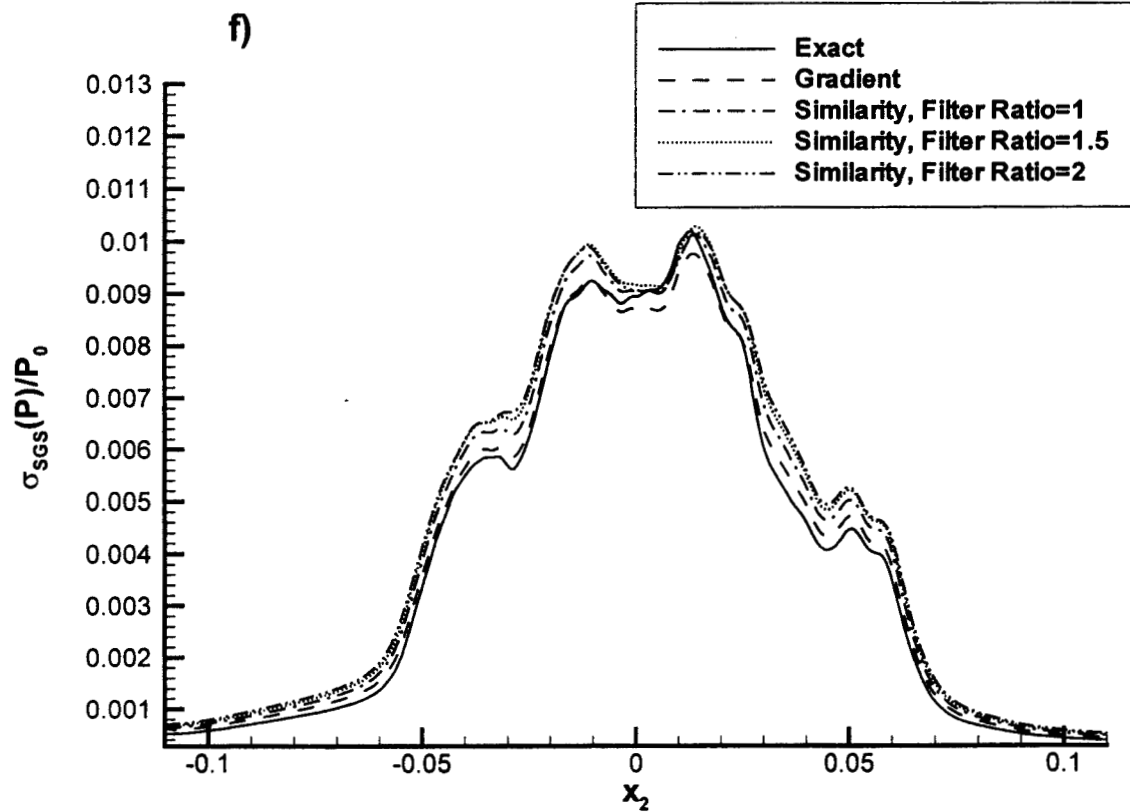
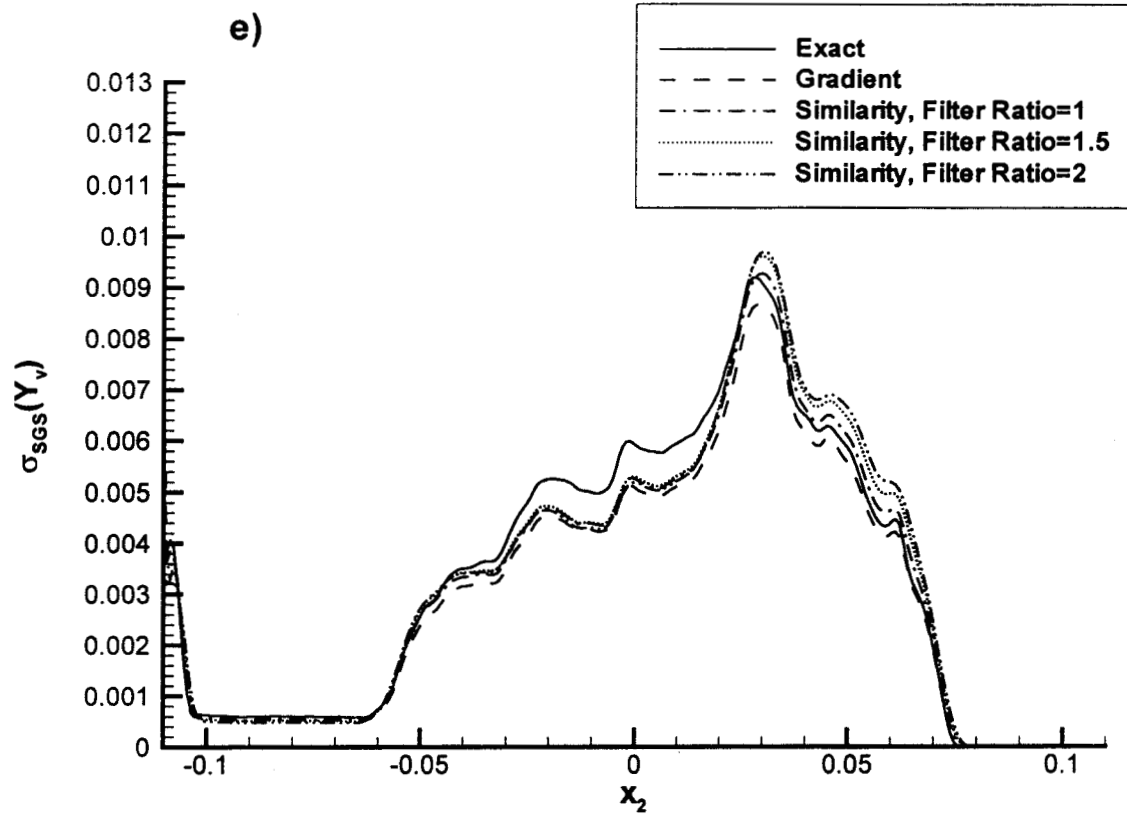


Figure 12. SGS standard deviation, Case TP500b
a) u_1 b) u_2 c) u_3 d) T e) Y_v f) P

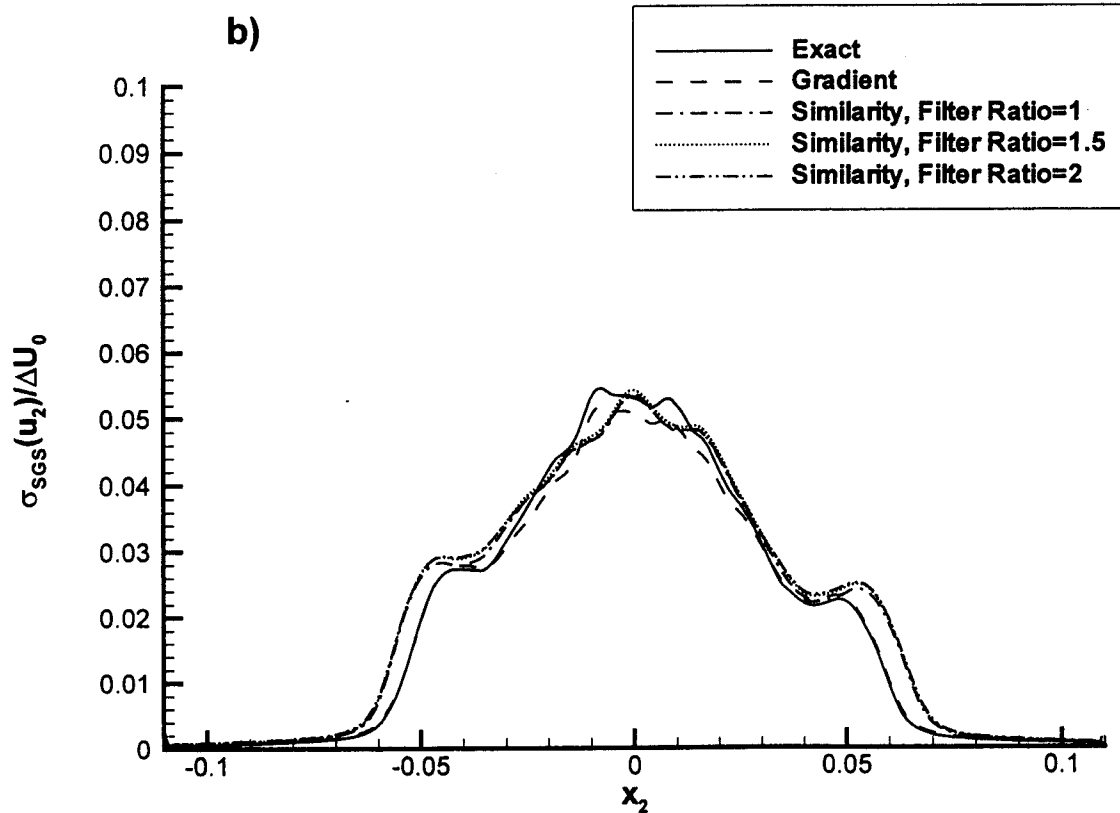
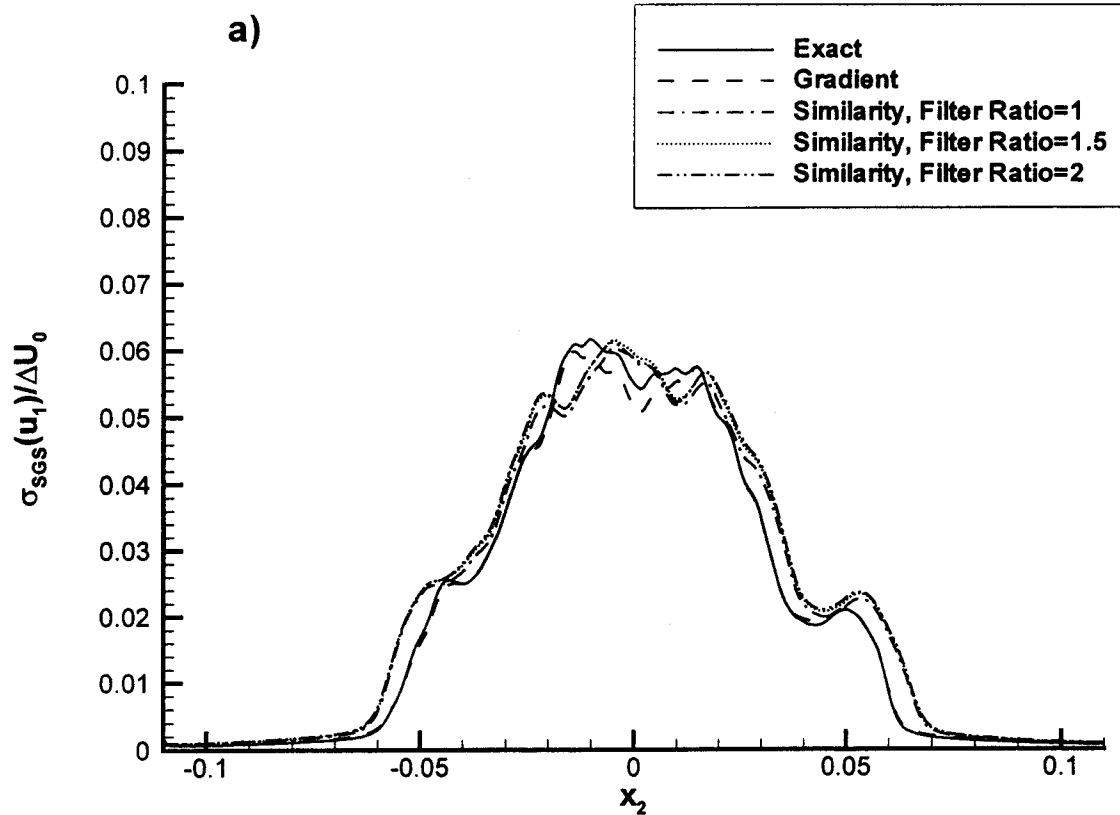


Figure 13. SGS standard deviation, Case TP600
a) u_1 b) u_2 c) u_3 d) T e) Y_v f) P

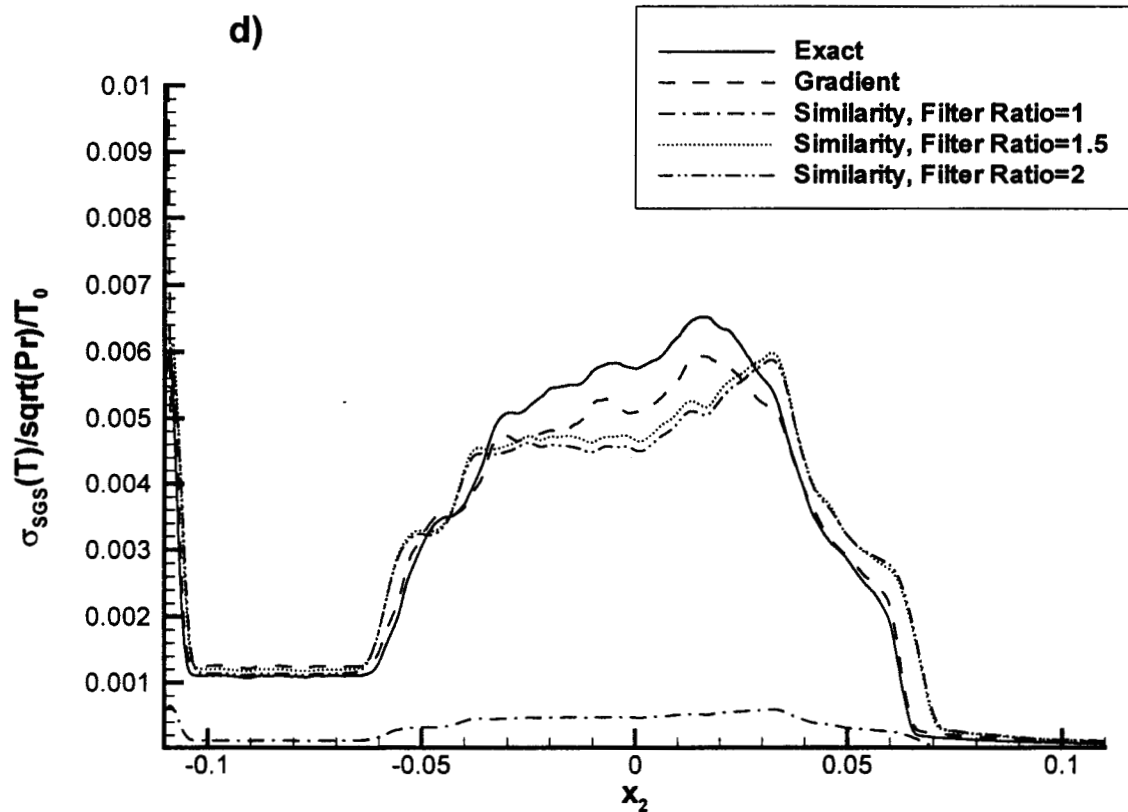
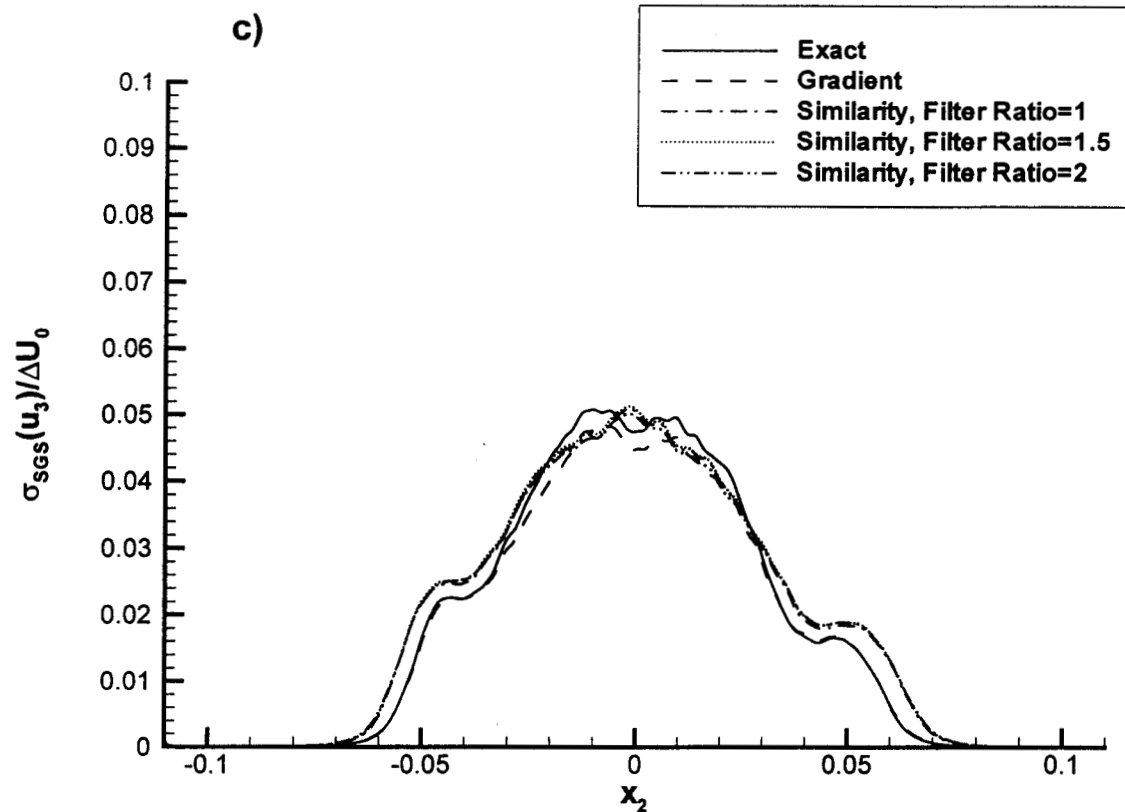


Figure 13. SGS standard deviation, Case TP600
a) u_1 b) u_2 c) u_3 d) T e) Y_v f) P

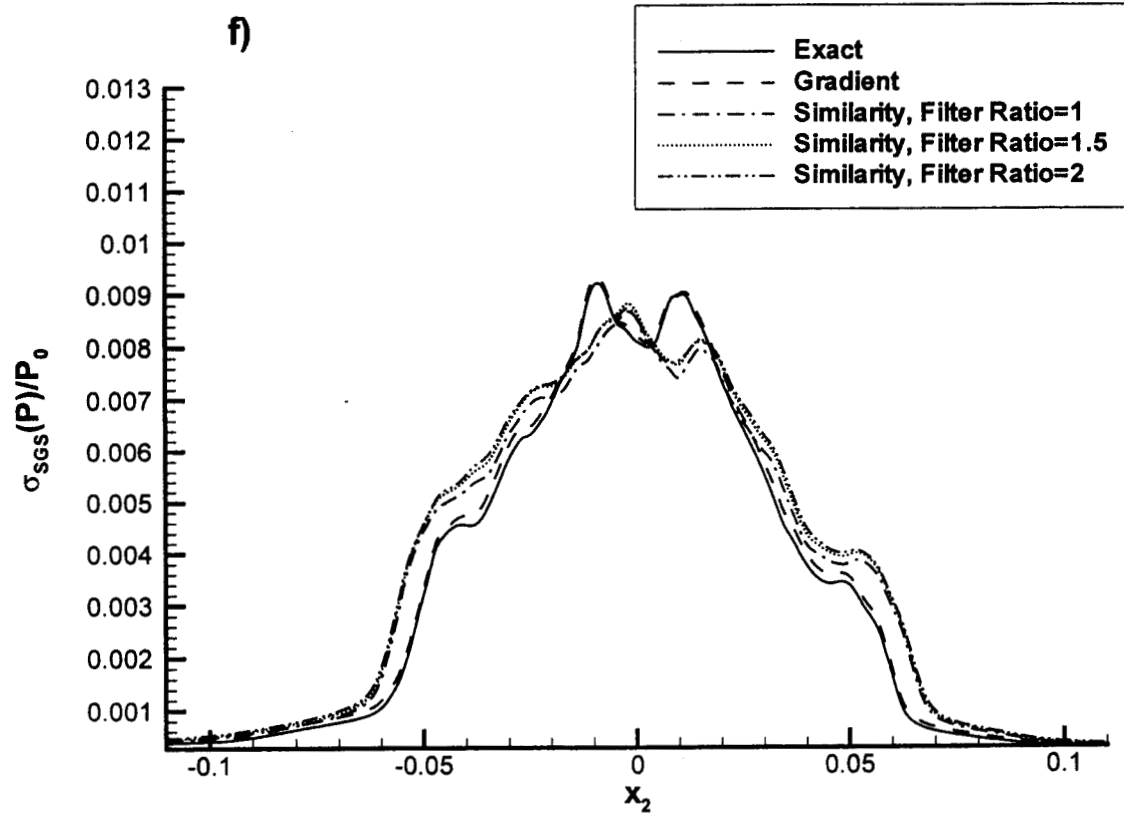
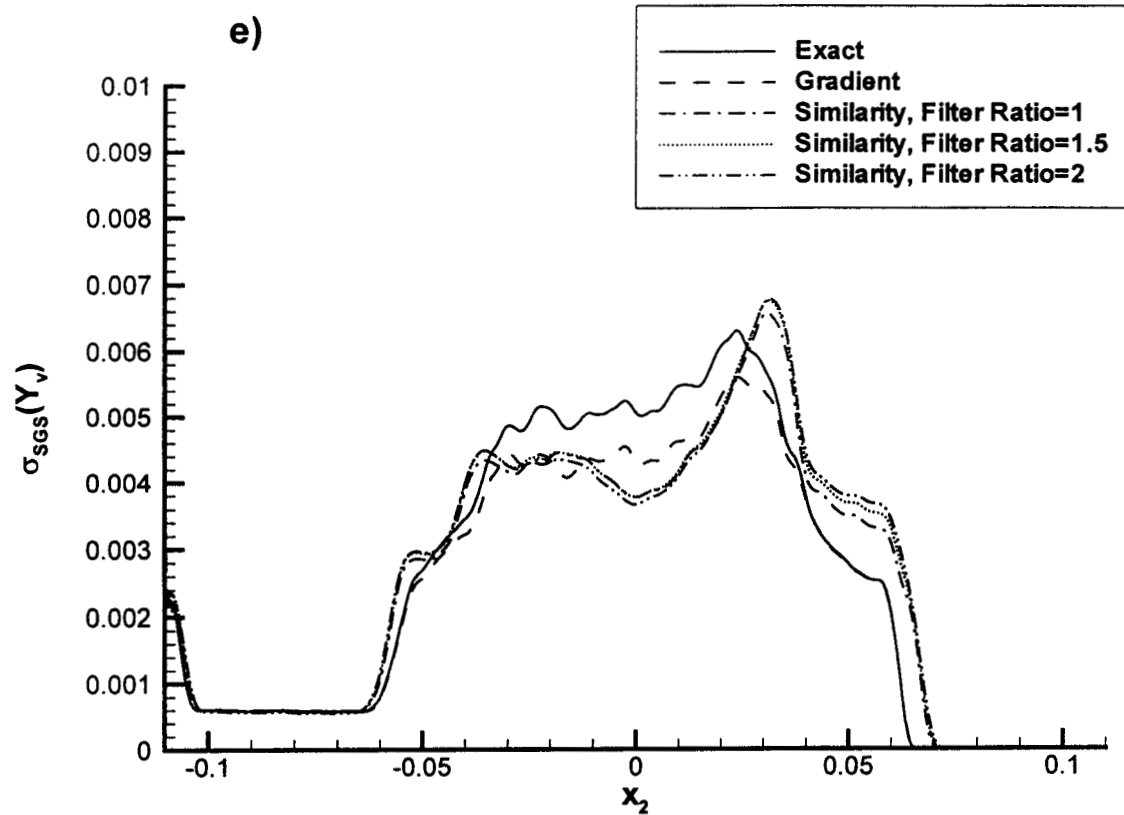


Figure 13. SGS standard deviation, Case TP600
a) u_1 b) u_2 c) u_3 d) T e) Y_v f) P